

# The study of the influence of micro-arc oxidation modes on the morphology and parameters of an oxide coating on the D16AT aluminum alloy

© 2023

**Fengyuan Bao**<sup>1,3</sup>, junior researcher, research engineer  
**Oleg V. Bashkov**<sup>\*1,4</sup>, Doctor of Sciences (Engineering), Professor,  
Head of Chair “Materials Science and Technology of Advanced Materials”  
**Dan Zhang**<sup>2,5</sup>, Doctor of Sciences (Engineering), Professor,  
Head of “Mechanical Engineering” Laboratory  
**Lan Lyu**<sup>1,2</sup>, graduate student  
**Tatiana I. Bashkova**<sup>1,6</sup>, PhD (Engineering), Associate Professor

<sup>1</sup>*Komsomolsk-na-Amure State University, Komsomolsk-on-Amur (Russia)*

<sup>2</sup>*Heilongjiang University of Science and Technology, Harbin (China)*

\*E-mail: bashkov@knastu.ru

<sup>3</sup>ORCID: <https://orcid.org/0000-0001-5762-7953>

<sup>4</sup>ORCID: <https://orcid.org/0000-0002-3910-9797>

<sup>5</sup>ORCID: <https://orcid.org/0000-0003-4150-7038>

<sup>6</sup>ORCID: <https://orcid.org/0000-0001-7070-5821>

Received 06.12.2022

Accepted 19.01.2023

**Abstract:** An effective way to protect valve metals and their alloys is the micro-arc oxidation method (MAO), which is currently used in various industries. However, to achieve the desired characteristics and properties of oxide coatings, a large number of experiments are required to determine an optimal oxidation mode, which makes the MAO method labor-intensive and resource-consuming. One of the ways to solve this problem is the search for an informative parameter or several parameters, the use of which during the oxidation process monitoring allows identifying a relationship between the MAO modes and the specified characteristics of oxide coatings. This paper studies the influence of the specified technological MAO modes (current density, oxidation time, amplitude of acoustic emission (AE) signals recorded during MAO) on the morphology and parameters of oxide coatings (thickness  $\delta$  and surface roughness  $R_a$ ) deposited on the D16AT aluminum alloy clad with pure aluminum. Multivariate planning of an experiment and the performed regression analysis allowed establishing a relationship between two oxidation factors (current density and oxidation time) and the parameters of the produced coatings. The authors proposed an additional factor, which is determined in the monitoring mode during the oxidation process as the time from the moment when the maximum or minimum of the acoustic emission (AE) amplitude recorded in the MAO process is reached until the end of the oxidation process. The study established that the introduction of an additional factor allows increasing significantly the reliability of the dependence between the coating parameters obtained experimentally and by the computational method based on the regression analysis. The authors note that when performing MAO, with the additional use of the MAO process monitoring by recording the AE amplitude, it is possible to achieve a high reliability between the calculated and actual values of the parameters of oxide coatings.

**Keywords:** micro-arc oxidation; oxide coating; acoustic emission; multivariate analysis; surface morphology; aluminum alloy; D16AT alloy; valve group alloy.

**Acknowledgements:** The work was supported by the Presidential grant for government support of leading scientific schools of the Russian Federation (project NSh-452.2022.4).

**For citation:** Bao F., Bashkov O.V., Zhang D., Lyu L., Bashkova T.I. The study of the influence of micro-arc oxidation modes on the morphology and parameters of an oxide coating on the D16AT aluminum alloy. *Frontier Materials & Technologies*, 2023, no. 1, pp. 7–21. DOI: 10.18323/2782-4039-2023-1-7-21.

## INTRODUCTION

Coatings produced by micro-arc oxidation (MAO) on the parts made of metals and alloys of the valve group, distinguishing by many valuable working and service properties (wear resistance, heat resistance, electrical insulating properties), have a special place among the surface treatment methods used in industry. The MAO method, similar to anodic oxidation, involves the oxidation of the surfaces of such metals as aluminum, magnesium, titanium, and other valve metals under the action of the electric current in an electrolyte. Compared to anodic oxidation, during MAO, the mixtures of various types of salts or alkalis

with a low concentration are used and not the concentrated acids. Oxidation is carried out under the action of micro-arc discharges formed by a high voltage pulse generator of positive polarity. The pulse amplitude can reach 400–600 V [1], and the pulse repetition rate depends on a generator type. At present, the MAO technology is not widely used for some reasons, including the lack of systematization of the relationship between parameters, which would contain practical recommendations for achieving the optimal oxidation regime [2].

Initially, it was believed that the MAO technology optimization should be based only on an in-depth study of the MAO mechanism to identify the oxide coating

formation process. The research in this area has indeed achieved significant results at the early stage of the MAO technology development. For example, the effective components in the electrolyte participating in the MAO process are determined based on the study of the electrochemical reaction principle. The direction of optimizing the power supply for MAO is determined based on the study of the electrical breakdown mechanism [3–5].

However, when studying the micro-arc oxidation mechanism, various models of interpretation of the oxide coating formation process appeared. The models accepted by the majority of scientists include the model of bubble breakdown on the anode, the model of oxide formation on the anode using the breakdown voltage  $U_B$ , the models based on the tunnel and avalanche effects, etc.

The development of basic research on the MAO technology is rather limited by the lack of a unified theoretical model. In recent years, the volume of study of the MAO mechanism has been gradually decreasing. At the same time, a large number of studies are focused on the optimal selection of the MAO process parameters using the optimization method. In most existing works, the method of planning of a multifactorial experiment is used, followed by determining the correlation between the processing factors and the parameters of the resulting coating properties. This allows establishing technical criteria for the efficient production management under certain conditions [6–8]. Such studies contributed to a significant development of MAO technology and allowed applying MAO in various industries.

However, due to the variety of MAO factors influencing the properties and parameters of the formed oxide coatings, and types of the widely used alloys of valve metals, it is necessary to carry out systematic studies, including the experiments under various conditions and using the effective methods for analyzing the results [9].

Today, the search for an associate parameter combined with the processing factors, which would ensure the complex of properties of the coatings produced with the MAO technology in real time, has become a promising direction of the study aimed at solving the noted problems. Based on this concept, various methods for controlling the MAO process were proposed: the method of monitoring the electrical parameters in the reverse circuit [10], the method of visual control of micro-arcs using a high-speed photo camera [11], the method of inductive measurement of the coating thickness in real time [12], and the method of accumulation of acoustic emission events during MAO [13–15].

According to the breakdown theory, the growth of oxide coatings is based on the formation of oxides melted after a high-voltage breakdown and solidified on the oxide metal surface. The energy dissipated during a discrete high-voltage breakdown is mainly converted into temperature, and some of the energy is converted into elastic waves propagating in the material. Acoustic emission (AE) signals recorded in the MAO process can carry the information about the source of a discrete electrical breakdown in the MAO process [16]. Therefore, the parameters of the recorded AE signals can be used to describe the kinetics of the oxide coating growth in real time.

Special features of the MAO technology make it difficult to control any parameters of a formed coating during processing. The surface thickness and roughness are one of the most requested parameters determining the properties and quality of the MAO-produced oxide coatings. These parameters are most often found in the literature and characterize MAO coatings to the fullest extent from the technological and operational point of view.

The study is aimed to establish the dependence of the oxide coating thickness and roughness on the micro-arc oxidation modes and to search for the possibility of controlling the parameters of a formed oxide coating in real time using the acoustic emission method.

## METHODS

### Materials and samples

Plates 2 mm thick, 20×20 mm in size cut from a D16AT aluminum alloy sheet in a naturally aged state and clad on both sides with pure aluminum 100 μm thick were used as the samples for the oxidation.

### Micro-arc oxidation unit

The MAO implementation scheme is shown in Fig. 1. Using a clamp, the sample is fixed in the electrolyte bath. An acoustic emission transducer (AET) is connected to a broadband amplifier and mounted on the sample above the clamp to prevent electrolyte from getting on the AET body, which is electrically isolated from the sample. The module for registration and control of the MAO system carries out the control of the MAO unit power source, the registration of the oxidation electrical parameters (voltage, current), as well as the registration of AE signals during the oxidation process. The MAO system can be used in two modes: voltage constraints and maximum current constraints. It gives the possibility to control the nature and mechanism of the oxide film growth.

The device ensures the formation of single-polarity pulses of positive polarity. The unit scheme is based on a three-phase double-wave rectifier with thyristor control. The electronic circuit diagram of the unit operates under the control of a computer with specially configured software. The rectifier generates voltage pulses with a frequency of 300 Hz and adjustable duration, which is determined by the oxidation current or voltage in accordance with the specified mode. In the work, the maximum current constraint mode was used.

To prevent the electrolyte from heating above 40 °C during oxidation, its thermostat control with the help of a water-cooling coil located in a stainless steel bath and acting as a cathode was used. For all the samples, MAO was performed in an electrolyte of the composition  $\text{Na}_2\text{SiO}_3 + \text{KOH} + \text{distilled water}$  [17; 18].

Registration and analysis of AE signals were performed using a system based on the Adlink PCI-9812 analog-to-digital converter and AE Pro 2.0 software. The GT301 broadband AET with a frequency range of 50–550 kHz was used as an AE transducer. The amplification factor of the AE signal amplifier was 40 dB. The AET was mounted on a D16AT aluminum alloy plate, which was a continuation of the sample.

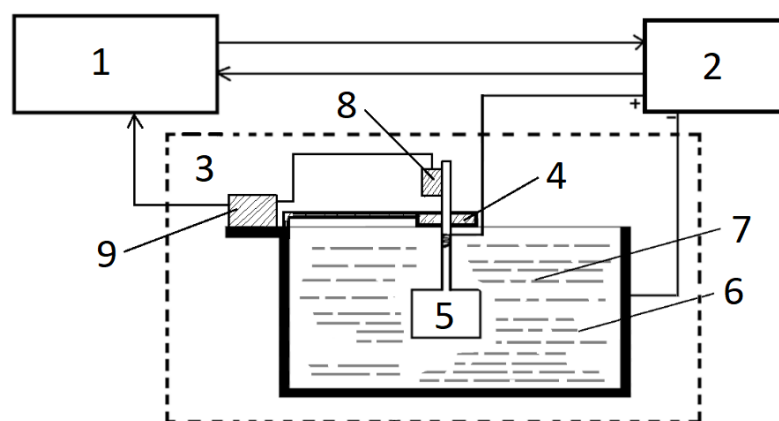


**Fig. 1.** The scheme of a unit for MAO and data registration:  
 1 – registration and control module; 2 – power source; 3 – oxidation cell;  
 4 – clamp; 5 – sample; 6 – bath; 7 – electrolyte;  
 8 – acoustic emission transducer (AET); 9 – amplifier

**Рис. 1.** Схема установки МДО и регистрации данных:  
 1 – модуль регистрации и управления; 2 – источник питания; 3 – ячейка для выполнения оксидирования;  
 4 – фиксатор; 5 – образец; 6 – ванна; 7 – электролит;  
 8 – преобразователь акустической эмиссии (ПАЭ); 9 – усилитель

### The experiment method

In this work, the application of the technique of multi-factorial planning and analysis allowed determining the degree of interrelation between the MAO process factors, as well as their influence on the parameters of the produced oxide coatings. The oxidation current density value  $i$  and the oxidation time  $t$  were the variable factors.

The oxidation modes specified by the two-factor experiment planning matrix are shown in Table 1.

During oxidation, the actual value of the oxidation pulse voltage  $U_D$  was recorded at the load in the return circuit. This parameter is necessary to control the MAO process after establishing the relationships between the specified modes and the target values of the coating parameters.

After oxidation carried out in the planned modes, the samples were washed in the distilled water and degreased. After that, the surface was analyzed using the Hitachi S-3400N scanning electron microscope (SEM) in two modes: the secondary electron (SE) mode to observe channels formed as a result of MAO, and the back-scattered electron (BSE) mode to study the surface topography. Thickness  $\delta$  and surface roughness  $R_a$  were chosen as informative parameters of the resulting oxide coating. The thickness of the coatings was determined by SEM after the preparation of transverse sections. Roughness  $R_a$  was determined with the TR200 portable roughness meter.

To establish the relationship between the specified MAO modes and the parameters of the produced oxide

**Table 1.** The experiment factor planning matrix  
**Таблица 1.** Матрица факторного планирования эксперимента

Factor	Samples								
	D1	D20	D10	D11	D5	D19	D12	D21	D9
Current density $i$ , A/dm <sup>2</sup>	22			48			74		
Treatment time $t$ , s	180	900	1620	180	900	1620	180	900	1620

Note. A number after the letter D in the designation of samples indicates the numerical order of a test series conducted during the research and is not associated with the number of experiment factor planning. At least three experiments were performed in each series to ensure its statistical repeatability and reliability.

Примечание. Цифра после буквы D в обозначении образцов означает порядковый номер серии испытаний, проводимых во время исследований, и не связана с номером факторного планирования эксперимента. В каждой серии выполнялось как минимум по три эксперимента, позволяющих обеспечить его статистическую повторяемость и достоверность.

coatings, the regression analysis was used. The technique consists in solving the linear regression equations using the parameters of the MAO modes (oxidation current density  $i$  and oxidation time  $t$ ) as the input variable factors, as well as the values of the parameters of the produced oxide coatings (thickness  $\delta$ , surface roughness  $R_a$ ) as the output results. The novelty of the study is in the use of an additional factor – the AE amplitude recorded in the monitoring mode during the entire oxidation process.

In addition to the parameters of the current density and the total oxidation time, a parameter was used that was defined as a period of time from the moment of cyclic change in the AE amplitude recorded in the MAO process to the end of the oxidation process. The paper considers the results of the study of oxide coatings produced depending on the specified MAO modes. Various periods of a cyclic change in the AE amplitude were used as an additional factor. The proposed approach allows increasing the reliability between the calculated and experimental values of the oxide coating parameters.

## RESULTS

According to the modes specified in Table 1, the experiments on the deposition of MAO coatings were carried out. Depending on the specified modes, the effective value of the pulse oxidation voltage  $U_D$ , that is an important parameter determining the nature of the oxide coating formation due to the spark and micro-arc discharges on the surface of a passivated metal, changed during the oxidation process. A time dependence  $U_D(t)$  typical view for a sample oxidized at the current density  $i=48 \text{ A/dm}^2$  is shown in Fig. 2. The arrows in figure indicate the oxidation time periods for the samples:  $t=180 \text{ s}$  is for *D11*,  $t=900 \text{ s}$  is for *D5*, and  $t=1620 \text{ s}$  is for *D19*.

Fig. 3 shows the SEM images of the surface of MAO coatings produced in accordance with the modes indicated in Table 1, at the current density  $i=48 \text{ A/dm}^2$  and time limits indicated in Fig. 2.

Fig. 3 shows that the surface uniformity decreases significantly with an increase in the processing time. In the MAO initial period, the low breakdown voltage does not lead to the formation of molten oxides on the sample

surface due to the low intensity of micro-arc discharges. Moreover, practically the same dielectric properties of an oxide layer along the entire surface make it possible to uniformly distribute a dense grid of micro-arc discharges over the sample. However, the increased current density in the substrate protruding parts leads to a relatively rough surface in local areas. In general, the roughness of the initial substrate surface influences greatly the quality of a resulting MAO coating, since the oxide coating morphology at this stage repeats the substrate surface, enhancing the relief.

Fig. 3 c shows the coating surface morphology at the next oxidation stage limited by the experiment time constraints (sample *D19* in Fig. 2). According to the image obtained using SEM in the SE mode, the diameter of channels in this oxidation period practically did not increase. However, the relief unevenness and the distribution of channels over the surface caused by the formation of molten oxides overlapping the existing channels resulting from local intense micro-arc discharges increased. The uneven distribution of breakdown sites led to a significant increase in the coating surface roughness.

Three-dimensional graphs obtained using the cubic interpolation of experimental data and shown in Fig. 4 allow visualizing the dependence of values of the oxide coating parameters ( $\delta$  and  $R_a$ ) obtained after oxidation on the MAO modes ( $i$ ,  $t$ ). This is necessary when choosing the range of optimal processing parameters. In the 3-D dependence graphs, the dots mark the experimental values of the measured parameters obtained under the specified MAO modes.

The 3-D dependences show that the  $\delta$  and  $R_a$  values do not have the same growth function of the measured parameter on the given factors ( $i$ ,  $t$ ) within the entire range [19], and in a certain range of the factors' values, a significant change in the  $\delta$  and  $R_a$  parameters is not observed.

To establish the relationship between the MAO modes and the parameters of the produced coatings, a regression analysis was carried out. The resulting regression equations of the coating  $\delta$  and  $R_a$  parameters measured during MAO and one of the oxidation electrical parameters (the effective value of the pulse oxidation voltage  $U_D$ ) are presented in the formulas:

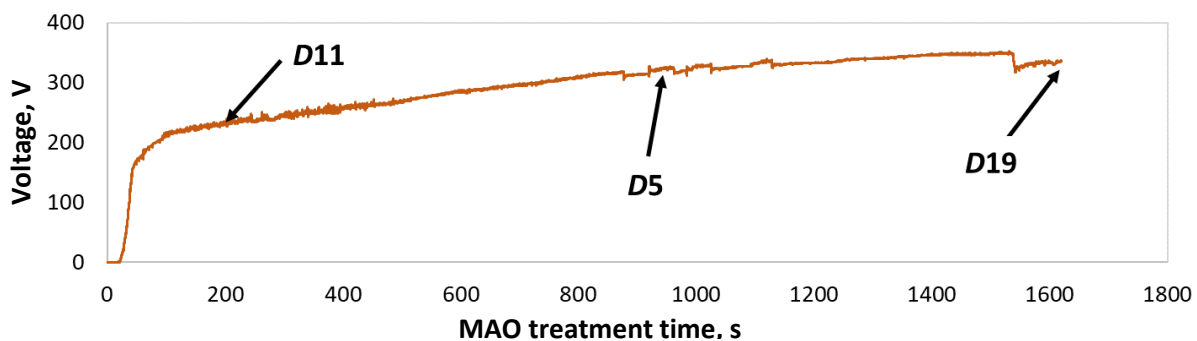
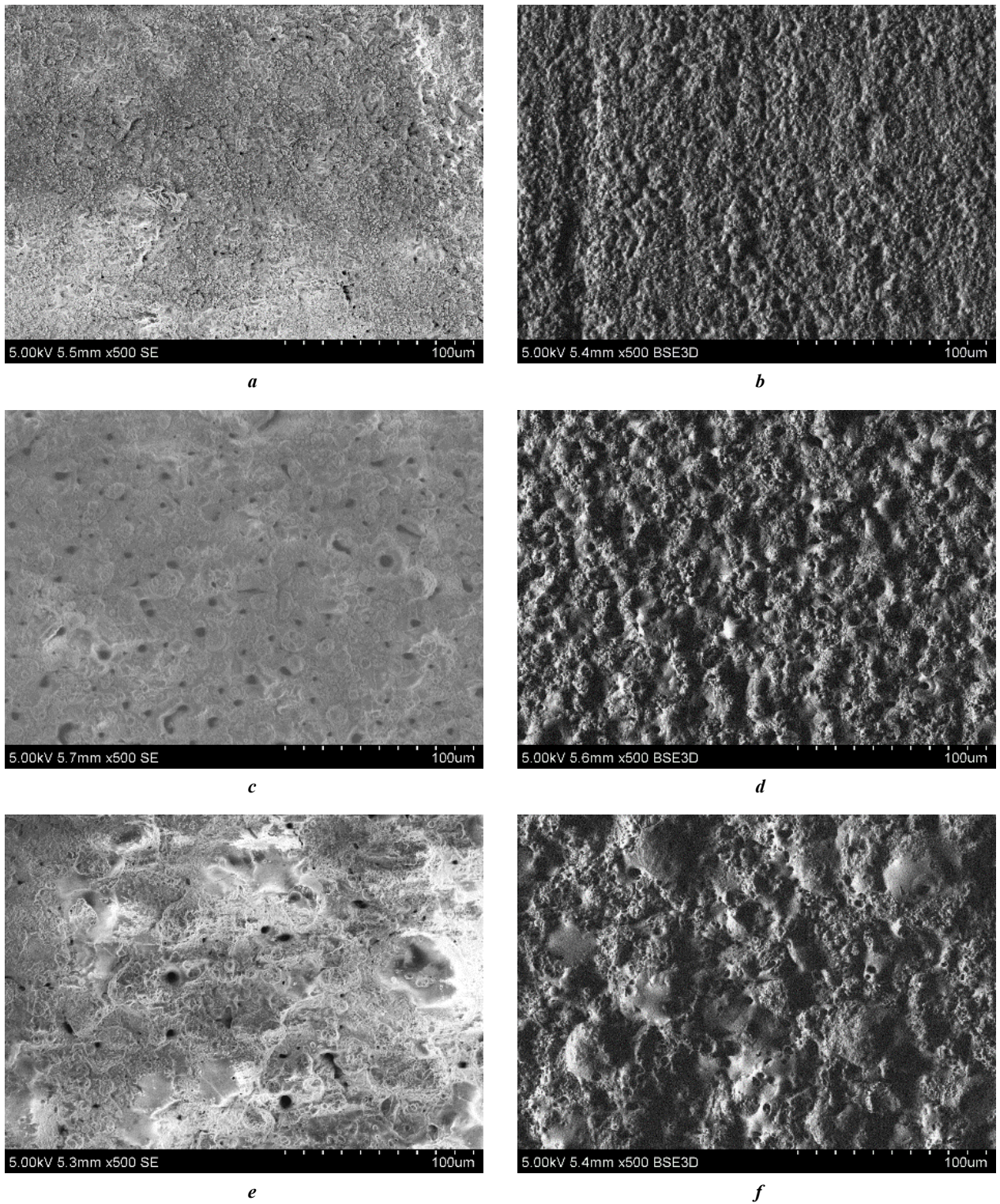
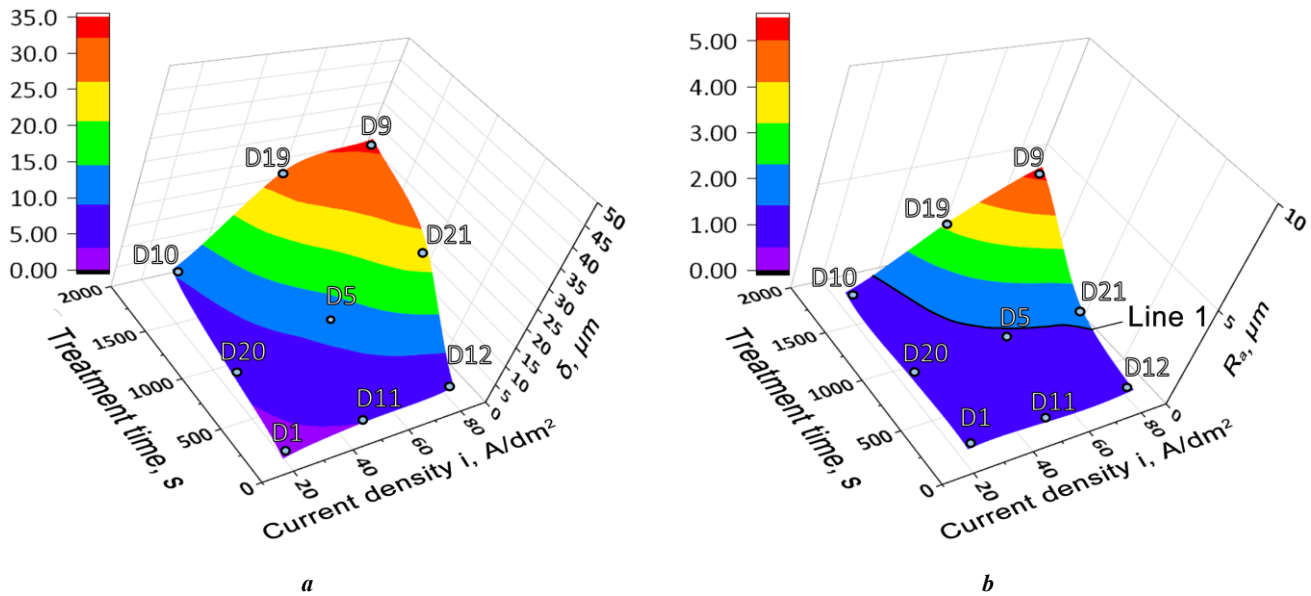


Fig. 2. The diagram of the voltage dependence on the MAO time  
 Рус. 2. Диаграмма зависимости напряжения от времени МДО



*Fig. 3. MAO-coating surface morphology for the samples:  
a, b – D11; c, d – D5; e, f – D19*

*Рис. 3. Морфология поверхности МДО-покрытия для образцов:  
a, b – D11; c, d – D5; e, f – D19*



**Fig. 4.** 3-D dependences of the MAO-coating parameters on the specified factors: **a** –  $\delta(i, t)$ ; **b** –  $R_a(i, t)$   
**Рис. 4.** Трёхмерные зависимости параметров МДО-покрытий от заданных факторов: **a** –  $\delta(i, t)$ ; **b** –  $R_a(i, t)$

$$\delta = -12,199 + 0,2819 \times i + 0,0123 \times t ;$$

$$R_a = -1,275 + 0,0327 \times i + 0,0015 \times t ;$$

$$U_D = 95,37 + 2,1875 \times i + 0,0757 \times t .$$

Table 2 shows the coating  $\delta$  and  $R_a$  parameters obtained experimentally and calculated by solving the linear regression equations using the corresponding MAO modes for each sample.

Fig. 5 a shows that the dependences of both the experimental and calculated values of the coating thickness  $\delta$  on the stress  $U_D$  have a rather high reliability of linear approximation and practically converge with each other. The dependences of the experimental and calculated values of the  $R_a$  roughness on the  $U_D$  voltage do not coincide according to the linear approximation graphs (Fig. 5 b), which is explained by the heredity of the sample surface relief at a low thickness of the oxide coating.

However, from a practical perspective, the relationship between the “experimental” and “calculated” values of the oxide coating parameters (Fig. 6) can be an informative graph used for the assessment of the reliability of using a linear regression model.

The displayed dependences show that the use of a linear regression model to determine  $\delta$  and  $R_a$ , by calculation and experimentally, had poor accuracy (error level – 0.9 and 0.8, respectively). In this regard, the authors decided to use additional parameters obtained using the AE method.

Fig. 7 shows the time diagrams for the amplitude of the AE signals recorded during the MAO process. The signals are single pulses following periodically during the entire period of oxidation. The AE signal repetition period depends on the frequency of the pulse generator of the MAO unit. The amplitude and other AE signal parameters depend on the mode and features of oxidation.

As for the time dependence of the AE signal amplitude (Fig. 7), the diagrams show the differences depending on the specified values of the current  $i$  and the time  $t$  passed from the oxidation onset. It should be noted that the nature of the change in the amplitude of the AE signals recorded in the initial oxidation period retains regardless of the current density  $i$ . Depending on the oxidation modes, several cycles of the increase and subsequent decrease in the amplitude of the recorded AE signals can be observed. However, the period when the cycle of change in the AE amplitude proceeds is different for different values of the oxidation current density.

The process of changing the amplitude of the recorded AE signals can be divided into 4 stages. The boundaries of the stages are marked with letters and compared to the change in time of the recorded voltage  $U_D$  value. For the quantitative assessment of the values of the AE amplitude recorded during the MAO process, the authors used as an additional new factor the values of the time periods ( $AN$ ,  $BN$ , and  $CN$ ) from the end of each of the stages ( $OA$ ,  $AB$ , and  $BC$ , respectively) to the end of the MAO process. These periods were used to construct the linear regression equations and are shown in Table 3 as the oxidation factors  $P_1$ ,  $P_2$ , and  $P_3$ .

It should be noted that in Table 3, the values of the  $P_2$  and  $P_3$  parameters are actually absent for some modes. This is caused by the fact that when selecting the modes with a short oxidation time or low current density, the oxidation process may not reach the  $P_2$  or  $P_3$  stage.

The linear regression equations when calculating the values of the coating parameters using the  $P_1$  factor take the form:

$$\delta = 11,922 + 0,018 \times i - 0,2267 \times t + 0,2426 \times P_1 ;$$

$$R_a = 2,3277 - 0,0067 \times i - 0,0344 \times t + 0,0362 \times P_1 .$$

**Table 2.** Values of MAO-coating parameters  
**Таблица 2.** Значения параметров МДО-покрытия

Sample No.	MAO-coating parameters					
	Experimental values			Calculated values		
	$\delta$ , $\mu\text{m}$	$R_a$ , $\mu\text{m}$	$U_D$ , V	$\delta$ , $\mu\text{m}$	$R_a$ , $\mu\text{m}$	$U_D$ , V
<b>D20</b>	5.4±0.8	0.77±0.08	198±10	6.33	0.79	212
<b>D10</b>	10.1±2.1	0.87±0.10	254±14	16.20	1.87	266
<b>D11</b>	4.1±1.0	0.71±0.11	254±14	3.80	0.56	214
<b>D5</b>	12.4±2.2	1.33±0.22	281±14	13.67	1.64	269
<b>D19</b>	28.4±2.7	3.16±0.34	348±15	23.53	2.72	323
<b>D12</b>	5.5±1.0	0.83±0.11	254±12	11.41	1.45	273
<b>D21</b>	24.6±2.6	1.84±0.25	343±16	21.27	2.53	328
<b>D9</b>	32.1±2.7	4.97±0.36	362±16	31.14	3.61	382

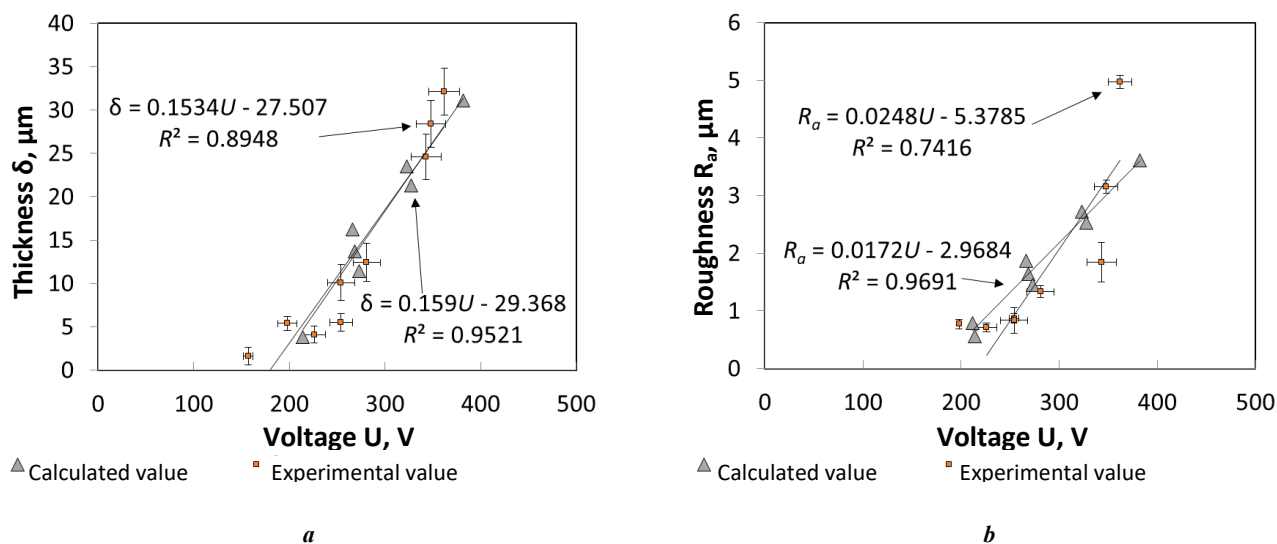


**Fig. 5.** The dependences of experimental and calculated values of the parameters of coatings on the voltage  $U_D$ :  
**a** –  $\delta(U_D)$ ; **b** –  $R_a(U_D)$

**Рис. 5.** Зависимости экспериментальных и расчетных значений параметров покрытий от напряжения  $U_D$ :  
**a** –  $\delta(U_D)$ ; **b** –  $R_a(U_D)$

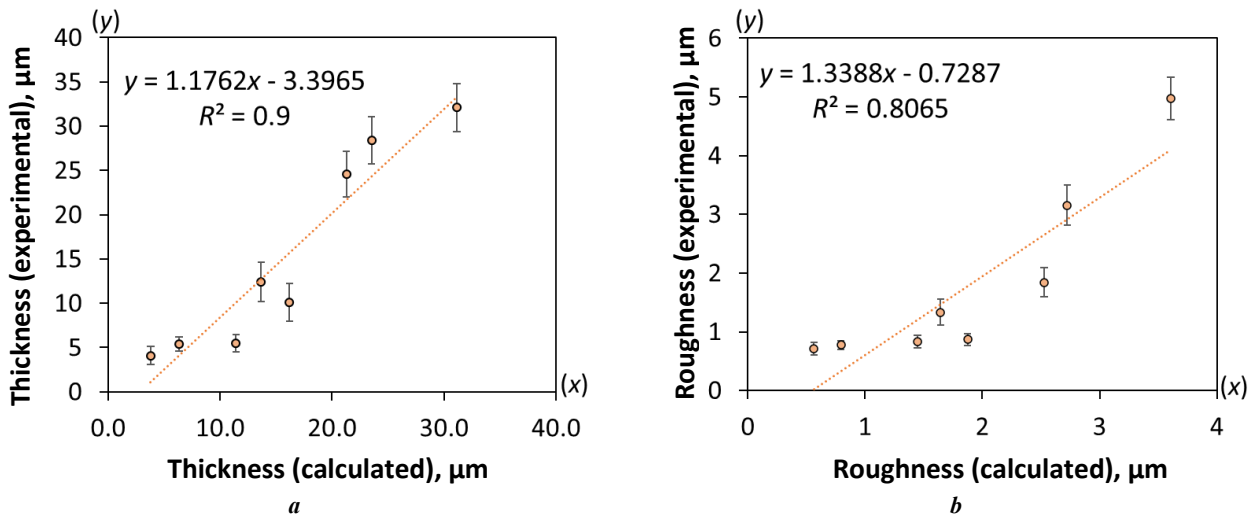


Fig. 6. A graph relating the experimental and calculated values of the MAO-coating parameters:  
*a* – coating thickness; *b* – coating roughness

Рис. 6. График, связывающий экспериментальные и расчетные значения параметров МДО-покрытия:  
*a* – толщина покрытия; *b* – шероховатость покрытия

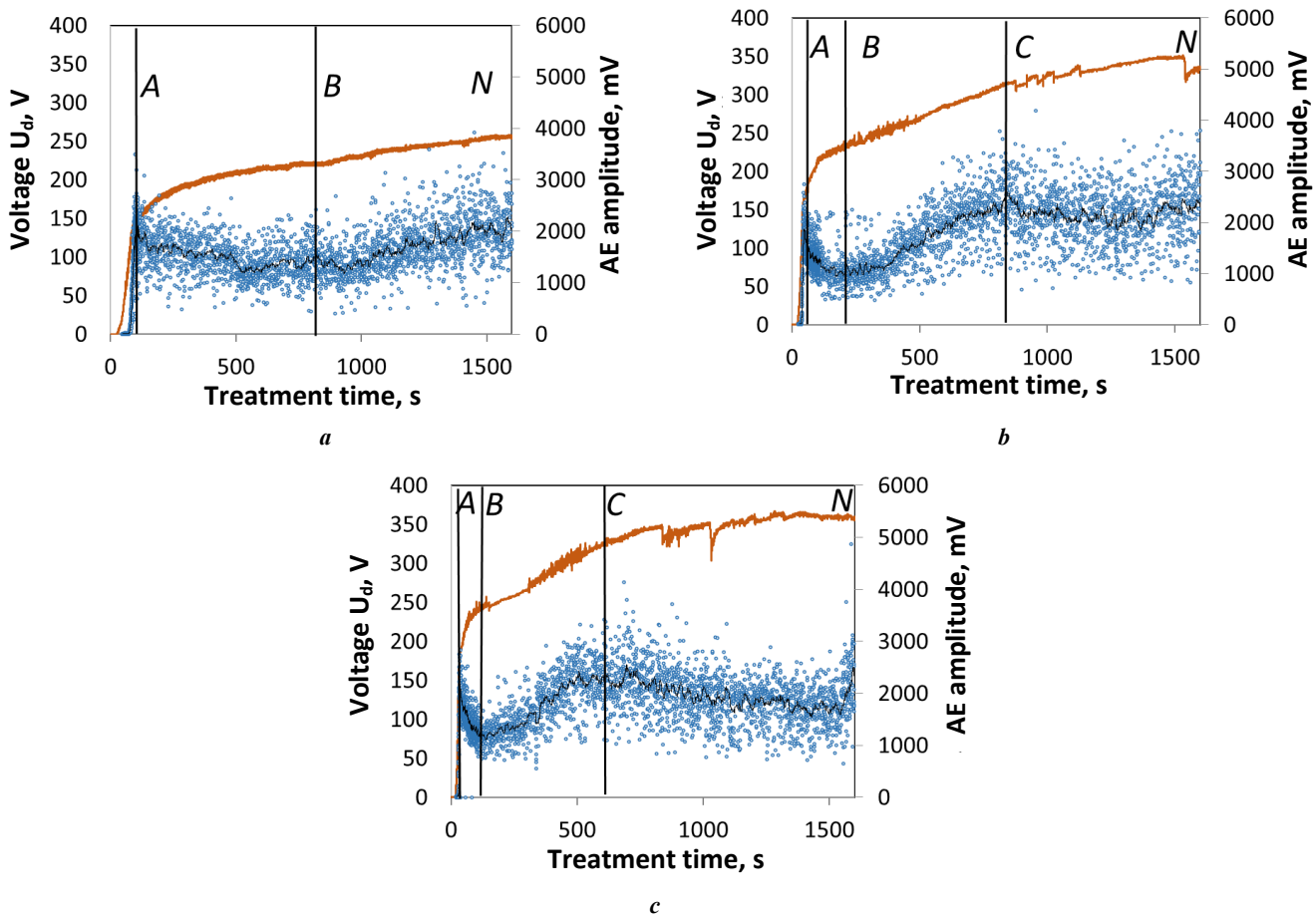


Fig. 7. Time diagrams of the AE amplitude and oxidation voltage registered during MAO:  
*a* – sample D10; *b* – sample D19; *c* – sample D9.

In the diagrams: A – the boundary of the 1 and 2 stages; B – the boundary of the 2 and 3 stages;  
 C – the boundary of the 3 and 4 stages; N – MAO process termination

Рис. 7. Диаграммы временных зависимостей амплитуды АЭ и напряжения окисления, регистрируемых в процессе МДО:

*a* – образец D10; *b* – образец D19; *c* – образец D9.

На диаграммах: А – граница стадий 1 и 2; В – граница стадий 2 и 3;  
 С – граница стадий 3 и 4; N – завершение процесса МДО

Table 3. AE parameters  
 Таблица 3. Параметры АЭ

Oxidation period, s	Sample No.								
	D1	D20	D10	D11	D5	D19	D12	D21	D9
AN ( $P_1$ )	109±5	808±7	1515±8	135±7	859±6	1575±5	151±7	868±8	1587±5
BN ( $P_2$ )	–	400±15	690±20	–	700±18	1394±16	46±10	768±14	1479±14
CN ( $P_3$ )	–	–	–	–	70±23	795±20	–	258±18	984±21

The linear regression equations when calculating the values of the coating parameters using the  $P_2$  factor take the form:

$$\delta = -7,8397 + 0,018 \times i - 0,0014 \times t + 0,0174 \times P_2;$$

$$R_a = -1,2374 - 0,0229 \times i + 0,00000955 \times t + 0,0026 \times P_2.$$

The linear regression equations when calculating the values of the coating parameters using the  $P_3$  factor take the form:

$$\delta = -0,0001 + 60,3825 \times i + 8,5813 \times t - 8,5 \times P_3;$$

$$R_a = 1528,2181 - 9,1459 \times i - 1,31 \times t + 1,3 \times P_3.$$

Table 4 gives the values of the coating  $\delta$  and  $R_a$  parameters obtained experimentally and calculated by solving the above equations using an additional factor.

At the first stage *OA* up to a voltage of 150–250 V, at a certain point, a rather rapid growth of the signal amplitude to the values of 2500–3000 mV begins. Then, the signal amplitude starts to gradually decrease. The greater is the oxidation current density, the higher is the decrease rate. Hereinafter, the amplitudes of the signals recorded by the GT301 model AET mounted on a duralumin plate, acting as a waveguide and being a continuation of the sample used in the oxidation, are given. After a certain oxidation time, the amplitude of the recorded signals reaches a certain minimum (*AB* stage), following which, the amplitude growth resumes and reaches a new maximum (*BC* stage). Further, depending on the MAO duration, the process of changing the amplitude of the recorded AE signals can reoccur. One more full cycle of the decrease and subsequent increase in the amplitude is observed during the oxidation of samples with a current density of 48 and 74 A/dm<sup>2</sup>.

Fig. 7 demonstrates that at the initial stage *OA*, at a high rate of the oxidation voltage  $U_D$  growth, the formation of a barrier film and the appearance of a luminescence begin on the anode surface, accompanied by the formation of a large number of small bubbles. The amplitude of the recorded AE signals starts from 5–50 mV at the beginning and rapidly increases to 2300 mV by the end of the *OA* stage.

Fig. 8 shows the graphs relating the experimental and calculated values of the MAO-coating parameters with the participation of the AE  $P_1$  factor as an additional factor in the regression calculation. The *OA* stage boundary for determining the  $P_1$  parameter is the achievement of the maximum AE amplitude values in the first cycle of the AE amplitude change during the oxidation period.

Using the  $P_1$  stage achievement time, it can be identified that the reliability of the linear approximation between the calculated and experimental values of the thickness  $\delta$  and oxide coating roughness  $R_a$  is much higher (Fig. 8) compared to the results of the regression calculation without the additional  $P_1$  factor (Fig. 6).

The three-dimensional dependence in Fig. 4 illustrates that the coating roughness increases sharply when a certain critical line 1 is reached under the action of two factors. However, during the oxidation period corresponding to the first stage *OA* (Fig. 7 a), no sharp increase in the coating roughness  $R_a$  is observed, since during this period, a barrier layer is formed without the stable growth of the oxide coating, and the roughness is determined by the hereditary relief of the sample surface prepared before oxidation.

Therefore, the results of linear regression by the  $P_1$  factor characterizing the coating roughness have a rather low value of the reliability of the linear approximation  $R^2=0.8217$  with the experimental values (Fig. 8 b).

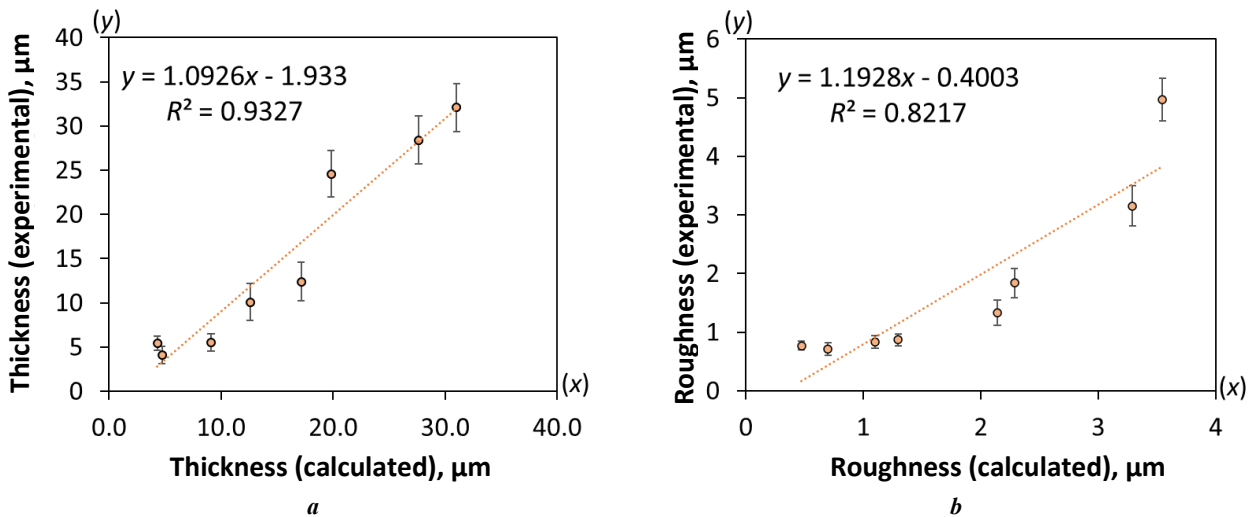
At the *AB* stage (Fig. 7 c), when the breakdown potential of the passivating film is reached, spark discharges gradually appear on the anode surface. The average value of the AE amplitude at the *AB* stage decreases to a value of 800 mV, which is minimal in the first cycle of changing the AE signals amplitude.

Fig. 9 shows the graphs relating the experimental and calculated values of the thickness  $\delta$  and roughness  $R_a$  of the coating when using the AE  $P_2$  factor in the regression analysis. As opposed to the  $P_1$  factor, the time period determined by the change in the amplitude of the recorded AE signals shifts to the right along the time axis and is defined as the *BN* period from the moment the *AB* stage is completed to the end of MAO. The *AB* stage boundary for determining the  $P_2$  parameter is the achievement of the minimum AE amplitude values at the beginning of the second cycle of the AE amplitude change.

It should be noted that the  $P_1$  factor determined by the initial stage of treatment includes both the MAO period and the period when a sample reaches the passivation

**Table 4.** Test results  
Таблица 4. Результаты эксперимента

Sample No.	Experimental values		Calculated values					
	$\delta, \mu\text{m}$	$R_a, \mu\text{m}$	$\delta, \mu\text{m}$			$R_a, \mu\text{m}$		
			$P_1$	$P_2$	$P_3$	$P_1$	$P_2$	$P_3$
D20	5.4±0.8	0.77±0.08	4.3	4.4	–	0.5	0.31	–
D10	10.1±2.4	0.87±0.10	12.6	10.4	–	1.3	1.07	–
D11	4.1±1.0	0.71±0.11	4.7	–	–	0.7	–	–
D5	12.4±2.5	1.33±0.22	17.2	14.5	16.7	2.1	1.70	1.32
D19	28.4±2.7	3.16±0.34	27.6	27.5	32.7	3.3	3.51	3.14
D12	5.5±1.0	0.83±0.11	9.1	7.0	–	1.1	0.60	–
D21	24.6±2.8	1.84±0.25	19.8	20.5	28.9	2.3	2.49	1.83
D9	32.1±2.7	4.97±0.36	31.0	33.9	36.4	3.5	4.35	4.95



**Fig. 8.** A graph relating the experimental and calculated values of the thickness  $\delta$  (a) and roughness  $R_a$  (b) of the coating with the participation of the  $P_1$  factor  
**Рис. 8.** График, связывающий экспериментальные и расчетные значения толщины  $\delta$  (a) и шероховатости  $R_a$  (b) покрытия при участии фактора  $P_1$

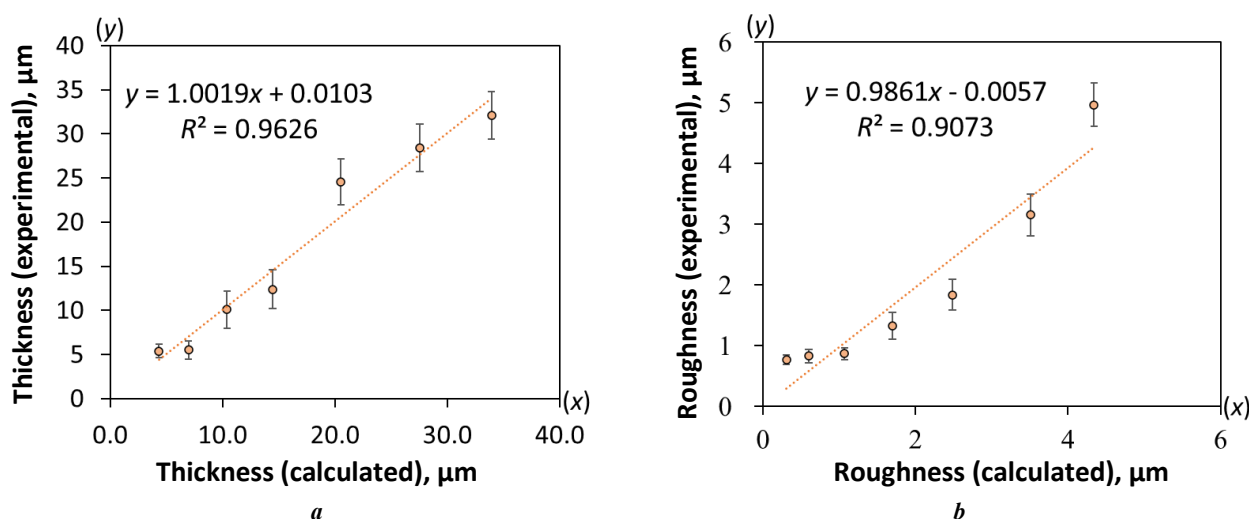


**Fig. 9.** A graph relating the experimental and calculated values of the thickness  $\delta$  (a) and roughness  $R_a$  (b) of the coating with the participation of the  $P_2$  factor  
**Рис. 9.** График, связывающий экспериментальные и расчетные значения толщины  $\delta$  (a) и шероховатости  $R_a$  (b) покрытия при участии фактора  $P_2$

potential, during which there is no stable growth of the oxide coating due to the MAO mechanism. Therefore, the use of the  $P_2$  parameter as compared to  $P_1$ , which is determined by the processing time during the  $BN$  period, makes it possible to further increase the reliability of the approximation between the values of the calculated and experimental data for determining the coating thickness and roughness.

At the  $BC$  stage (Fig. 7), the average amplitude of the AE signals increases as the oxidation voltage increases up to a maximum value of 2500 mV with a large dispersion of values. An increase in the signal amplitude occurs with a simultaneous increase in the size and brightness of individual micro-arc discharges on the anode surface.

Fig. 10 presents a graph relating the experimental and calculated values of the coating thickness  $\delta$  and roughness  $R_a$  when using the additional  $P_3$  factor in the regression analysis. The achievement of the maximum AE amplitude values in the second cycle of the AE amplitude change during MAO is the boundary of the  $BC$  stage for determining the  $P_3$  parameter. The  $CN$  period is defined from the end of the  $BC$  stage to the end of MAO.

Fig. 7 b, 7 c show that the  $C$  boundary shifts backward along the time axis with an increase in the current density  $i$ . In combination with the analysis presented in Fig. 4 b, 4 c, one can see that for different samples, the time points determined by the  $C$  stage boundary almost coincide in the same range of two contour lines of the  $\delta$  value change. It indicates that there is a relationship between the  $CN$  period, determined according to the AE amplitude change, and the coating thickness  $\delta$ .

The abovementioned analysis proves that the  $P_3$  factor has a closer relationship with the MAO-coating parameters than the  $P_1$  and  $P_2$  factors. Using the  $P_3$  stage achievement time as an additional factor in solving the linear regression equations, as shown in Fig. 9, it is possible to achieve the approximation reliability equal to 1 between the values of the calculated and experimental data on the coating thickness and roughness.

## DISCUSSION

The results of the analysis of three-dimensional dependences showed that the change in the coating thickness and roughness is nonlinear within the range of the oxidation period  $t=180-1620$  s and the current density  $i=22-74$  A/dm<sup>2</sup>. This makes it inappropriate to use a linearly changing parameter (processing time, current density) to establish the dependences of the resulting coating parameters on the MAO modes.

One of the conventional solutions to this problem is the use of a non-linear variable concurrent parameter – the effective impulse voltage  $U_D$ . However, the results of study of the dependence of the coating parameters on  $U_D$  showed poor accuracy for determining  $\delta$  and  $R_a$  (the error level is 0.89 and 0.74, respectively). A known effective way to increase the reliability of the established dependences is to use the linear regression technique. According to the results of the regression equations calculation, one can see that the reliability of the approximation between the values of the calculated and experimental data was 0.90 for the coating thickness values and 0.81 – for the roughness.

The registration of the AE amplitude in the monitoring mode allowed increasing the reliability and accuracy of determining the values of coating parameters when using the regression analysis. The results of the study of the recorded AE signals within the MAO modes set in the work showed several cycles of the increase and subsequent decrease in the amplitude. The causes for the change in the amplitude can be explained by the mechanism of the ongoing process of the oxide coating formation and growth under the conditions specified by the oxidation modes. Multiple formation of bubbles at the  $OA$  stage, which is not yet associated with the formation of sparks and micro-arcs on the anode surface, leads to coherent combining of an acoustic noise from their collapse and, as a consequence, to an increase in the amplitude of the AE signals [20]. The  $P_1$  parameter defined as the  $AN$  period eliminates

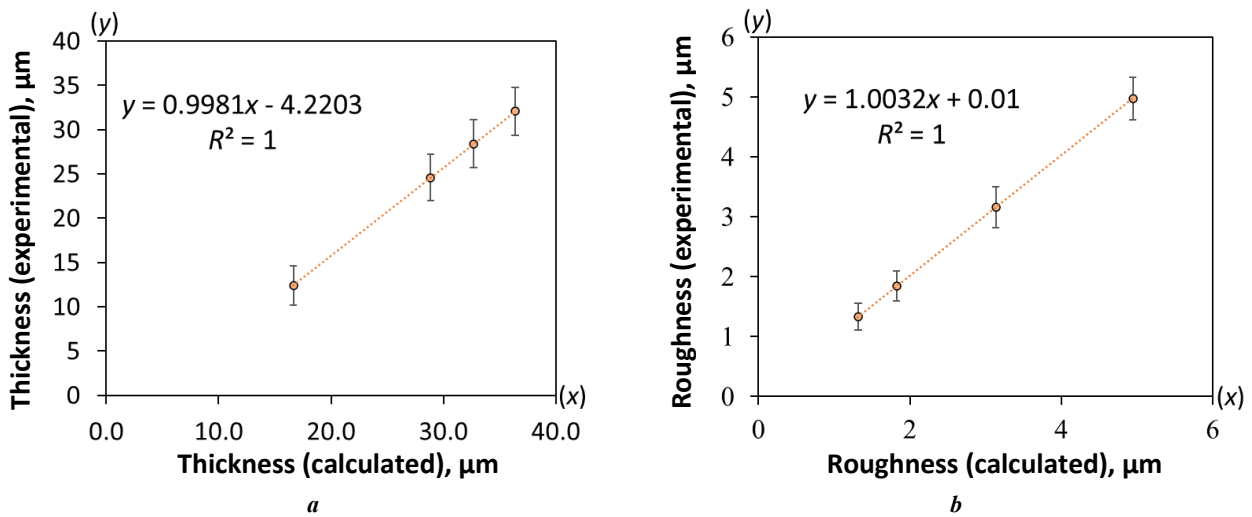


**Fig. 10.** A graph relating the experimental and calculated values of the thickness  $\delta$  (a) and roughness  $R_a$  (b) of the coating with the participation of the  $P_3$  factor  
**Рис. 10.** График, связывающий экспериментальные и расчетные значения толщины  $\delta$  (a) и шероховатости  $R_a$  (b) покрытия при участии фактора  $P_3$

the negative effect of the initial *OA* period, when the electrical breakdowns have not yet begun, on the linear dependence determined by the regression equation. It explains the increase in the accuracy of determining the oxide coating thickness up to 0.93 and the roughness up to 0.82 when using the  $P_1$  parameter as an additional factor.

The transition to the passivation state caused by the formation of a dense but still rather thin barrier layer leads to an increase in the size and a decrease in the number of bubbles occurring on the surface due to the formation of the first spark breakdowns, the number and energy of which gradually increase as the breakdown potential and the oxide film increase. Due to a change in the noise generation mechanism, the amplitude of the recorded AE signals first slightly decreases at the *AB* stage, but as the spark breakdown quantity and the oxide film thickness increase at the *BC* stage, it again increases. It is confirmed by the surface morphology of the coatings produced at various stages of oxidation. Fig. 3 a and 3 d show the coating surface obtained at the *AB* stage, where only multiple very-small-diameter channels are visible, characterizing the sparking onset. The replacement of the  $P_1$  parameter in the regression analysis with the  $P_2$  parameter determined by the *BN* period duration increases the accuracy of determining the coating thickness to 0.96 and the roughness – to 0.91.

Fig. 3 b and 3 e demonstrate the oxidized sample surface at the same current density at the end of the *BC* stage. One can assume that the *BC* stage is a transition stage between the spark and micro-arc oxidation processes. The increase in the amplitude of the AE signals is obviously associated with an increase in the pore diameter caused by an increase in the pulse energy as a result of sparking.

A further increase in the coating thickness at the *CN* stage first leads to a decrease in the number of breakdown channels, which are the centers of micro-arc discharges at this stage, and, as a result, to a certain decrease in the amplitude of the recorded AE signals. The use of the

$P_3$  parameter determined by the *CN* period duration increased the accuracy of determining the thickness and roughness to 1. The results of the study demonstrate the importance of the influence of the oxidation duration at the final stage on the quality of the resulting coating.

The division of the oxidation time into periods characterizing a certain oxidation mechanism allows increasing the reliability of the relationship between the calculated and experimental values of the coating parameters.

It should be noted that the proposed approach has some constraints. These constraints include the absence of the  $P_2$  and  $P_3$  parameters for a certain ratio of oxidation time and current density, at which the oxidation process stays within the spark breakdown limits and does not go into the micro-arc mode. For these modes, either the *CN* stage or the *BC* and *CN* stages at the same time will be absent.

## MAIN RESULTS AND CONCLUSIONS

The paper proposes a technique that allows establishing the dependence of the parameters of the oxide coating deposited on the D16AT aluminum alloy on various MAO modes. The technique is based on the solution of linear regression equations obtained as a result of an experiment with two factors: time and current density of oxidation. The reliability of the relationship between the experimental and calculated values of the oxide coating thickness and roughness was 0.89 and 0.74, respectively.

The introduction of an additional factor, defined as a period of time from the moment of reaching the minimum or maximum value of the AE signal amplitude cyclically changing during the oxidation process until the end of oxidation, increases the reliability of the linear approximation between the values of the coating parameters obtained experimentally or by calculation. The use of the time period from the moment of reaching the maximum value in the second cycle of the AE signal amplitude change to the oxidation process termination allows maximizing the reliability of the coating parameters' values obtained

by calculation as a result of solving the linear regression equations against the values obtained experimentally.

The addition of the proposed technique with a third controlled factor allows expanding its functionality and applying it in the online monitoring mode during the MAO process to increase the reliability of obtaining the specified values of the oxide coating thickness or roughness.

## REFERENCES

- Yerokhin A., Nie X., Leyland A., Matthews A., Dowe J. Plasma electrolysis for surface engineering. *Surface and coatings technology*, 1999, vol. 122, no. 2-3, pp. 73–93. DOI: [10.1016/S0257-8972\(99\)00441-7](https://doi.org/10.1016/S0257-8972(99)00441-7).
- Pecherskaya E.A., Golubkov P.E., Karpanin O.V., Kozlov G.V., Zinchenko T.O., Smogunov V.V. The influence of technological parameters on the properties of coatings synthesized by microarc oxidation. *Izmerenie. Monitoring. Upravlenie. Kontrol*, 2020, no. 2, pp. 89–99. DOI: [10.21685/2307-5538-2020-2-11](https://doi.org/10.21685/2307-5538-2020-2-11).
- Shi M., Li H. The mathematical mode of Ti alloy micro-arc oxidation process parameters and ceramic coating and experimental study. *Journal of Yunnan University: Natural Sciences Edition*, 2015, vol. 37, no. 1, pp. 102–110.
- Chen H., Hao J., Feng Z. Micro-arc oxidation mechanism and electrical discharge model. *Journal of Chang'an University (Natural Science Edition)*, 2008, vol. 28, pp. 116–119.
- Golubkov P.E., Pecherskaya E.A., Artamonov D.V., Zinchenko T.O., Gerasimova Yu.E., Rozenberg N.V. Electrophysical model of micro-arc oxidation process. *Izvestiya vysshikh uchebnykh zavedeniy. Fizika*, 2019, vol. 62, no. 11, pp. 166–171. DOI: [10.17223/00213411/62/11/166](https://doi.org/10.17223/00213411/62/11/166).
- Dudareva N.Yu., Akhmedzyanov D.A. Tribological parameters of MAO-layers formed in silicate-alkaline electrolyte on samples of high-silicon aluminum alloy AK12. *Vestnik Ufimskogo gosudarstvennogo aviatsionnogo tekhnicheskogo universiteta*, 2018, vol. 22, no. 3, pp. 10–16. EDN: [YAAWLJ](https://www.edn.ru/yaawlj).
- Pecherskaya E.A., Golubkov P.E., Melnikov O.A., Karpanin O.V., Zinchenko T.O., Artamonov D.V. Intelligent Technology of Oxide Layer Formation by Micro-Arc Oxidation. *IEEE Transactions on Plasma Science*, 2021, vol. 49, no. 9, pp. 2613–2617. DOI: [10.1109/TPS.2021.3091830](https://doi.org/10.1109/TPS.2021.3091830).
- Jayaraj R.K., Malarvizhi S., Balasubramanian V. Optimizing the micro-arc oxidation (MAO) parameters to attain coatings with minimum porosity and maximum hardness on the friction stir welded AA6061 aluminium alloy welds. *Defence technology*, 2017, vol. 13, no. 2, pp. 111–117. DOI: [10.1016/j.dt.2017.03.003](https://doi.org/10.1016/j.dt.2017.03.003).
- Vakili-Azghandi M., Fattah-alhosseini A., Keshavarz M.K. Optimizing the electrolyte chemistry parameters of PEO coating on 6061 Al alloy by corrosion rate measurement: Response surface methodology. *Measurement*, 2018, vol. 124, pp. 252–259. DOI: [10.1016/j.measurement.2018.04.038](https://doi.org/10.1016/j.measurement.2018.04.038).
- Yang S. *On-line test method of micro-arc oxidation load impedance spectroscopy and on-line test system for realizing the method*, patent no. 102621391 CHN, 2012. 10 p.
- Guo Y. *On-line Monitoring System of Micro-arc Oxidation Film Formation Process*, patent no. 111647924 CHN, 2021. 11 p.
- Golubkov P.E. Analysis of the applicability of thickness measurement methods dielectric layers in controlled synthesis protective coatings by micro-arc method oxygenating. *Izmerenie. Monitoring. Upravlenie. Kontrol*, 2020, no. 1, pp. 81–92. DOI: [10.21685/2307-5538-2020-1-11](https://doi.org/10.21685/2307-5538-2020-1-11).
- Bespalova Zh.I., Panenko I.N., Dubovskov V.V., Kozachenko P.N., Kudryavtsev Yu.D. Investigation of the formation of optical black oxide-ceramic coatings on the surface of aluminum alloy 1160. *Izvestiya vysshikh uchebnykh zavedeniy. Severo-Kavkazskiy region. Estestvennye nauki*, 2012, no. 5, pp. 63–66. EDN: [PFATGJ](https://www.edn.ru/pfatgj).
- Mukaeva V.R., Gorbatkov M.V., Farrakhov R.G., Parfenov E.V. A study of the acoustic characteristics of plasma electrolytic oxidation of aluminum. *Elektrotekhnicheskie i informatsionnye komplekсы i sistemy*, 2018, vol. 14, no. 3, pp. 60–65. EDN: [YSAZNZ](https://www.edn.ru/ysaznz).
- Boinet M., Verdier S., Maximovitch S., Dalard F. Application of acoustic emission technique for in situ study of plasma anodizing. *NDT&E International*, 2004, vol. 37, no. 3, pp. 213–219. DOI: [10.1016/j.ndteint.2003.09.011](https://doi.org/10.1016/j.ndteint.2003.09.011).
- Chen Z., Zhang L., Liu H. et al. 3D printing technique-improved phase-sensitive OTDR for breakdown discharge detection of gas-insulated switchgear. *Sensors*, 2020, vol. 20, no. 4, article number 1045. DOI: [10.3390/s20041045](https://doi.org/10.3390/s20041045).
- Bashkov O., Li X., Bao F., Kim V.A., Zhou C. Acoustic emission that occurs during the destruction of coatings applied by microarc oxidation on an aluminum alloy. *Materials Today: Proceedings*, 2019, vol. 19-5, pp. 2522–2525. DOI: [10.1016/j.matpr.2019.08.174](https://doi.org/10.1016/j.matpr.2019.08.174).
- Jadhav P., Bongale A., Kumar S. The effects of processing parameters on the formation of oxide layers in aluminium alloys using plasma electrolytic oxidation technique. *Journal of the Mechanical Behavior of Materials*, 2021, vol. 30, no. 1, pp. 118–129. DOI: [10.1515/jmbm-2021-0013](https://doi.org/10.1515/jmbm-2021-0013).
- Cao J., Fang Z., Chen J., Chen Z., Yin W., Yang Y., Zhang W. Preparation and Properties of Micro-arc Oxide Film with Single Dense Layer on Surface of 5083 Aluminum Alloy. *Journal of Chinese Society for Corrosion and Protection*, 2020, vol. 40, no. 3, pp. 251–258. DOI: [10.11902/1005.4537.2019.069](https://doi.org/10.11902/1005.4537.2019.069).
- Bashkov O.V., Bao F., Li X., Bashkova T.I. Investigation of the Influence of Electrical Modes on the Morphology and Properties of Oxide Coatings on Aluminum Alloy 1163, Obtained by the Micro-arc Oxidation. *Lecture notes in networks and systems*, 2021, vol. 200, pp. 87–95. DOI: [10.1007/978-3-030-69421-0\\_10](https://doi.org/10.1007/978-3-030-69421-0_10).

## СПИСОК ЛИТЕРАТУРЫ

- Yerokhin A., Nie X., Leyland A., Matthews A., Dowe J. Plasma electrolysis for surface engineering // *Surface and coatings technology*. 1999. Vol. 122. № 2-3. P. 73–93. DOI: [10.1016/S0257-8972\(99\)00441-7](https://doi.org/10.1016/S0257-8972(99)00441-7).
- Печерская Е.А., Голубков П.Е., Карпанин О.В., Козлов Г.В., Зинченко Т.О., Смогунов В.В. Влияние технологических параметров на свойства покрытий,

- синтезируемых методом микродугового оксидирования // Измерение. Мониторинг. Управление. Контроль. 2020. № 2. С. 89–99. DOI: [10.21685/2307-5538-2020-2-11](https://doi.org/10.21685/2307-5538-2020-2-11).
3. Shi M., Li H. The mathematical mode of Ti alloy micro-arc oxidation process parameters and ceramic coating and experimental study // Journal of Yunnan University: Natural Sciences Edition. 2015. Vol. 37. № 1. P. 102–110.
  4. Chen H., Hao J., Feng Z. Micro-arc oxidation mechanism and electrical discharge model // Journal of Changan University (Natural Science Edition). 2008. Vol. 28. P. 116–119.
  5. Голубков П.Е., Печерская Е.А., Артамонов Д.В., Зинченко Т.О., Герасимова Ю.Е., Розенберг Н.В. Электрофизическая модель процесса микродугового оксидирования // Известия высших учебных заведений. Физика. 2019. Т. 62. № 11. С. 166–171. DOI: [10.17223/00213411/62/11/166](https://doi.org/10.17223/00213411/62/11/166).
  6. Дударева Н.Ю., Ахмедзянов Д.А. Трибологические параметры МДО-слоев, сформированных в силикатно-щелочном электролите на образцах из высококремниевое алюминиевого сплава АК12 // Вестник Уфимского государственного авиационного технического университета. 2018. Т. 22. № 3. С. 10–16. EDN: [YAAWLJ](https://www.edn.ru/yaawlj/).
  7. Pecherskaya E.A., Golubkov P.E., Melnikov O.A., Karpanin O.V., Zinchenko T.O., Artamonov D.V. Intelligent Technology of Oxide Layer Formation by Micro-Arc Oxidation // IEEE Transactions on Plasma Science. 2021. Vol. 49. № 9. P. 2613–2617. DOI: [10.1109/TPS.2021.3091830](https://doi.org/10.1109/TPS.2021.3091830).
  8. Jayaraj R.K., Malarvizhi S., Balasubramanian V. Optimizing the micro-arc oxidation (MAO) parameters to attain coatings with minimum porosity and maximum hardness on the friction stir welded AA6061 aluminium alloy welds // Defence technology. 2017. Vol. 13. № 2. P. 111–117. DOI: [10.1016/j.dt.2017.03.003](https://doi.org/10.1016/j.dt.2017.03.003).
  9. Vakili-Azghandi M., Fattah-alhosseini A., Keshavarz M.K. Optimizing the electrolyte chemistry parameters of PEO coating on 6061 Al alloy by corrosion rate measurement: Response surface methodology // Measurement. 2018. Vol. 124. P. 252–259. DOI: [10.1016/j.measurement.2018.04.038](https://doi.org/10.1016/j.measurement.2018.04.038).
  10. Yang S. On-line test method of micro-arc oxidation load impedance spectroscopy and on-line test system for realizing the method: patent № 102621391 CHN, 2012. 10 p.
  11. Guo Y. On-line Monitoring System of Micro-arc Oxidation Film Formation Process: patent № 111647924 CHN, 2021. 11 p.
  12. Голубков П.Е. Анализ применимости методов измерения толщины диэлектрических слоев при управляемом синтезе защитных покрытий методом микродугового оксидирования // Измерение. Мониторинг. Управление. Контроль. 2020. № 1. С. 81–92. DOI: [10.21685/2307-5538-2020-1-11](https://doi.org/10.21685/2307-5538-2020-1-11).
  13. Беспалова Ж.И., Паненко И.Н., Дубовсков В.В., Козаченко П.Н., Кудрявцев Ю.Д. Исследование процесса формирования оптически черных оксидно-керамических покрытий на поверхности алюминиевого сплава 1160 // Известия высших учебных заведений. Северо-Кавказский регион. Естественные науки. 2012. № 5. С. 63–66. EDN: [PFATGJ](https://www.edn.ru/pfatgj/).
  14. Мукаева В.Р., Горбатков М.В., Фаррахов Р.Г., Парфенов Е.В. Исследование акустических характеристик процесса плазменно-электролитического оксидирования алюминия // Электротехнические и информационные комплексы и системы. 2018. Т. 14. № 3. С. 60–65. EDN: [YSAZNZ](https://www.edn.ru/ysaznz/).
  15. Boinet M., Verdier S., Maximovitch S., Dalard F. Application of acoustic emission technique for in situ study of plasma anodizing // NDT&E International. 2004. Vol. 37. № 3. P. 213–219. DOI: [10.1016/j.ndteint.2003.09.011](https://doi.org/10.1016/j.ndteint.2003.09.011).
  16. Chen Z., Zhang L., Liu H. et al. 3D printing technique-improved phase-sensitive OTDR for breakdown discharge detection of gas-insulated switchgear // Sensors. 2020. Vol. 20. № 4. Article number 1045. DOI: [10.3390/s20041045](https://doi.org/10.3390/s20041045).
  17. Bashkov O., Li X., Bao F., Kim V.A., Zhou C. Acoustic emission that occurs during the destruction of coatings applied by microarc oxidation on an aluminum alloy // Materials Today: Proceedings. 2019. Vol. 19-5. P. 2522–2525. DOI: [10.1016/j.matpr.2019.08.174](https://doi.org/10.1016/j.matpr.2019.08.174).
  18. Jadhav P., Bongale A., Kumar S. The effects of processing parameters on the formation of oxide layers in aluminium alloys using plasma electrolytic oxidation technique // Journal of the Mechanical Behavior of Materials. 2021. Vol. 30. № 1. P. 118–129. DOI: [10.1515/jmbm-2021-0013](https://doi.org/10.1515/jmbm-2021-0013).
  19. Cao J., Fang Z., Chen J., Chen Z., Yin W., Yang Y., Zhang W. Preparation and Properties of Micro-arc Oxide Film with Single Dense Layer on Surface of 5083 Aluminum Alloy // Journal of Chinese Society for Corrosion and Protection. 2020. Vol. 40. № 3. P. 251–258. DOI: [10.11902/1005.4537.2019.069](https://doi.org/10.11902/1005.4537.2019.069).
  20. Bashkov O.V., Bao F., Li X., Bashkova T.I. Investigation of the Influence of Electrical Modes on the Morphology and Properties of Oxide Coatings on Aluminum Alloy 1163, Obtained by the Micro-arc Oxidation // Lecture notes in networks and systems. 2021. Vol. 200. P. 87–95. DOI: [10.1007/978-3-030-69421-0\\_10](https://doi.org/10.1007/978-3-030-69421-0_10).

## Исследование влияния режимов микродугового оксидирования на морфологию и параметры оксидного покрытия, наносимого на алюминиевый сплав Д16АТ

© 2023

**Бао Фэнюань**<sup>1,3</sup>, младший научный сотрудник, инженер-исследователь

**Башков Олег Викторович**<sup>\*1,4</sup>, доктор технических наук, профессор, заведующий кафедрой «Материаловедение и технология новых материалов»

**Чжан Дан**<sup>2,5</sup>, доктор технических наук, профессор, заведующий лабораторией «Машиностроение»

**Люй Лань**<sup>1,2</sup>, аспирант

**Башкова Татьяна Игоревна**<sup>1,6</sup>, кандидат технических наук, доцент

<sup>1</sup>Комсомольский-на-Амуре государственный университет, Комсомольск-на-Амуре (Россия)

<sup>2</sup>Хэйлунцзянский университет науки и технологий, Харбин (Китай)

\*E-mail: bashkov@knastu.ru

<sup>3</sup>ORCID: <https://orcid.org/0000-0001-5762-7953>

<sup>4</sup>ORCID: <https://orcid.org/0000-0002-3910-9797>

<sup>5</sup>ORCID: <https://orcid.org/0000-0003-4150-7038>

<sup>6</sup>ORCID: <https://orcid.org/0000-0001-7070-5821>

Поступила в редакцию 06.12.2022

Принята к публикации 19.01.2023

**Аннотация:** Эффективным способом защиты вентиляльных металлов и их сплавов является метод микродугового оксидирования (МДО), в настоящее время применяемый в различных отраслях. Однако для достижения желаемых характеристик и свойств оксидных покрытий требуется большое число экспериментов по определению оптимального режима оксидирования, что делает метод МДО трудоемким и ресурсозатратным. Одним из путей решения данной проблемы является поиск информативного параметра или нескольких параметров, использование которых при мониторинге процесса оксидирования позволит установить связь между режимами МДО и заданными характеристиками оксидных покрытий. В работе изучено влияние заданных технологических режимов МДО (плотности тока, времени оксидирования, регистрируемой в процессе МДО амплитуды сигналов акустической эмиссии (АЭ)) на морфологию и параметры оксидных покрытий (толщину  $\delta$  и шероховатость поверхности  $R_a$ ), наносимых на алюминиевый сплав Д16АТ, плакированный чистым алюминием. Многофакторное планирование эксперимента и проведенный регрессионный анализ позволили установить связь между двумя факторами оксидирования (плотностью тока и временем оксидирования) и параметрами получаемых покрытий. Предложен дополнительный фактор, определяемый в режиме мониторинга в процессе оксидирования как время от момента достижения максимума или минимума регистрируемой в процессе МДО амплитуды АЭ до окончания процесса оксидирования. Установлено, что введение дополнительного фактора позволяет существенно повысить достоверность зависимости между параметрами покрытий, получаемыми экспериментально и расчетным методом на основе регрессионного анализа. Отмечено, что при выполнении МДО высокая достоверность между расчетными и фактическими значениями параметров оксидных покрытий может быть достигнута при дополнительном мониторинге процесса МДО путем регистрации амплитуды АЭ.

**Ключевые слова:** микродуговое оксидирование; оксидное покрытие; акустическая эмиссия; многофакторный анализ; морфология поверхности; алюминиевый сплав; Д16АТ; сплавы вентиляльной группы.

**Благодарности:** Работа выполнена при поддержке гранта Президента РФ для государственной поддержки ведущих научных школ Российской Федерации (проект НШ-452.2022.4).

**Для цитирования:** Бао Ф., Башков О.В., Чжан Д., Люй Л., Башкова Т.И. Исследование влияния режимов микродугового оксидирования на морфологию и параметры оксидного покрытия, наносимого на алюминиевый сплав Д16АТ // Frontier Materials & Technologies. 2023. № 1. С. 7–21. DOI: 10.18323/2782-4039-2023-1-7-21.



## Numerical modeling of temperature fields during friction stir welding of the AA5083 aluminum alloy

© 2023

*Igor N. Zybin*<sup>\*1</sup>, PhD (Engineering), Associate Professor, assistant professor of Chair “Material Bonding and Processing Technology”  
*Mikhail S. Antokhin*<sup>2</sup>, graduate student of Chair “Material Bonding and Processing Technology”  
Kaluga Branch of Bauman Moscow State Technical University, Kaluga (Russia)

\*E-mail: igor.zybin@mail.ru

<sup>1</sup>ORCID: <https://orcid.org/0000-0002-5738-4231>

<sup>2</sup>ORCID: <https://orcid.org/0000-0002-8043-1606>

Received 12.12.2022

Accepted 30.01.2023

**Abstract:** One of the important parameters ensuring the production of a welded joint without continuity defects during friction stir welding is the provision of the required temperature in the metal bonding zone. Significant difficulties arise when determining experimentally the temperature directly in the stir zone of metals using thermocouples. In this regard, the application of numerical methods describing the distribution of temperature fields during friction stir welding is relevant. In the work, numerical modeling of temperature fields during friction stir welding was used, which was based on the finite element method using Abaqus/Explicit software. Modeling was carried out taking into account the coupled Euler – Lagrange approach, the Johnson – Cook plasticity model, and the Coulomb friction law. Using the finite element method, the models of a part, substrate, and tool were constructed taking into account their thermophysical properties. To reduce the computation time, an approach based on the metal mass scaling by recalculating the density of the metal and its thermal properties was used. The authors matched coefficients of scaling of the material mass and heat capacity for the selected welding mode parameters. To evaluate the validity of the results of numerical modeling of temperature fields during friction stir welding, the experimental research of the temperature fields using thermocouples was carried out. The paper shows the possibility of numerical modeling of temperature fields during friction stir welding with the help of the coupled Euler – Lagrange approach and Abaqus/Explicit software. Due to the application of the approach associated with material mass scaling, the calculation time is reduced by more than 10 times.

**Keywords:** friction stir welding; AA5083; coupled Euler – Lagrange approach; numerical modeling of temperature fields.

**For citation:** Zybin I.N., Antokhin M.S. Numerical modeling of temperature fields during friction stir welding of the AA5083 aluminum alloy. *Frontier Materials & Technologies*, 2023, no. 1, pp. 23–32. DOI: 10.18323/2782-4039-2023-1-23-32.

### INTRODUCTION

Friction stir welding (FSW) is one of the modern and advanced methods for producing goods from aluminum alloys. The formation of a welded joint is carried out in the solid phase without melting the parts to be joined, which is the advantage of this method compared to the traditional arc welding methods. The strength of welded joints produced by FSW, as a rule, is 90–95 % of the base metal strength [1–3]; however, it can reach the strength of the base metal as well. Bending tests show that the destruction of welded samples occurs along the base metal [1].

The main parameters of the process, characterizing the welded joint formation during FSW without defects include the provision of the required temperature in the welding zone. The base amount of heat is released as a result of friction of a tool with the parts to be welded. In this case, the amount of heat released during welding affects the seam structure, the width of a heat-affected zone and the welded joint quality. The geometric shape of a tool pin significantly influences the processes of heat generation.

To determine the temperatures in the metal joining zone during FSW, experimental and theoretical studies are used.

Thermocouples are widely used in experimental studies. At the same time, it is virtually impossible to determine the temperature using thermocouples directly in the mixing zone of metals. Moreover, such studies require significant time expenditures (thermocouples preparation and fullering). In this regard, the numerical methods are widely used to study the distribution of temperature fields during FSW. As a rule, these methods are based on the use of the finite element method.

Finite element models used in FSW can be divided into three types: thermal, thermomechanical without flow, and thermomechanical models with flow. According to the Lagrange approach, in the models with flow, the elements can be strongly distorted and the final results may be inaccurate. To avoid grid distortion, several modelling methods are used: the adaptive model grid refinement and the arbitrary Euler – Lagrange approach. The flow-based models are developed using the computational fluid dynamics software systems. The impossibility to take into account the hardening of the material is a disadvantage of this method, since here a rigid-viscous-plastic material is considered.

The flow-based models are also developed using the coupled Euler – Lagrange approach [4–6]. This method of analysis combines two approaches: Euler’s and

Lagrange's. A tool is modeled as a rigid isothermal Lagrange body, and has a "reference point" control point, and a part is modelled using the Euler approach. With the help of a contact, the direct interaction of a tool and a part is simulated [6]. The works [7; 8] prove the efficiency of applying the coupled Euler – Lagrange approach when modelling the FSW process. Therefore, to obtain proper results when studying the distribution of temperature fields during FSW, the coupled Euler – Lagrange approach should be used. However, one should take into account the change in the material thermo-physical properties depending on the temperature [9; 10], and the Johnson – Cook material plasticity model, the utilization efficiency of which is proved by the results of experimental tests in the work [11] during the numerical modelling of the FSW process.

The FSW studies are carried out in various commercial software, such as: ABAQUS, DEFORM-3D, ANSYS, FORGE 3, LS-DYNA. However, the thermomechanical models built in DEFORM-3D and ABAQUS turned out to be better than the models built in other software, which allowed obtaining a theoretical distribution of temperature fields relevant to the experimental data.

It is also important to significantly reduce the time of theoretical calculations when developing a model, since such calculations can take up to 500 hours or more, depending on the personal computer capabilities, the task complexity, and the weld length. To reduce the calculation time, two approaches are used: "Time Scaling" and "Mass Scaling" under the condition that the deformation rates and inertial forces remain small. Mass scaling is carried out by recalculating the metal density. Time scaling is carried out by replacing the time with a fictitious variable. However, in both cases, to maintain the proper distribution and take into account the heating temperature, the material thermal properties are recalculated. These approaches allow saving the calculation time without the loss of the result accuracy.

The study is aimed at the computer simulation of the distribution of temperature fields during FSW of the AA5083 aluminum alloy, based on the coupled Euler – Lagrange approach, which reduces the time of theoretical calculations virtually with no loss of their accuracy.

## METHODS

Modelling of the distribution of temperature fields during welding of the AA5083 aluminum alloy was carried out in the Abaqus/Explicit software product. The model was based on the coupled Euler – Lagrange approach and on an explicit integration scheme designed to calculate non-stationary dynamics, quasi-statics, and rapid processes. The Abaqus/Explicit software product allows applying the Coulomb friction law, the Johnson – Cook material plasticity model, and includes discontinuous nonlinear behaviour.

To simulate the temperature fields during FSW, a joint solution of strength and fluid dynamics tasks is used – the coupled Euler – Lagrange approach in a three-dimensional formulation [12; 13]. This method allows simulating fluid dynamics tasks on the Euler grids and dynamic

strength problems on the Lagrange grid within a single spatial solution.

The model included a part, a substrate, and a tool. In this respect, the material of the part and the substrate was modelled within the Euler approach, and the tool material was modelled within the Lagrange approach [14]. The peculiarity of such simulation is that the generation of a finite element grid on the part and substrate was performed only on the area constructed within the Euler approach.

The Lagrange grid nodes are connected to the material. The model grid elements and the boundaries of these grid elements coinciding with the boundaries of the material are deformed under the force action. The Lagrange grid elements themselves are filled with the material. The finite element models of the part, substrate, and the tool with the substrate were constructed using the EC3D8RT and C3D8RT elements, respectively, which are three-dimensional eight-node elements. In the nodes of model elements, four degrees of freedom were available: movements along three mutually perpendicular axes and the temperature degree of freedom.

The contact between the model elements took into account the Coulomb friction law, where the sliding friction force is proportional to the normal force acting between the bodies. The sliding friction coefficient for a metal-metal pair is usually in the range of 0.15–0.3. Within the numerical modelling, its value, as a rule, is assumed to be constant [15]. To simulate the distribution of temperature fields, the sliding friction coefficient was chosen to be 0.15.

Modelling of the distribution of temperature fields was performed for the base metal in the form of a sheet of the AA5083 alloy 5 mm thick. An AISI 1020 steel sheet 10 mm thick was chosen as a substrate material. The welding mode was chosen taking into account the absence of continuity defects in the welding zone: the tool rotation speed is 560 rpm, the welding speed (the longitudinal tool feed) is 40 mm/min. The angle of tool inclination to the vertical was 2°. The depth of penetration of a tool shoulder into the part is 0.1 mm. The geometric dimensions of the tool are shown in Fig. 1.

Fig. 2 shows the models of a part with a substrate and a tool constructed using the finite element method. The model of the part with a substrate included 6000 elements, and the model of the tool – 2741 elements.

To account for the plastic deformation of the model elements, the empirical Johnson – Cook plasticity model was used, which took into account kinematic hardening, the effects of isotropic hardening, the deformed metal adiabatic heating, and the temperature changes. In this model, the yield strength is determined by the following formula [16; 17]:

$$\sigma_y = \left[ A + B \cdot \varepsilon_p^n \right] \cdot \left[ 1 + C \cdot \ln \left( \frac{\varepsilon_p^n}{\varepsilon_0} \right) \right] \cdot \left[ 1 - \left( \frac{T - T_r}{T_m - T_r} \right)^m \right], \quad (1)$$

where  $\sigma_y$  – is the yield strength;

$\varepsilon_p^n$  – is the effective plastic strain;

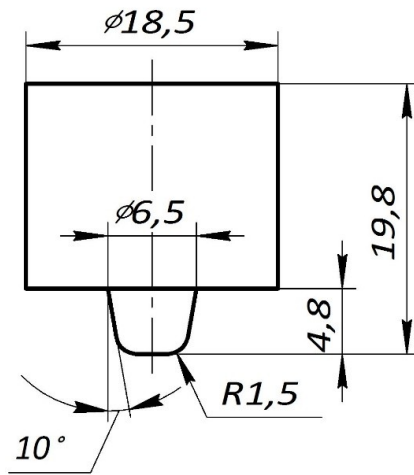


Fig. 1. FSW tool dimensions  
Рис. 1. Размеры инструмента для СТП

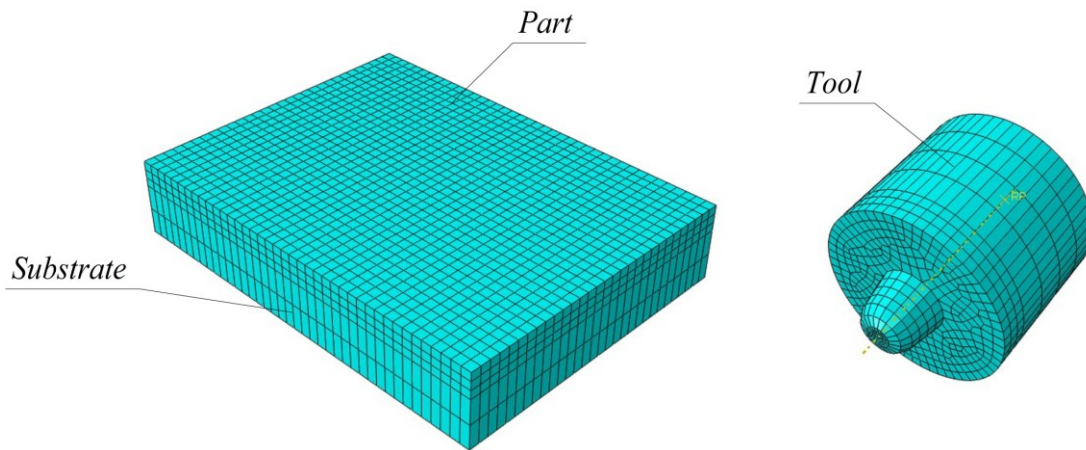


Fig. 2. Finite element models of the part, substrate, and tool  
Рис. 2. Модели детали, подложки и инструмента, построенные с помощью метода конечных элементов

$T_m$  – is the melting temperature;  
 $T_r$  – is the room temperature;  
 $T$  – is the material temperature;  
 $A, B, C, n, m, \varepsilon_0$  – are the model parameters.

The model parameters (1) are shown in Table 1.

In the current work, an approach related to metal mass scaling is selected to reduce the calculation time.

The metal density was calculated as per the formula

$$\rho^* = k_m \cdot \rho, \quad (2)$$

where  $\rho^*$  – is the fictitious density;  
 $k_m$  – is the scaling ratio determining what fold approximately the calculation time will be reduced ( $k_m > 1$ );  
 $\rho$  – the material density.

The scaling ratio  $k_m$  is chosen so that the inertial forces on the right side of an equation (2) remain small.

The scaling ratio value is chosen equal to  $k_m = 400$ . When solving the formulated task, the Navier thermoelasticity equation is used:

$$\mu \cdot \nabla^2 \cdot u + (\lambda + \mu) \cdot \nabla \cdot \text{tr}(E) - \alpha \cdot \lambda \cdot \nabla \cdot T = \rho \cdot \frac{\partial u}{\partial t^2}, \quad (3)$$

where  $E$  – is the linear strain tensor;  
 $\mu$  and  $\lambda$  – are the Lamé coefficients;  
 $T$  – is the temperature;  
 $\alpha$  – is the thermal expansion coefficient;  
 $u$  – is the displacement vector;  
 $\rho$  – is the density;  
 $t$  – is the time;  
 $\nabla$  – is the nabla operator;  
 $\text{tr}$  – is the  $E$  matrix trace.

When replacing the density with a fictitious one, thermal constants change. The influence of this effect was compensated by recalculating the material heating capacity as per the formula

$$c_e^* = c_e \cdot k_n^{-1}, \tag{4}$$

where  $c_e^*$  – is the fictitious density;  
 $k_n$  – is the heating capacity scaling ratio;  
 $c_e$  – is the material heating capacity.

Since the value of the right side of the equation (3) has increased, the minimum stable time increment of the explicit solver increases [23].

The heating capacity scaling factor  $k_n$  was selected to reduce the calculation time, while providing the accuracy comparable to that when simulating the distribution of temperature fields without the metal mass scaling. The heating capacity scaling ratio  $k_n$  was assumed to be equal to the mass scaling factor  $k_m=400$ .

To verify the validity of the computer simulation results, the authors carried out an experiment on butt welding of two parts 5 mm thick made of the AA5083 aluminium alloy. Welding was performed on a FSS400R vertical turning mill using a tool, the geometric dimensions of which are shown in Fig. 1. The tool was made of H13 tool die steel. The tool hardness was 53...57 HRC after quenching in oil and next tempering. To study temperature fields, the authors used a LTR modular data acquisition system with an LGraph2 multichannel recorder and a K-type thermocouple (chromel-alumel).

A thermocouple layout is shown in Fig. 3. To improve the accuracy of the results of obtaining the distribution of temperature fields, two groups of thermocouples were prepared.

**RESULTS**

The temperature distribution on the surface of welded parts during computer simulation of the FSW process without mass scaling and with scaling ( $k_m=k_n=400$ ) is shown in Fig. 4.

From Fig. 4, it is evident that with the selected scaling factors, the distribution of temperature fields differs significantly. Therefore, it was necessary to update the scaling factor  $k_n$ . Based on the comparative analysis of the obtained temperature fields without and with scaling, the heating capacity scaling ratio was assumed to be 257. After that, the simulation of the temperature fields' distribution was repeated. Fig. 5 shows the temperature distribution on the surface of welded parts during computer simulation of the FSW process without mass scaling and with scaling ( $k_m=400$ ;  $k_n=257$ ). According to the simulation results, the welding area maximum temperature was 584 °C.

Fig. 6 shows the location of thermocouples before welding (a) and after welding (b) of parts during the investigational study when producing a butt welded joint.

The results of the investigational study are shown in Fig. 7.

Fig. 8 presents the experimental data and data obtained during numerical modelling for the considered points of installing the 1 and 2 thermocouples.

**DISCUSSION**

The analysis of the obtained distribution of temperature fields presented in Fig. 5 showed a slight difference between this distribution when using mass scaling and without scaling. With the selected scaling factors, the distribution of isotherms differs by no more than 6 %. In this case, the calculation time was reduced from 600–700 hours (approximate value) to 60 hours.

The maximum temperature values in the welding area obtained in this work as a result of numerical modeling (584 °C) are in good agreement with data of some works where the FSW process simulation was performed. In particular, in the work [19], during numerical modelling of temperature fields when producing a FSW butt joint, the maximum temperature in the welding area was 585 °C. When obtaining T-formed welded joints as a result of the FSW process numerical modelling based on the Euler –

*Table 1. The values of the parameters of the Johnson – Cook plasticity model for the AA5083 and AISI 1020 materials [18]*

*Таблица 1. Значения параметров модели пластичности Джонсона – Кука для материалов AA5083 и AISI 1020 [18]*

Parameter	Material	
	AA5083	AISI 1020
<i>A</i>	137.9	187.60
<i>B</i>	216.73	199.10
<i>n</i>	0.4845	0.1717
<i>m</i>	1.2250	0.4437
<i>T<sub>m</sub></i>	659.85	1460.00
<i>T<sub>r</sub></i>	25	25

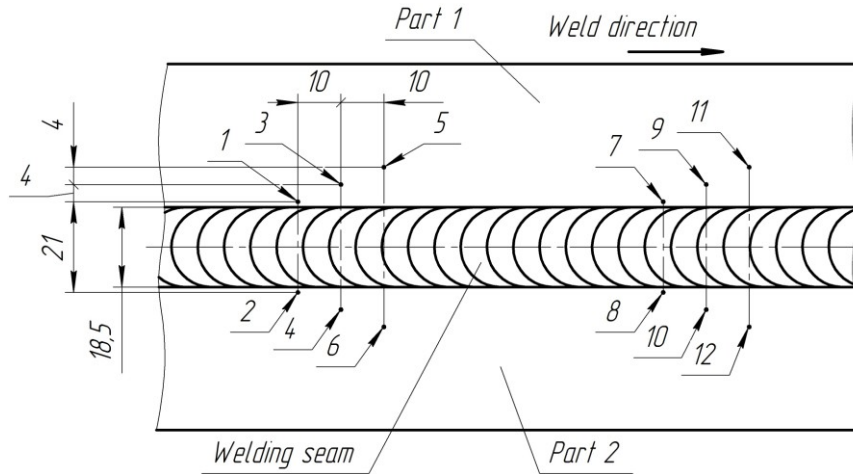


**Fig. 3.** A thermocouples layout: 1–12 – thermocouples installation locations  
**Рис. 3.** Схема расположения термомпар: 1–12 – места установки термомпар

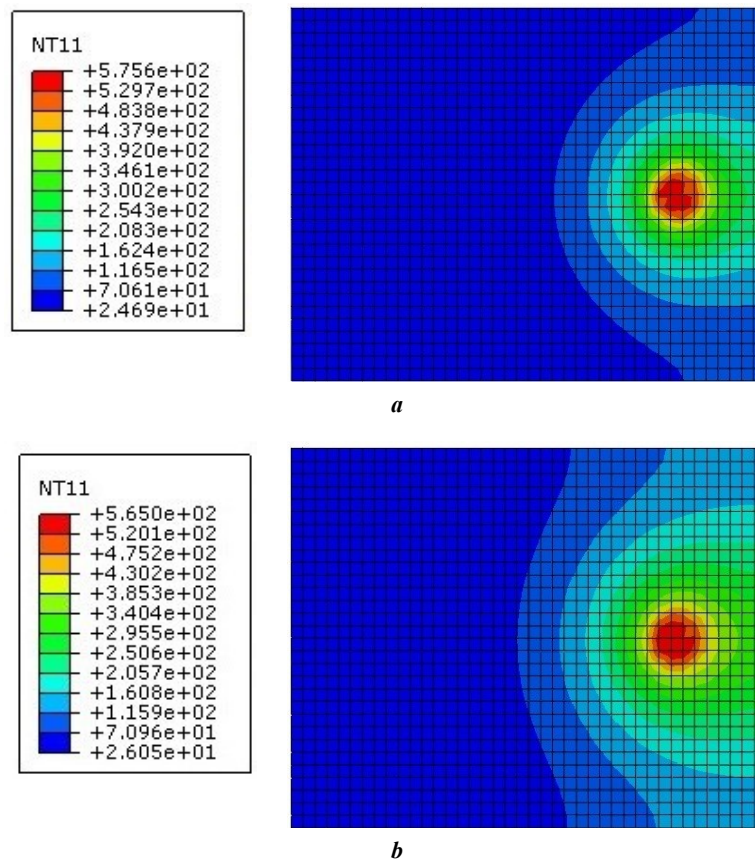


**Fig. 4.** Temperature fields distribution on the surface of welded parts when modeling the FSW process:  
**a** – a model without mass scaling; **b** – a model with mass scaling ( $k_m=k_n=400$ )

**Рис. 4.** Распределение температурных полей на поверхности свариваемых деталей при моделировании процесса СТП:

**a** – модель без применения масштабирования массы;  
**b** – модель с применением масштабирования массы ( $k_m=k_n=400$ )

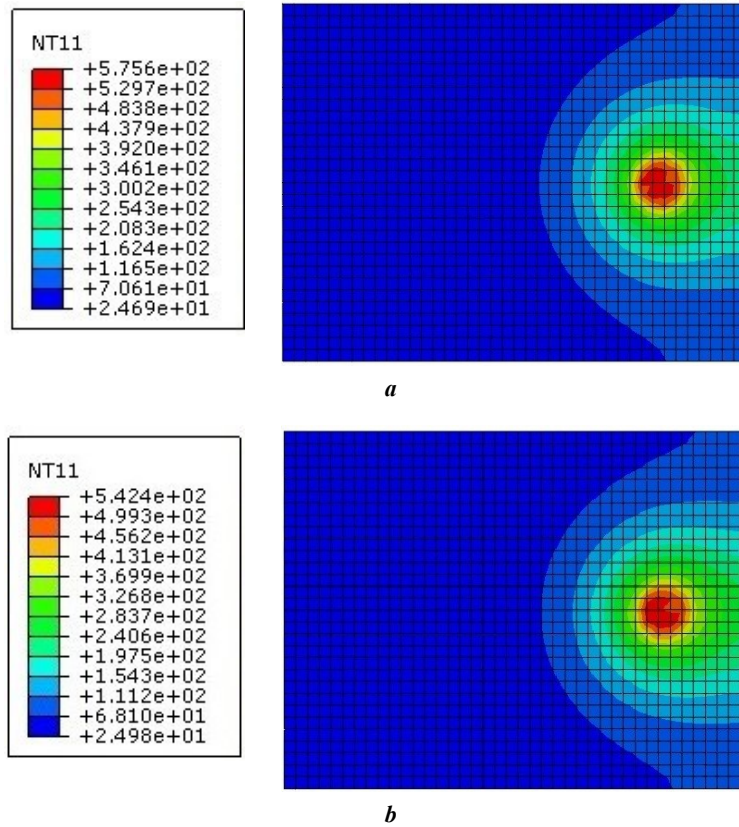


**Fig. 5.** Temperature fields distribution on the surface of welded parts when modeling the FSW process: **a** – a model without mass scaling; **b** – a model with mass scaling ( $k_m=400$ ;  $k_n=257$ )

**Рис. 5.** Распределение температурных полей на поверхности свариваемых деталей при моделировании процесса СТП:

**a** – модель без применения масштабирования массы;

**b** – модель с применением масштабирования массы ( $k_m=400$ ;  $k_n=257$ )

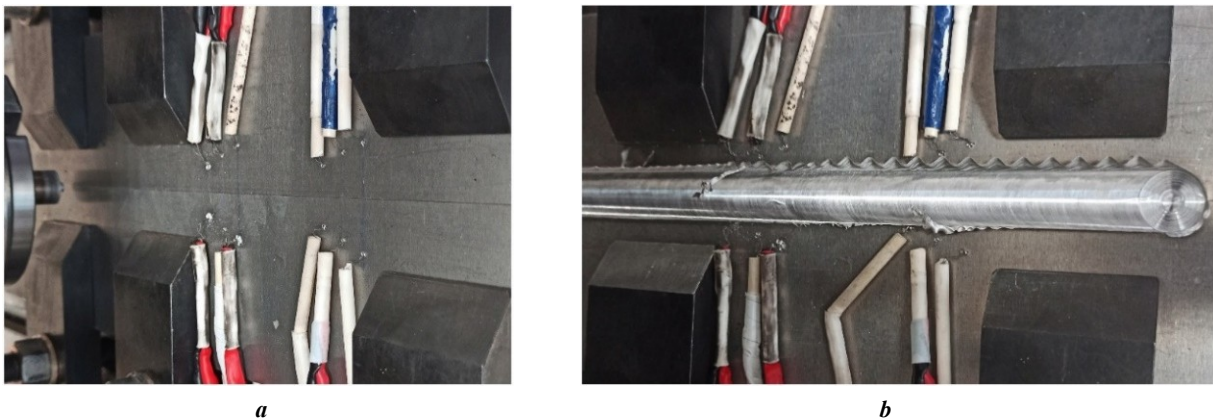


**Fig. 6.** The location of thermocouples before (a) and after (b) welding of parts

**Рис. 6.** Расположение термопар перед (a) и после (b) сварки деталей

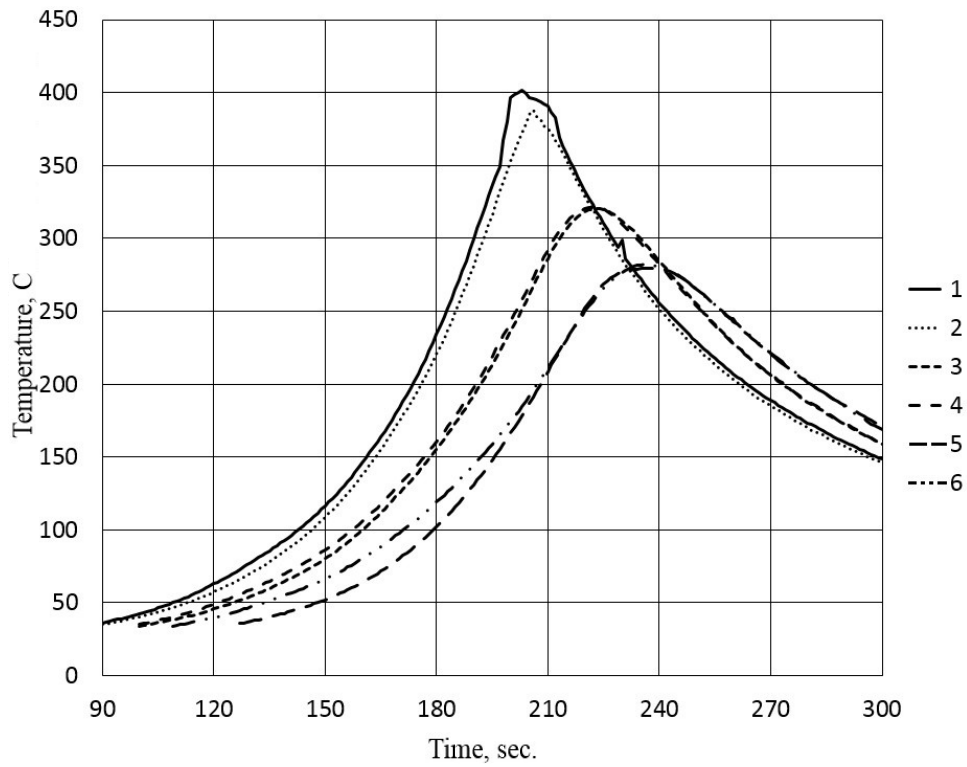


**Fig. 7.** The distribution of temperature fields during friction stir welding: 1–6 – the numbers of thermocouples  
**Рис. 7.** Распределение температурных полей при СТП: 1–6 – номера термопар

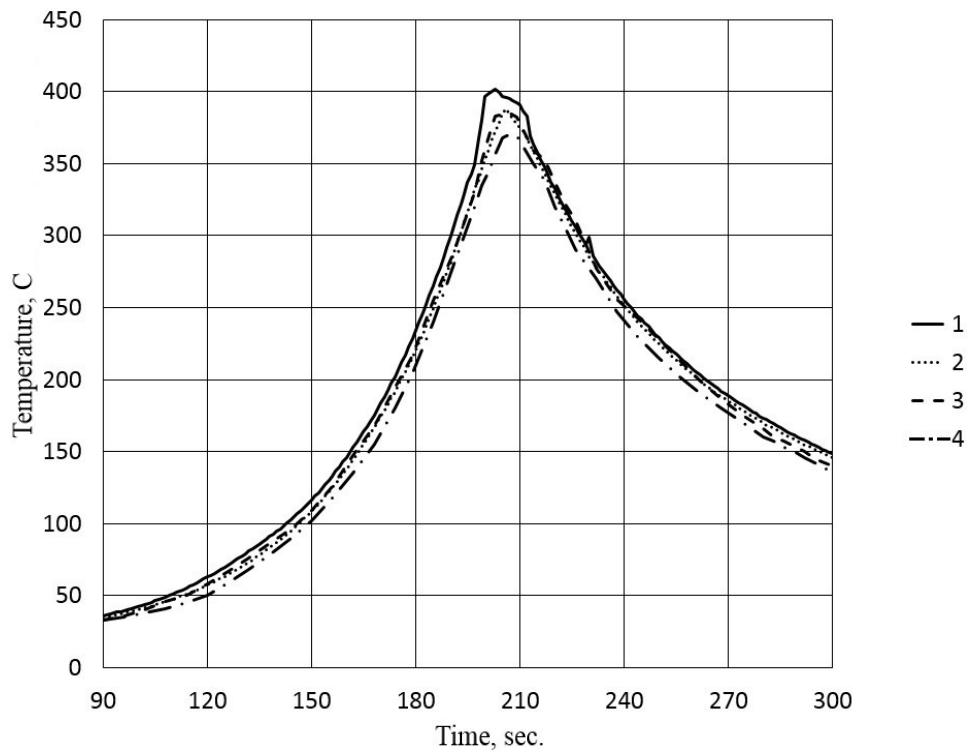


**Fig. 8.** The distribution of temperature fields during friction stir welding obtained by computer modeling and experimentally:  
 1–2 – thermocouples (an experiment); 3–4 – thermocouples (modeling)  
**Рис. 8.** Распределение температурных полей при СТП, полученных с помощью компьютерного моделирования и экспериментальным путем:  
 1–2 – термопары (эксперимент); 3–4 – термопары (моделирование)

Lagrange approach, in the work [20], the maximum temperature in the welding area was 575 °C.

At the periphery of the tool-part contact during welding (thermocouples 1 and 2, Fig. 7), the maximum temperature on the surface of the part on the side of the tool backward slip zone is higher than on the side of the running-on zone. This is explained by the fact that an overpressure zone appears in front of the tool on the side of the running-on zone. From this zone, the tool working surface displaces metal, which is in the plastic state and prevents the tool movement, due to its translational-rotational movement, into the zone located behind the tool, i.e. into the backward slip zone.

## MAIN RESULTS AND CONCLUSIONS

The analysis of the results of experimental investigations showed that at the periphery of the tool-part contact during welding (thermocouples 1 and 2), the maximum temperature reaches 401.6 °C, and the temperature on the part surface on the side of the tool backward slip zone is approximately 14 °C higher than on the side of the tool running-on zone. It is associated with different conditions of metal stirring in the tool running-on and backward slip zones. With an increase in the distance from the welding area in the direction perpendicular to the weld, these temperature changes on the side of the tool backward slip and running-on zones are smoothed.

The values of the maximum temperatures reached during welding at the considered points of installation of thermocouples obtained experimentally and using numerical modelling differ by no more than 5 %. Moreover, the curves describing the nature of temperature changes depending on the time obtained experimentally and theoretically have a similar nature. This indicates the possibility of using computer simulation to estimate the temperature distribution in the welding zone.

The obtained results of the distribution of temperature fields at the periphery of the tool-part contact are in good agreement with the theoretical data existing in the literature, as well as with the data obtained experimentally in this work during butt welding of parts made of the AA5083 aluminum alloy.

Numerical modelling of the distribution of temperature fields during FSW using a thermomechanical model (Abaqus software) taking into account the coupled Euler – Lagrange approach, the Johnson – Cook plasticity model, and the Coulomb friction law was carried out. The results of numerical modelling are proved by the experimental investigation of the distribution of temperature fields when producing a butt welded joint made of the AA5083 aluminum alloy 5 mm thick. The difference between the theoretical and experimental results does not exceed 5 %.

The application of the approach based on the metal mass scaling during numerical modelling of temperature fields by recalculating the metal density and thermal properties allows reducing the time for theoretical calculations by more than one order.

## REFERENCES

- Ishchenko A.Ya., Podelnikov S.V., Poklyatskiy A.G. Friction stir welding of aluminium alloys (Review). *Avtomaticheskaya svarka*, 2007, no. 11, pp. 32–38.
- Arbegast W.J. Friction stir welding after a decade of development. *Welding Journal*, 2006, vol. 85, no. 3, pp. 28–35.
- Okamura H., Aota K., Ezumi M. Friction stir welding of aluminum alloy and application to structure. *Journal of Japan Institute of Light Metals*, 2000, vol. 50, no. 4, pp. 166–172. DOI: [10.2464/jilm.50.166](https://doi.org/10.2464/jilm.50.166).
- Salloomi K.N., Hussein F.I., Al-Sumaidae S.N.M. Temperature and stress evaluation during three different phases of friction stir welding of AA 7075-T651 alloy. *Modelling and Simulation in Engineering*, 2020, vol. 2020, pp. 1–11. DOI: [10.1155/2020/3197813](https://doi.org/10.1155/2020/3197813).
- Ragab M., Liu H., Yang G.-J., Ahmed M.M.Z. Friction stir welding of 1Cr11Ni2W2MoV martensitic stainless steel: Numerical simulation based on coupled Eulerian Lagrangian approach supported with experimental work. *Applied Science*, 2021, vol. 11, no. 7, pp. 1–6. DOI: [10.3390/app11073049](https://doi.org/10.3390/app11073049).
- Chauhan P., Jain R., Pal S.K., Singh S.B. Modeling of defects in friction stir welding using coupled Eulerian and Lagrangian method. *Journal of Manufacturing Processes*, 2018, vol. 34-A, pp. 158–166. DOI: [10.1016/j.jmapro.2018.05.022](https://doi.org/10.1016/j.jmapro.2018.05.022).
- Meyghani B., Awang M.B., Emamian S.S., Mohd Nor M.K.B., Pedapati S.R. A Comparison of Different Finite Element Methods in the Thermal Analysis of Friction Stir Welding (FSW). *Metals*, 2017, vol. 7, no. 10, article number 450. DOI: [10.3390/met7100450](https://doi.org/10.3390/met7100450).
- Andrade D.G., Leitão C., Dialami N., Chiumenti M., Rodrigues D.M. Modelling torque and temperature in friction stir welding of aluminium alloys. *International Journal of Mechanical Sciences*, 2020, vol. 182, article number 105725. DOI: [10.1016/j.ijmecsci.2020.105725](https://doi.org/10.1016/j.ijmecsci.2020.105725).
- El-Sayed M.M., Shash A.Y., Mahmoud T.S., Rabbou M.A. Effect of friction stir welding parameters on the peak temperature and the mechanical properties of aluminum alloy 5083-O. *Advanced Structured Materials*, 2018, vol. 72, pp. 11–25. DOI: [10.1007/978-3-319-59590-0\\_2](https://doi.org/10.1007/978-3-319-59590-0_2).
- El-Sayed M.M., Shash A.Y., Abd-Rabou M. Finite element modeling of aluminum alloy AA5083-O friction stir welding process. *Journal of Materials Processing Technology*, 2018, vol. 252, pp. 13–24. DOI: [10.1016/j.jmatprotec.2017.09.008](https://doi.org/10.1016/j.jmatprotec.2017.09.008).
- Patil S., Tay Y.Y., Baratzadeh F., Lankarani H. Modeling of friction-stir butt-welds and its application in automotive bumper impact performance. Part 1. Thermo-mechanical weld process modeling. *Journal of Mechanical Science and Technology*, 2018, vol. 32, no. 6, pp. 2569–2575. DOI: [10.1007/s12206-018-0514-0](https://doi.org/10.1007/s12206-018-0514-0).
- Lia K., Jarrara F., Sheikh-Ahmada J., Ozturkb F. Using coupled Eulerian Lagrangian formulation for accurate modeling of the friction stir welding process. *Procedia Engineering*, 2017, vol. 207, pp. 574–579. DOI: [10.1016/j.proeng.2017.10.1023](https://doi.org/10.1016/j.proeng.2017.10.1023).
- Mohammad A.A., Avik S., Reza A.B., Hongtao D. An efficient coupled Eulerian-Lagrangian finite element model for friction stir processing. *The International Journal of Advanced Manufacturing Technology*, 2019, vol. 101, pp. 1495–1508. DOI: [10.1007/s00170-018-3000-z](https://doi.org/10.1007/s00170-018-3000-z).
- Malik V., Sanjeev N.K., Suresh H.S., Kailas S.V. Investigations on the effect of various tool pin profiles in

- friction stir welding using finite element simulations. *Procedia Engineering*, 2014, vol. 97, pp. 1060–1068. DOI: [10.1016/j.proeng.2014.12.384](https://doi.org/10.1016/j.proeng.2014.12.384).
15. Ranjole C., Singh V.P., Kuriachen B., Vineesh K.P. Numerical prediction and experimental investigation of temperature, residual stress and mechanical properties of dissimilar friction-stir welded AA5083 and AZ31 alloys. *Arabian Journal for Science and Engineering*, 2022, vol. 47, pp. 16103–16115. DOI: [10.1007/s13369-022-06808-3](https://doi.org/10.1007/s13369-022-06808-3).
  16. Garcia-Castillo F.A., Reyes L.A., Garza C., Lopez-Botello O.E., Hernandez-Munoz G.M., Zambrano-Robledo P. Investigation of microstructure, mechanical properties, and numerical modeling of Ti6Al4V joints produced by friction stir spot welding. *Journal of Materials Engineering and Performance*, 2020, vol. 29, no. 6, pp. 4105–4116. DOI: [10.1007/s11665-020-04900-z](https://doi.org/10.1007/s11665-020-04900-z).
  17. Salloomi K.N. Fully coupled thermomechanical simulation of friction stir welding of aluminum 6061-T6 alloy T-joint. *Journal of Manufacturing Processes*, 2019, vol. 45, pp. 746–754. DOI: [10.1016/j.jmapro.2019.06.030](https://doi.org/10.1016/j.jmapro.2019.06.030).
  18. Kamal M., Shah M., Ahmad N., Wani O.I., Sahari J. Study of crashworthiness behavior of thin-walled tube under axial loading by using computational mechanics. *International Journal of Materials and Metallurgical Engineering*, 2016, vol. 10, no. 8, pp. 1170–1175. DOI: [10.5281/zenodo.1130389](https://doi.org/10.5281/zenodo.1130389).
  19. Chao Y.J., Liu S., Chien C.H. Friction stir welding of AL 6061-T6 thick plates: Part II. Numerical modeling of the thermal and heat transfer phenomena. *Journal of the Chinese Institute of Engineers*, 2008, vol. 31, no. 5, pp. 769–779. DOI: [10.1080/02533839.2008.9671431](https://doi.org/10.1080/02533839.2008.9671431).
  20. Wang C., Deng J., Dong C., Zhao Y. Numerical simulation and experimental studies on stationary shoulder friction stir welding of aluminum alloy t-joint. *Frontiers in Materials*, 2022, vol. 9, pp. 1–8. DOI: [10.3389/fmats.2022.898929](https://doi.org/10.3389/fmats.2022.898929).
  6. Chauhan P., Jain R., Pal S.K., Singh S.B. Modeling of defects in friction stir welding using coupled Eulerian and Lagrangian method // *Journal of Manufacturing Processes*. 2018. Vol. 34-A. P. 158–166. DOI: [10.1016/j.jmapro.2018.05.022](https://doi.org/10.1016/j.jmapro.2018.05.022).
  7. Meyghani B., Awang M.B., Emamian S.S., Mohd Nor M.K.B., Pedapati S.R. A Comparison of Different Finite Element Methods in the Thermal Analysis of Friction Stir Welding (FSW) // *Metals*. 2017. Vol. 7. № 10. Article number 450. DOI: [10.3390/met7100450](https://doi.org/10.3390/met7100450).
  8. Andrade D.G., Leitão C., Dialami N., Chiumenti M., Rodrigues D.M. Modelling torque and temperature in friction stir welding of aluminium alloys // *International Journal of Mechanical Sciences*. 2020. Vol. 182. Article number 105725. DOI: [10.1016/j.ijmecsci.2020.105725](https://doi.org/10.1016/j.ijmecsci.2020.105725).
  9. El-Sayed M.M., Shash A.Y., Mahmoud T.S., Rabbou M.A. Effect of friction stir welding parameters on the peak temperature and the mechanical properties of aluminum alloy 5083-O // *Advanced Structured Materials*. 2018. Vol. 72. P. 11–25. DOI: [10.1007/978-3-319-59590-0\\_2](https://doi.org/10.1007/978-3-319-59590-0_2).
  10. El-Sayed M.M., Shash A.Y., Abd-Rabou M. Finite element modeling of aluminum alloy AA5083-O friction stir welding process // *Journal of Materials Processing Technology*. 2018. Vol. 252. P. 13–24. DOI: [10.1016/j.jmatprotec.2017.09.008](https://doi.org/10.1016/j.jmatprotec.2017.09.008).
  11. Patil S., Tay Y.Y., Baratzadeh F., Lankarani H. Modeling of friction-stir butt-welds and its application in automotive bumper impact performance. Part 1. Thermo-mechanical weld process modeling // *Journal of Mechanical Science and Technology*. 2018. Vol. 32. № 6. P. 2569–2575. DOI: [10.1007/s12206-018-0514-0](https://doi.org/10.1007/s12206-018-0514-0).
  12. Lia K., Jarrara F., Sheikh-Ahmada J., Ozturkb F. Using coupled Eulerian Lagrangian formulation for accurate modeling of the friction stir welding process // *Procedia Engineering*. 2017. Vol. 207. P. 574–579. DOI: [10.1016/j.proeng.2017.10.1023](https://doi.org/10.1016/j.proeng.2017.10.1023).
  13. Mohammad A.A., Avik S., Reza A.B., Hongtao D. An efficient coupled Eulerian-Lagrangian finite element model for friction stir processing // *The International Journal of Advanced Manufacturing Technology*. 2019. Vol. 101. P. 1495–1508. DOI: [10.1007/s00170-018-3000-z](https://doi.org/10.1007/s00170-018-3000-z).
  14. Malik V., Sanjeev N.K., Suresh H.S., Kailas S.V. Investigations on the effect of various tool pin profiles in friction stir welding using finite element simulations // *Procedia Engineering*. 2014. Vol. 97. P. 1060–1068. DOI: [10.1016/j.proeng.2014.12.384](https://doi.org/10.1016/j.proeng.2014.12.384).
  15. Ranjole C., Singh V.P., Kuriachen B., Vineesh K.P. Numerical prediction and experimental investigation of temperature, residual stress and mechanical properties of dissimilar friction-stir welded AA5083 and AZ31 alloys // *Arabian Journal for Science and Engineering*. 2022. Vol. 47. P. 16103–16115. DOI: [10.1007/s13369-022-06808-3](https://doi.org/10.1007/s13369-022-06808-3).
  16. Garcia-Castillo F.A., Reyes L.A., Garza C., Lopez-Botello O.E., Hernandez-Munoz G.M., Zambrano-Robledo P. Investigation of microstructure, mechanical properties, and numerical modeling of Ti6Al4V joints produced by friction stir spot welding // *Journal of Materials Engineering and Performance*. 2020. Vol. 29. № 6. P. 4105–4116. DOI: [10.1007/s11665-020-04900-z](https://doi.org/10.1007/s11665-020-04900-z).
  17. Salloomi K.N. Fully coupled thermomechanical simulation of friction stir welding of aluminum 6061-T6 alloy

## СПИСОК ЛИТЕРАТУРЫ

1. Ищенко А.Я., Подъельников С.В., Покляцкий А.Г. Сварка трением с перемешиванием алюминиевых сплавов (обзор) // *Автоматическая сварка*. 2007. № 11. С. 32–38.
2. Arbegast W.J. Friction stir welding after a decade of development // *Welding Journal*. 2006. Vol. 85. № 3. P. 28–35.
3. Okamura H., Aota K., Ezumi M. Friction stir welding of aluminum alloy and application to structure // *Journal of Japan Institute of Light Metals*. 2000. Vol. 50. № 4. P. 166–172. DOI: [10.2464/jilm.50.166](https://doi.org/10.2464/jilm.50.166).
4. Salloomi K.N., Hussein F.I., Al-Sumaidae S.N.M. Temperature and stress evaluation during three different phases of friction stir welding of AA 7075-T651 alloy // *Modelling and Simulation in Engineering*. 2020. Vol. 2020. P. 1–11. DOI: [10.1155/2020/3197813](https://doi.org/10.1155/2020/3197813).
5. Ragab M., Liu H., Yang G.-J., Ahmed M.M.Z. Friction stir welding of 1Cr11Ni2W2MoV martensitic stainless steel: Numerical simulation based on coupled Eulerian Lagrangian approach supported with experimental work // *Applied Science*. 2021. Vol. 11. № 7. P. 1–6. DOI: [10.3390/app11073049](https://doi.org/10.3390/app11073049).

- T-joint // Journal of Manufacturing Processes. 2019. Vol. 45. P. 746–754. DOI: [10.1016/j.jmapro.2019.06.030](https://doi.org/10.1016/j.jmapro.2019.06.030).
18. Kamal M., Shah M., Ahmad N., Wani O.I., Sahari J. Study of crashworthiness behavior of thin-walled tube under axial loading by using computational mechanics // International Journal of Materials and Metallurgical Engineering. 2016. Vol. 10. № 8. P. 1170–1175. DOI: [10.5281/zenodo.1130389](https://doi.org/10.5281/zenodo.1130389).
19. Chao Y.J., Liu S., Chien C.H. Friction stir welding of AL 6061-T6 thick plates: Part II. Numerical modeling of the thermal and heat transfer phenomena // Journal of the Chinese Institute of Engineers. 2008. Vol. 31. № 5. P. 769–779. DOI: [10.1080/02533839.2008.9671431](https://doi.org/10.1080/02533839.2008.9671431).
20. Wang C., Deng J., Dong C., Zhao Y. Numerical simulation and experimental studies on stationary shoulder friction stir welding of aluminum alloy t-joint // Frontiers in Materials. 2022. Vol. 9. P. 1–8. DOI: [10.3389/fmats.2022.898929](https://doi.org/10.3389/fmats.2022.898929).

## Численное моделирование температурных полей

### при сварке трением с перемешиванием алюминиевого сплава AA5083

© 2023

**Зыбин Игорь Николаевич**<sup>\*1</sup>, кандидат технических наук, доцент,  
доцент кафедры «Технологии соединения и обработки материалов»

**Антохин Михаил Сергеевич**<sup>2</sup>, магистрант кафедры «Технологии соединения и обработки материалов»  
Калужский филиал Московского государственного технического университета имени Н.Э. Баумана,  
Калуга (Россия)

\*E-mail: [igor.zybin@mail.ru](mailto:igor.zybin@mail.ru)

<sup>1</sup>ORCID: <https://orcid.org/0000-0002-5738-4231>

<sup>2</sup>ORCID: <https://orcid.org/0000-0002-8043-1606>

Поступила в редакцию 12.12.2022

Принята к публикации 30.01.2023

**Аннотация:** Одним из важных параметров, обеспечивающих получение сварного соединения при сварке трением с перемешиванием без дефектов сплошности, является обеспечение в зоне соединения металлов требуемой температуры. При экспериментальном определении температуры непосредственно в зоне перемешивания металлов с помощью термопар возникают значительные трудности. В связи с этим актуальным представляется использование численных методов, описывающих распределение температурных полей при сварке трением с перемешиванием. В работе выполнено численное моделирование температурных полей при сварке трением с перемешиванием на основе метода конечных элементов с использованием программного обеспечения Abaqus/Explicit. Моделирование выполнялось на основе связанного подхода Эйлера – Лагранжа, модели пластичности материала Джонсона – Кука и закона трения Кулона. С помощью метода конечных элементов построены модели детали, подложки и инструмента с учетом их теплофизических свойств. Для сокращения времени вычислений использовался подход масштабирования массы путем пересчета плотности материала и его тепловых свойств. Были подобраны коэффициенты масштабирования теплоемкости и массы материала для выбранных параметров режима сварки. Для оценки адекватности результатов численного моделирования температурных полей при сварке трением с перемешиванием были проведены экспериментальные исследования температурных полей с использованием термопар. Показана возможность численного моделирования температурных полей при сварке трением с перемешиванием с помощью связанного подхода Эйлера – Лагранжа и программного обеспечения Abaqus/Explicit. Благодаря применению подхода, связанного с масштабированием массы материала, время вычислений сокращено более чем в 10 раз.

**Ключевые слова:** сварка трением с перемешиванием; AA5083; связанный подход Эйлера – Лагранжа; численное моделирование температурных полей.

**Для цитирования:** Зыбин И.Н., Антохин М.С. Численное моделирование температурных полей при сварке трением с перемешиванием алюминиевого сплава AA5083 // Frontier Materials & Technologies. 2023. № 1. С. 23–32. DOI: [10.18323/2782-4039-2023-1-23-32](https://doi.org/10.18323/2782-4039-2023-1-23-32).

## Characteristic properties of the microstructure and microtexture of medium-carbon steel subjected to sulfide stress cracking

© 2023

*Andrey V. Malinin*<sup>1,3</sup>, PhD (Engineering),  
Deputy Director  
*Vil D. Sitdikov*<sup>1,4</sup>, Doctor of Sciences (Physics and Mathematics),  
Head of the laboratory  
*Valeria E. Tkacheva*<sup>1,5</sup>, PhD (Engineering), Associate Professor, Chief Specialist  
*Artem K. Makatrov*<sup>1,6</sup>, PhD (Engineering),  
Head of the Department  
*Ilya V. Valekzhanin*<sup>1,7</sup>, Head of the Department  
*Andrey N. Markin*<sup>2</sup>, PhD (Engineering),  
assistant professor of Chair “Oil and Gas Engineering”

<sup>1</sup>LLC “RN-BashNIPIneft”, Ufa (Russia)<sup>2</sup>Branch of Industrial University of Tyumen in Nizhneartovsk, Nizhneartovsk (Russia)

\*E-mail: MalininAV@bnipi.rosneft.ru

<sup>3</sup>ORCID: <https://orcid.org/0000-0003-1185-5648><sup>4</sup>ORCID: <https://orcid.org/0000-0002-9948-1099><sup>5</sup>ORCID: <https://orcid.org/0000-0001-6927-9781><sup>6</sup>ORCID: <https://orcid.org/0000-0002-2822-9072><sup>7</sup>ORCID: <https://orcid.org/0000-0001-9472-2968>

Received 06.12.2022

Accepted 06.03.2023

**Abstract:** Increasing the resistance of steel products to sulfide stress cracking (SSC) is one of the topical issues of the oil and gas industry. Among various factors determining the SSC resistance of a material is the structure-phase state of the material itself and the crystallographic texture associated with it. The current paper analyzes these features using the scanning electron microscopy (SEM), transmission electron microscopy (TEM), and microroentgen electron backscattered diffraction (EBSD) techniques. As the research material, a production string (PS) coupling made of medium-carbon steel was selected, which collapsed by the mechanism of hydrogen embrittlement and subsequent SSC. For the first time, by the SEM method, using the location and mutual orientation of cementite (Fe<sub>3</sub>C) particles, at high magnifications, the authors demonstrated the possibilities of identifying the components of upper bainite, lower bainite, and tempered martensite in steels. The presence of the detected structural components of steel was confirmed by transmission electron microscopy (TEM). Using the EBSD method, the detailed studies of microtexture were conducted to identify the type and nature of the microcrack propagation. It is established that the processes of hydrogen embrittlement and subsequent SSC lead to the formation of {101} <0 $\bar{1}$ 0>, {100} <001>, {122} <2 $\bar{1}$ 0>, {013} <211>, {111} < $\bar{1}$ 00>, {133} < $\bar{1}$ 2 $\bar{1}$ >, {3 $\bar{2}$ 6} <201> grain orientations. It is shown that the strengthening of orientations of {001} <110>, {100} <001>, {112} <111>, and {133} < $\bar{1}$ 2 $\bar{1}$ > types worsens the SSC resistance of the material. Using the EBSD analysis method, the influence of special grain boundaries on the nature of microcrack propagation is estimated. It is found that the  $\Sigma$  3 coincident site lattice grain boundaries between the {122} <2 $\bar{1}$ 0> and {111} < $\bar{1}$ 00>, {012} < $\bar{1}$ 10>, {100} <001> plates of the upper bainite inhibit the microcrack development, and the  $\Sigma$  13b,  $\Sigma$  29a, and  $\Sigma$  39a boundaries, on the contrary, contribute to the accelerated propagation of microcracks. For comparative analysis, similar studies were carried out in an unbroken (original) coupling before operation.

**Keywords:** medium-carbon steel; bainite microstructure; sulfide stress cracking; crystallographic texture.

**For citation:** Malinin A.V., Sitdikov V.D., Tkacheva V.E., Makatrov A.K., Valekzhanin I.V., Markin A.N. Characteristic properties of the microstructure and microtexture of medium-carbon steel subjected to sulfide stress cracking. *Frontier Materials & Technologies*, 2023, no. 1, pp. 33–44. DOI: 10.18323/2782-4039-2023-1-33-44.

### INTRODUCTION

The complex of oil and gas pipes of the Russian Federation is one of the most developed systems, and belongs to the key type of raw oil and gas transportation throughout the RF territory. In this regard, the highest requirements are imposed on oil and gas pipelines, which aim to ensure their reliability, durability, and safety [1–3]. The latter is associated with irreversible environmental, and economic expenditures in the case of an unintended breakdown of pipelines and their units in a certain sector of oil transportation. Among various types of complications in oil production,

the mechanical corrosion failure – sulfide stress cracking is the most serious [4–6]. Sulfide stress cracking (SSC) of oilfield equipment is determined by the action of various factors, among which are the partial pressure of hydrogen sulfide and the temperature in the string, the degree of salinity of the water component of oil, and the stress-strain state of the metal. These factors are best described in the GOST 53678 standard and in the works [6–8]. Besides the abovementioned factors, the SSC-resistance of steels is determined by the degree of alloying of iron with impurity atoms, the structure-phase state, the level and anisotropy of strength properties, which determine

the final mechanical properties of materials. A developed crystallographic texture, which can be controlled by optimizing the modes of thermomechanical effect, is a particularly important parameter in the operation of goods [5; 9].

It is known that the boundaries of grains, laths, and plates formed during quenching and subsequent tempering, are the preferred areas for precipitation of cementite particles [10]. As a result of external applied loads, due to the difference in microhardness, microcracks appear between the cementite particles and the main matrix. Subsequently, they propagate along the prior austenite grain boundaries (PAGB) or along the lath martensite boundaries [10]. According to [11], martensitic steel characterized by a relatively low ductility is more prone to SSC compared to tempered martensite. At the same time, the presence of some alloying elements (for example, Nb, V, Mo, and Ti) during aging generates the precipitate at the grain boundaries, which reduce the SSC susceptibility of steel [11]. The shape and size of the constituent elements of the steel microstructure also determine the material propensity to SSC. In particular, the authors [12] identified that the ferrite-pearlite structure is more prone to SSC than the acicular ferrite or ultrafine-grained bainitic structure. In this regard, it was concluded that a homogeneous and uniform structure has a greater SSC resistance [12].

Some works deal with the study of the nature of the microcrack propagation in steels, as well as identifying the relationship between this nature and the crystallographic texture, the type of grain boundaries and their orientation relative to each other [13–15]. In particular, in the work [13], the authors showed that the formation of low-angle and coincident site lattice (CSL) grain boundaries increases the cracking resistance of the API X65 steel. Moreover, it was found that the presence of CSL grain boundaries smaller than  $\Sigma$  13b provides cracking resistance [13], while a number of other high-angle boundaries (not CSL), worsen the SSC resistance [14; 15]. As a result, forming the low-angle and CSL grain boundaries of a certain type, it is possible to stop a microcrack after its formation and obtain crack-resistant steel.

Thus, the above factors, which are responsible for the microcrack initiation and development, are controlled, and on the whole, determine the tendency of the material to SSC. The control of these factors, by changing the processing parameters, as well as the formation of

certain microstructures and crystallographic textures with the required strength characteristics for specific types of operation of oilfield equipment, is a crucial task.

This work is aimed to identify the structure-phase features and regularities of the texture formation processes, in a standard production string coupling made of bainitic steel structure, as well as to establish the factors determining its resistance to hydrogen sulfide stress cracking.

## METHODS

A production string (PS) coupling with an outer diameter of 139.7 mm and a wall thickness of 9.17 mm, manufactured according to the GOST 31446 standard (strength group P110), was selected as the research material. The chemical composition of the investigated coupling is shown in Table 1.

The studies were carried out in two PS couplings. The first one was destroyed by the SSC mechanism during the hydraulic fracture of a shelf on an exploration well. The second coupling was new, without operation. A bainite structure was formed in the couplings at the factory conveyor conditions, by carrying out the traditional heat treatment (quenching and subsequent tempering). The mechanical tensile tests were carried out using an INSPEKT 200 universal testing machine according to the GOST 10006 requirements. Microhardness was measured by the Rockwell method using a 251 VRSD universal hardness tester. The SP coupling microstructure was studied using a Thermo Scientific Q250 scanning electron microscope equipped with the EDAX-TSL system for backscattered electron diffraction (EBSD) analysis. The imaging of samples was carried out at an accelerating voltage of 20 kV at a chamber pressure of  $10^{-4}$  Pa. The electron beam diameter was 3  $\mu\text{m}$ . During the study, the sample was placed at a focal distance of 10.0 mm. Nital solution was used as a metallographic reagent. The microstructure was also analyzed using a transmission electron microscope (TEM), to get the information about the size of structural elements and the nature of the arrangement of cementite precipitates. The observations were carried out on a JEM-2100 microscope at an accelerating voltage of 200 kV. The samples for TEM were prepared by two-jet electropolishing using an electrolyte based on n-butyl alcohol.

*Table 1. Chemical composition of the coupling material  
Таблица 1. Химический состав материала муфты*

Content, wt. %									
Fe	C	Si	Mn	P	S	Cr	Ni	Mo	Al
97.1	0.452	0.306	1.400	0.014	0.005	0.278	0.199	0.006	0.012
Content, wt. %									
Co	Cu	V	Ti	Sn	B	Zr	As	Bi	
<0.001	0.026	0.058	0.002	0.011	0.002	0.002	0.075	0.010	

## RESULTS

The average value of the coupling metal microhardness in the primary crack nucleus is 35.5 HRC, and far from the crack, its value decreases to 34.0 HRC. At the same time, the average hardness of the pipe billet metal without operation was 32.6 HRC. The mechanical tests showed that in the coupling before operation, the tensile strength was 983 MPa, the yield strength was 913 MPa, and the relative elongation was 15.5 %; while after operation, the tensile strength was 1096 MPa, the yield strength was 1000 MPa, and the relative elongation was 13.7 %.

Fig. 1 a shows a typical SEM image of the PS coupling microstructure (before operation) after etching. The experimental microstructure is mainly characterized by a bainitic structure consisting of parallel plates. In the photograph, the bainite plates are shown as disoriented blocks inside the PAGB (Fig. 1 a). The bainitic blocks in Fig. 1 a in some places are circled by green contour lines, and PAGB – by yellow lines. Along with the bainite component, the microstructure contains the irregularly shaped islands of the martensitic-austenitic (M/A) phase (Fig. 1 a). Unlike the bainite component, the M/A areas are resistant to etching; they look like non-etched and relatively light areas (outlined with a white line) (Fig. 1 a). A microstructure detailed analysis at rather high magnifications showed that the bainite component is formed from the upper bainite (UB) and lower bainite (LB) plates. This fact is supported by the results of SEM and TEM studies, according to which the needle-like cementite ( $\text{Fe}_3\text{C}$ ) particles in the UB plates are located only at the plate boundaries and are oriented along the boundaries (Fig. 1 b) [10]. The detected cementite particles at the boundaries of the UB plates in some places grow up to a length of 170 nm, while their diameter equal to ~34 nm remains practically unchanged. At the same time, in the LB, cementite particles are formed only in the body of the plates (Fig. 1 c, 1 d). In this case, the cementite particles in the LB have a needle-like shape (up to 210 nm long, 22 nm in diameter) and are parallel to each other (Fig. 1 c, 1 d). Fig. 1 d shows the section of the “coalesced” LB, where the merge of parallel plates is observed. In the PS coupling microstructure, rather large plates of tempered martensite (TM) are observed in some places (Fig. 1 e, 1 f). Similar structural components (LB, UB, and TM) in steels were previously observed in the works [17–19]. The TM plates (laths) have a length of up to several tens of microns and a width of 1–4 microns. The difference between the TM and the UB and LB is that, in the TM plates, cementite particles of the needle-like morphology are oriented between themselves both parallel and at an angle of  $60^\circ$  with respect to each other (Fig. 1 e, 1 f) [19].

Fig. 2 a shows a typical SEM image of the PS coupling microstructure after operation. The precision SEM analysis showed (Fig. 2 a, 2 b) that the microstructure of the PS coupling after operation contains similar structural components (UB, LB, TM, and M/A), which were found in the original coupling (Fig. 2 a–f). At the same time, during the transition to the area where the destruction occurred according to the SSC mechanism, significant changes in the microstructure are identified (Fig. 2 c–f).

In particular, in the area very close to a fracture, the microstructure is characterized by the absence of visible needle-like cementite particles in the plates (laths) (Fig. 2 c).

The absence of cementite particles both inside the plates and between them indicates the formation of a purely martensitic structure with a body-centered tetragonal (BCT) lattice [20]. The external applied load in the fracture zone leads both to the rotation of the plate-like structure in the direction of tensile forces and the formation of deformation bands (Fig. 2 d) and to the appearance of cracks on the non-metallic inclusions (Fig. 2 d, upper right corner, Fig. 2 e, upper left corner). Fig. 2 e, 2 f show a general view of the path of the secondary crack propagation as a result of SSC. It is obvious that at the initial stages, the crack propagates according to the transcrystalline type (up to 60  $\mu\text{m}$ ), and then it has an intercrystalline type (Fig. 2 e, 2 f). In this case, it is seen that, when stopped, a crack can be initiated at the boundary of the plates (Fig. 2 f). The analysis of SEM images showed that in all the studied areas, the PS coupling contamination with non-metallic inclusions did not exceed 5 points (SH method).

To analyze the nature of microcrack propagation, the authors studied the local crystallographic microtexture, i. e., the predominant grain orientations, as shown in Fig. 3 a. The analysis of the distribution map of grain orientations was carried out in the plane of the sample cross section. For ease of analysis, individual orientations of each block and plates are shown in different colors (Fig. 3 a, 3 b).

According to the EBSD analysis, the average size of the PAGB blocks in the PS coupling before operation was ~80  $\mu\text{m}$ , and after failure in the fracture region, it was ~66  $\mu\text{m}$ . The EBSD analysis showed that, in the coupling failure area, a crystallographic texture is basically formed, in which grain orientations related to the  $\{101\} \langle 010 \rangle$ ,  $\{100\} \langle 001 \rangle$ , and  $\{111\} \langle \bar{1}00 \rangle$  texture components dominate (Fig. 3 a). At the same time, in the coupling without operation, the  $\{110\} \langle 001 \rangle$ ,  $\{001\} \langle 110 \rangle$ , and  $\{111\} \langle 011 \rangle$  grain orientations are prevailing. The main texture components identified in the PS coupling before and after operation (with a crack) are recorded in Table 2.

Besides, Table 2 shows schematically the orientations of individual plates with respect to the ND–TD plane and their volume fractions belonging to one or another texture component. To identify the influence of the texture formation processes on the nature of crack propagation, local EBSD studies were carried out (Fig. 3 b). In this case, the authors paid special attention to the identification of high-angle disorientations related to CSL grain boundaries formed both in the original coupling and in the coupling after operation (Fig. 4 a, 4 b). The distributions of CSL grain boundaries corresponding to the original and destroyed coupling (crack area) are shown in Fig. 4 a, 4 b, and their volume fractions are summarized in Table 3.

To determine the influence of mutual orientations of plates (laths) on the crack propagation character, the authors carried out an analysis of microtexture research. Fig. 5 shows the direct pole figures (PF) (110) of the PS coupling obtained from different areas of analysis: without operation, away from the fracture, and in the crack surrounding area.

The pole figure (110) obtained for the PS coupling before operation, according to microtexture analysis, is characterized by a set of the following main orientations:  $\{101\} \langle 0\bar{1}0 \rangle$ ,  $\{100\} \langle 001 \rangle$ ,  $\{122\} \langle 2\bar{1}0 \rangle$ ,  $\{013\} \langle 211 \rangle$ ,  $\{111\} \langle \bar{1}00 \rangle$ ,  $\{133\} \langle \bar{1}\bar{2}1 \rangle$ ,  $\{3\bar{2}\bar{6}\} \langle 201 \rangle$ ,  $\{102\} \langle 2\bar{1}1 \rangle$ ,  $\{230\} \langle 3\bar{2}3 \rangle$ ,  $\{122\} \langle 2\bar{2}1 \rangle$ ,  $\{110\} \langle \bar{1}\bar{1}1 \rangle$ , and  $\{111\} \langle \bar{1}00 \rangle$

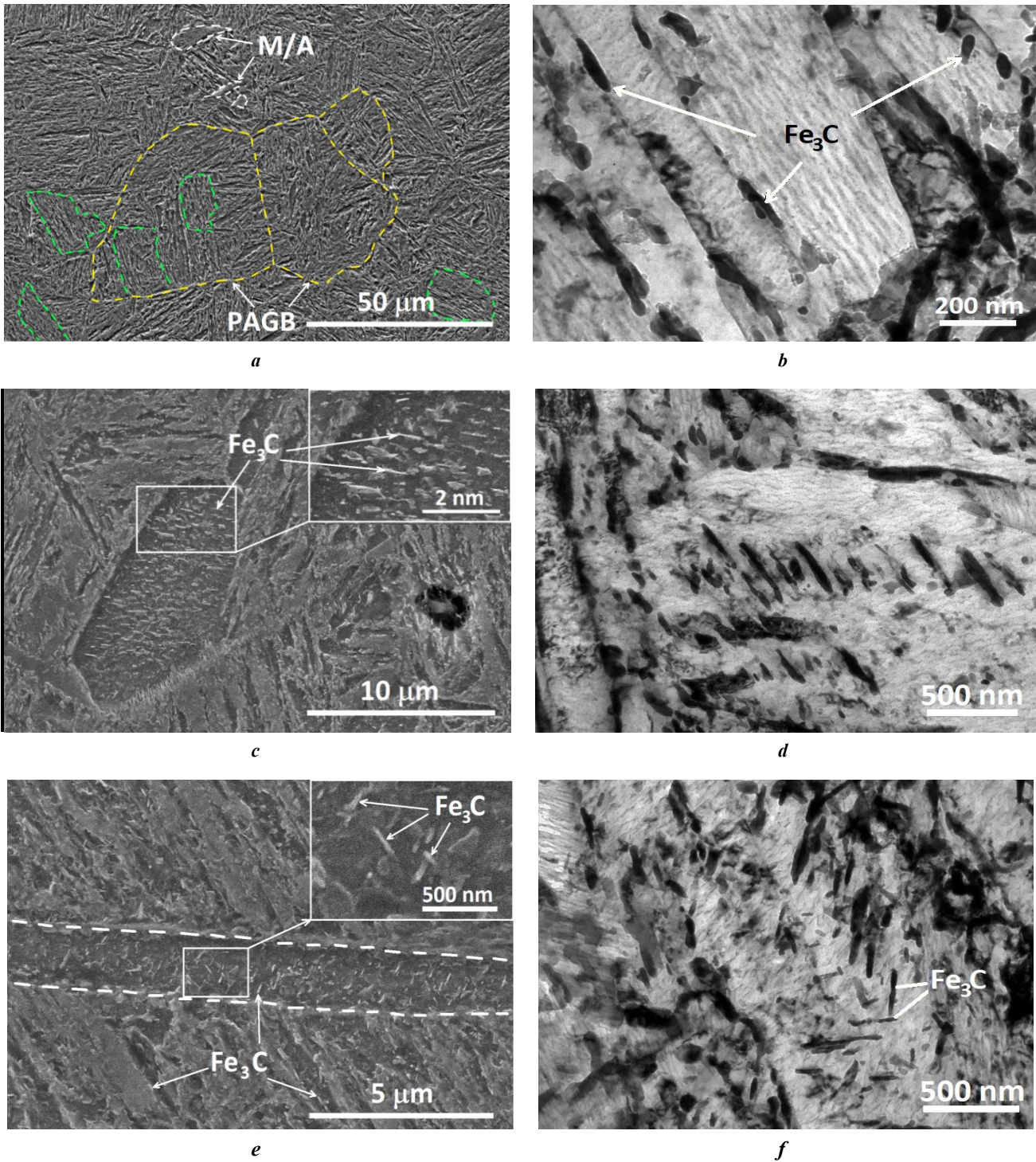
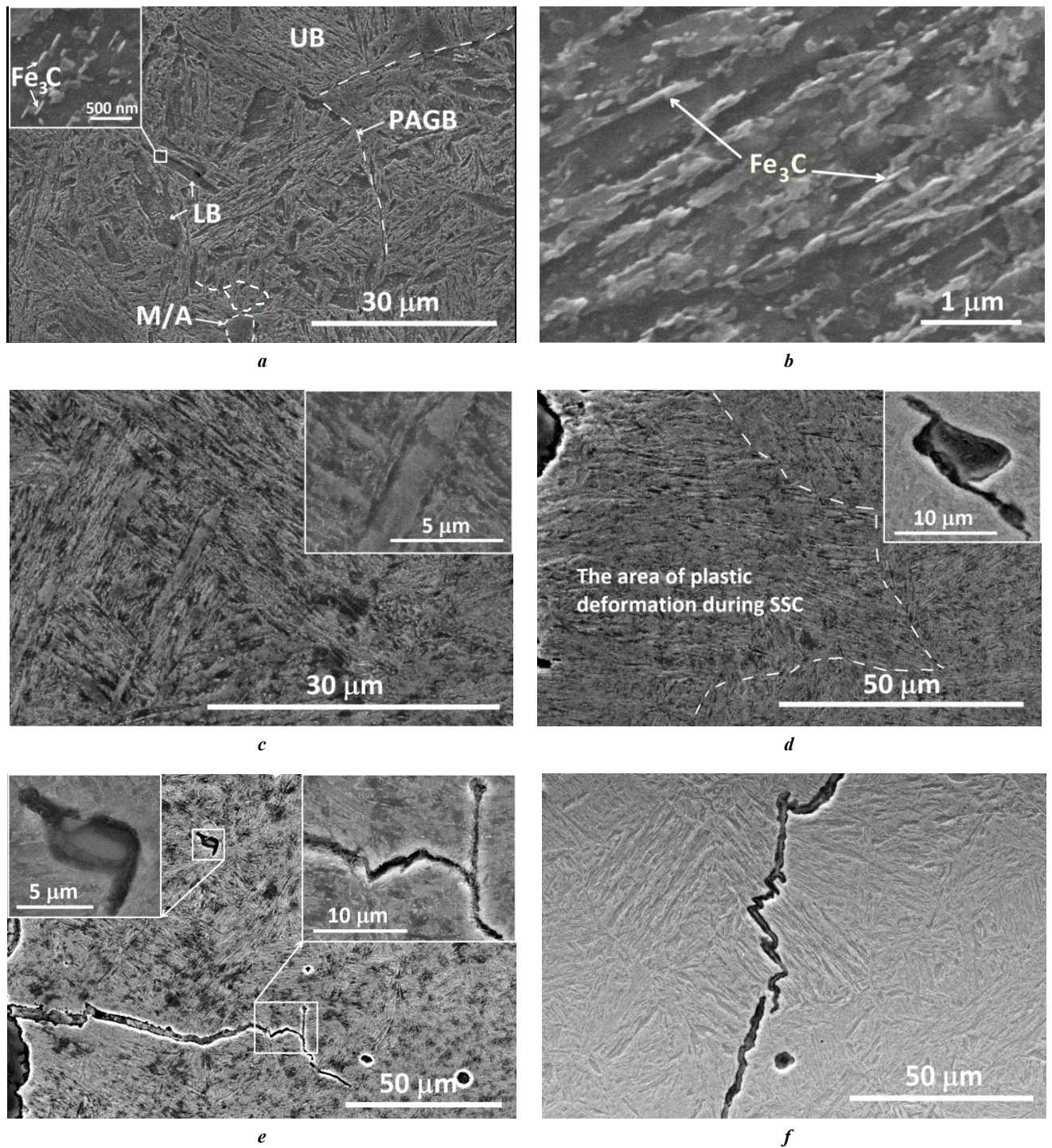


**Fig. 1.** Images of the PS coupling microstructure (before operation):

*a* – microstructure general view; *b* – upper bainite plates;  
*c, d* – lower bainite plates; *e, f* – martensite tempering plates.  
*M/A* – martensite-austenite areas; *PAGB* – prior austenite grain boundaries.  
*a, c, e* – SEM images; *b, d, f* – TEM images

**Рис. 1.** Изображения микроструктуры муфты ЭК (до эксплуатации):

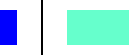
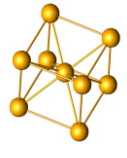
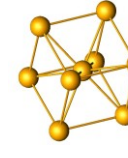
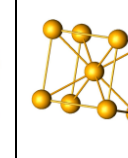
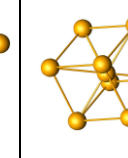
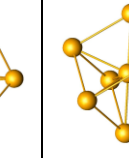
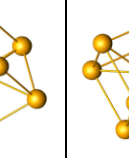
*a* – общий вид микроструктуры; *b* – пластины верхнего бейнита;  
*c, d* – пластины нижнего бейнита; *e, f* – мартенситные пластины отпуска.  
*M/A* – мартенситно-аустенитные участки; *PAGB* – первоначальные границы зерен аустенита.  
*a, c, e* – РЭМ-изображения; *b, d, f* – ПЭМ-изображения



**Fig. 2.** Microstructure SEM images:  
*a* – general view of the microstructure away from the fracture area; *b* – upper bainite plates;  
*c* – general view of the microstructure in the fracture area; *d* – deformation bands;  
*e* – the appearance of cracks in the fracture area; *f* – crack development on bainitic blocks.  
 UB – upper bainite; LB – lower bainite

**Рис. 2.** РЭМ-изображения микроструктуры после эксплуатации:  
*a* – общий вид микроструктуры вдали от излома; *b* – пластины верхнего бейнита;  
*c* – общий вид микроструктуры в области излома; *d* – полосы деформации;  
*e* – вид трещин в области излома; *f* – развитие трещины на бейнитных блоках.  
 UB – верхний бейнит; LB – нижний бейнит

**Table 2.** The determined orientations of bainite/martensite plates and their volume fraction  
**Таблица 2.** Обнаруженные ориентации бейнитных/мартенситных пластин и их объемная доля

Plane of Analysis ND ↑ TD →	The main orientations and their volume fraction, %						
							
							
Euler angles, $\varphi_1, \Phi, \varphi_2$	181.8, 35.1, 76.7	88.2, 5.9, 73.7	230.2, 46.5, 66.4	259.6, 13.5, 0	333.9, 49.1, 49.8	17.6, 44.5, 17.9	331.3, 33.4, 55.5
Orientation	{101} <0 $\bar{1}$ 0>	{100} <001>	{122} <2 $\bar{1}$ 0>	{013} <211>	{111} < $\bar{1}$ 00>	{133} < $\bar{1}$ 21>	{32 $\bar{6}$ } <201>
Before operation	4.6	3.3	4.1	6.5	6.5	7.8	8.9
After operation	8.2	6.9	7.2	8.8	6.0	12.3	5.7
Crack area	9.9	13.7	9.1	12.1	8.6	10.2	4.6

Note. ND – normal direction oriented along the coupling (pipe) radius;  
 TD – transverse direction coinciding with the coupling (pipe) axis.  
 Примечание. ND – нормальное направление, ориентированное вдоль радиуса муфты (трубы);  
 TD – поперечное направление, совпадающее с осью муфты (трубы).

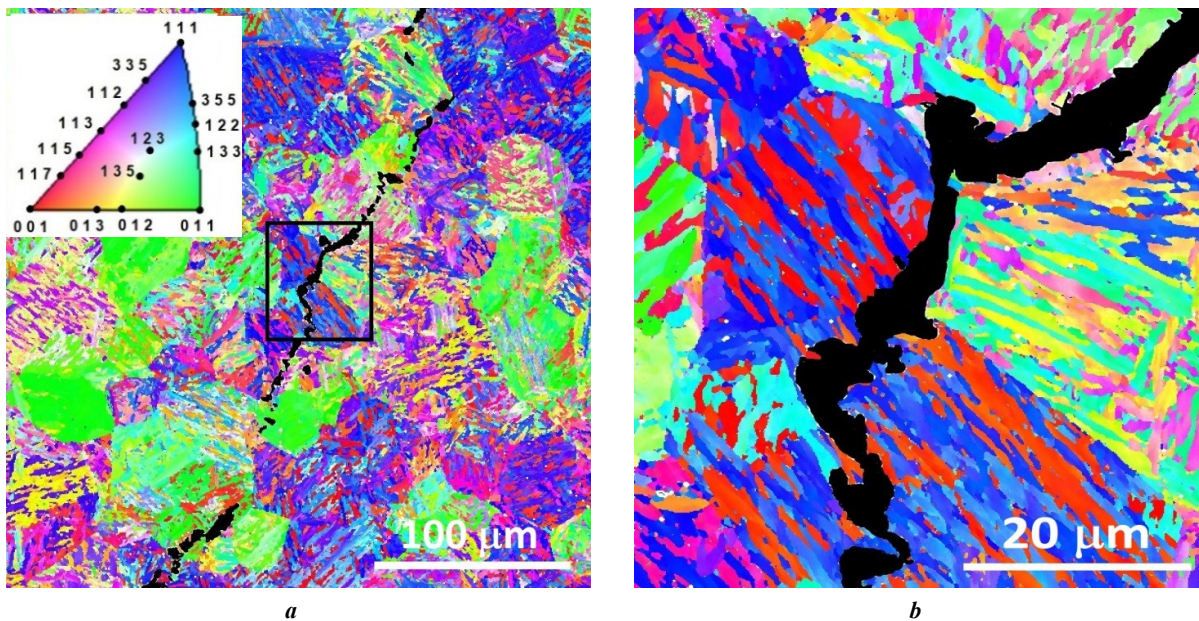


**Fig. 3.** EBSD images of the microstructure: **a** – general view; **b** – precision area  
**Рис. 3.** ДОРЭ-изображения микроструктуры: **a** – общий вид; **b** – прецизионный участок

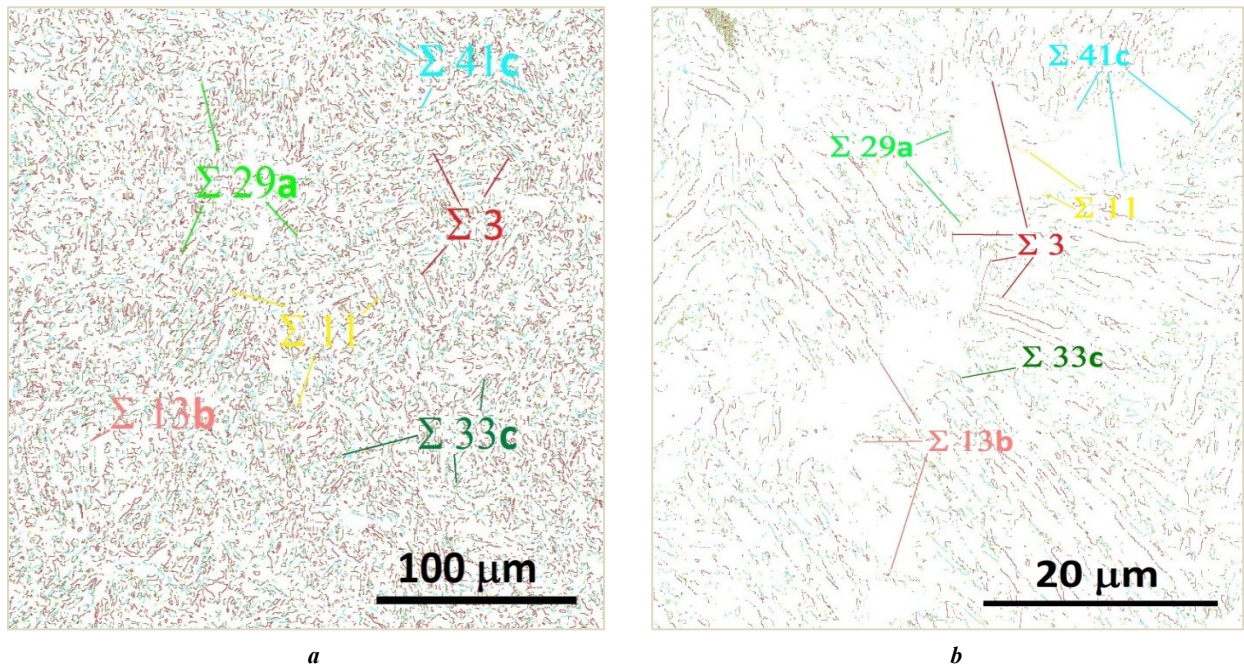


**Fig. 4.** EBSD images of the microstructure:  
*a* – map of distribution of special grain boundaries in the coupling (pipe) without operation;  
*b* – map of distribution of special grain boundaries in the crack area

**Рис. 4.** ДОРЭ-изображения микроструктуры:  
*a* – карта распределения специальных границ зерен в муфте без эксплуатации;  
*b* – карта распределения специальных границ зерен около трещины

**Table 3.** The revealed CSL grain boundaries of bainite plates and their volume fraction  
**Таблица 3.** Выявленные специальные границы  $\Sigma$  бейнитных пластин и их объемная доля

The area of analysis	Volume fraction of CSL grain boundaries, %							
	$\Sigma 3$	$\Sigma 11$	$\Sigma 13b$	$\Sigma 25b$	$\Sigma 29a$	$\Sigma 33c$	$\Sigma 39a$	$\Sigma 41c$
Before operation	12.4	1.1	0.4	1.1	0.3	4.3	0.8	4.2
After operation	11.9	1.4	0.2	1.3	0.1	5.0	0.3	3.8
Crack area	9.6	3.6	4.4	0.4	2.3	2.2	2.6	3.9

(Fig. 5, Table 2). Since the microtexture analysis covers the study of the crack development nature, Fig. 5 d and Table 2 show only the positions of the main grain orientations. The analysis showed that in the PS coupling after operation (away from the crack), the general appearance of the (110) PF remains. However, the ratio of the preferred grain orientations changes. This is evidenced by the redistribution of texture maxima on the (110) PF, where the  $\{102\} \langle 2\bar{1}1 \rangle$ ,  $\{230\} \langle 323 \rangle$ ,  $\{122\} \langle 2\bar{2}1 \rangle$ ,  $\{110\} \langle 1\bar{1}1 \rangle$  and  $\{111\} \langle \bar{1}00 \rangle$ , and  $\{111\} \langle \bar{1}00 \rangle$  orientations are suppressed, while the  $\{101\} \langle 0\bar{1}0 \rangle$ ,  $\{100\} \langle 001 \rangle$ ,  $\{013\} \langle 211 \rangle$ ,  $\{122\} \langle 2\bar{1}0 \rangle$ , and  $\{133\} \langle \bar{1}\bar{2}1 \rangle$  texture components are enhanced (Fig. 5 b, Table 2). This fact is ex-

plained by the fact that during operation, the structure elements rotate as a result of the action of the applied external loads. Moreover, additional orientations (textural maxima) appear on the (110) PF and the pole density of some orientations sharply increases (Fig. 5 b). In particular, as a result of SSC, the weight fractions of the  $\{001\} \langle 110 \rangle$ ,  $\{100\} \langle 001 \rangle$ ,  $\{112\} \langle 111 \rangle$ , and  $\{133\} \langle \bar{1}\bar{2}1 \rangle$  texture components increase (Fig. 5 b).

The precision microtexture analysis showed that the nature of the location of texture maxima on the (110) PF in the crack area changes significantly (Fig. 5 c). In this case, an increase in the pole density of individual orientations is observed (Fig. 5 c). In particular, in the zone

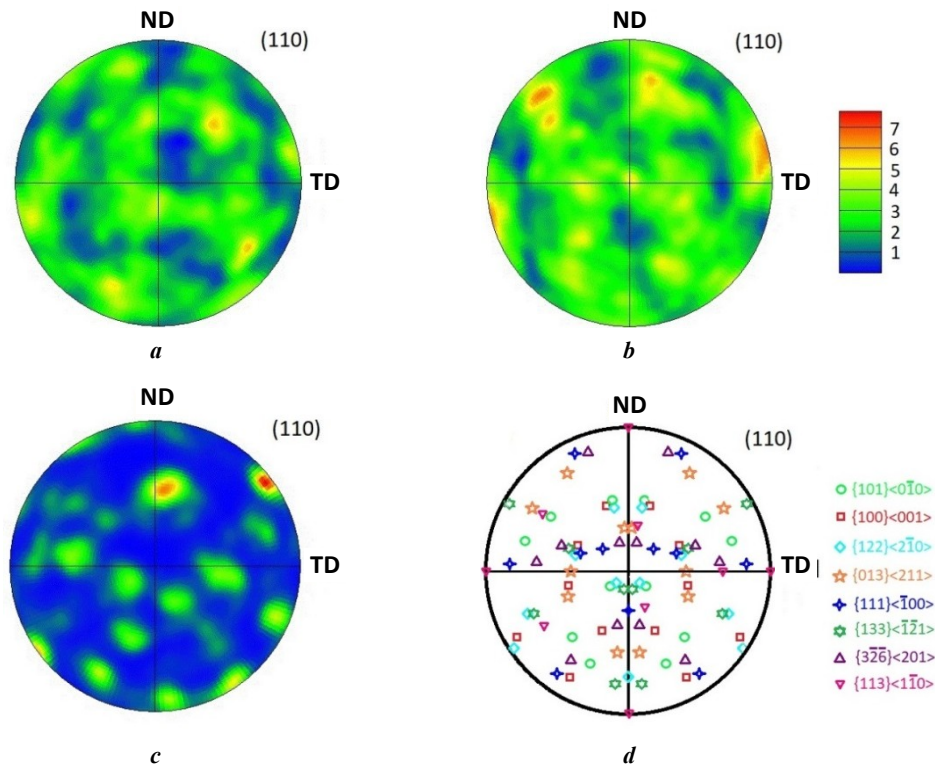


**Fig. 5.** Direct pole figures (110):  
*a* – PS coupling before operation; *b* – after operation away from the crack;  
*c* – in the crack area; *d* – the positions of the determined orientations on a pole figure

**Рис. 5.** Прямые полюсные фигуры (110):  
*a* – муфта ЭК до эксплуатации; *b* – после эксплуатации вдали от трещины;  
*c* – в области трещины; *d* – позиции обнаруженных ориентаций на полюсной фигуре

of crack development, there is a sharp increase in the  $\{101\} \langle 0\bar{1}0 \rangle$ ,  $\{100\} \langle 001 \rangle$ ,  $\{122\} \langle 2\bar{1}0 \rangle$ , and  $\{133\} \langle \bar{1}\bar{2}1 \rangle$  grain orientations, uncharacteristic for the initial PS coupling. In general, the changes in the (110) PF, on the one hand, are associated with the formation of an unfavorable crystallographic texture, and, on the other hand, with the active processes of grinding bainite blocks and subsequent reorientation of the plates as a result of shear deformations.

## DISCUSSION

The analysis of the microstructure of the medium-carbon steel PS coupling showed that various structure components are formed in it: upper bainite, lower bainite, and tempered martensite (Fig. 1). These structural components differ both by the arrangement of cementite particles and their mutual orientation, and by the dimensions of the plates (laths). In particular, the average width of the UB plates is  $0.7 \mu\text{m}$ , and the length is  $\sim 25 \mu\text{m}$ . Cementite particles in the UB plates are located along their boundaries [16–18]. Compared to the UB, the width of the plates in the LB is a bit narrower ( $0.5 \mu\text{m}$ ), and their length does not exceed  $20 \mu\text{m}$ . Needle-like cementite particles in the LB precipitate in the body of the plates and are strictly parallel to each other [16–18]. In the tempered martensite plates, the cementite particles precipitate in the form of needles located in the body of the plates (laths) and are oriented to each other both in parallel and at an angle of  $60^\circ$  with re-

spect to each other [19]. This fact indicates that cementite particles can grow along the  $\langle 011 \rangle$  and  $\langle 110 \rangle$  directions in the BCT lattice. The length of the cementite particle inside the TM plates reaches  $300 \mu\text{m}$ , and the diameter is  $\sim 39 \mu\text{m}$ .

Thus, the UB, LB, and TM distinguishing features are the dimensions of the plates, the precipitation area of cementite particles on the plates, and their mutual orientation. Cementite particles in the UB precipitate only at the boundaries of the plates (laths), in the LB, they precipitate only inside the plates and are parallel to each other, and in the TM plates they are oriented at an angle to each other.

The analysis of the microstructure identified the presence of a structural gradient (UB, LB, TM, M/A, and martensite) in the PS coupling material. In particular, in the area close to the fracture, many martensite plates were found, which, apparently, locally increase the microhardness to 35.5 HRC. Martensite plates in the fracture area are characterized by the absence of cementite particles, the lath width in the range of  $0.6\text{--}3.5 \mu\text{m}$ , and the length of a few tens of  $\mu\text{m}$ . At the same time, areas with a high content of martensite/austenite component of irregular shape were found as well in this area. Numerous secondary microcracks are observed in the fracture area, since the martensitic structure is less SSC-resistant and requires additional tempering [21].

The analysis of the general appearance and path of the secondary crack propagation as a result of SSC indicates that the nature of crack development can be divided into two

stages. At the first stage, it propagates along a rather straight trajectory. It is obvious that the crack thickness, which is approximately equal to 7.5  $\mu\text{m}$  at the crack tip, remains virtually unchanged up to large depths (more than 60  $\mu\text{m}$ ) (Fig. 2 e). This fact indicates that up to the depths of 60  $\mu\text{m}$ , corrosion processes are actively realized with the formation of iron oxides/sulfides. Further, the crack has a more tortuous propagation pattern containing a greater number of deflections (Fig. 2 e, 2 f). At the same time, at the initial stage, the type of crack propagation is transcrystalline (Fig. 2 e). Changes in the microstructure caused by the action of tensile stresses, and the formation of deformation bands shown in Fig. 2 d also led to this type of crack propagation. In this case, the deformation bands were formed as a result of the bainitic structure rotation in the direction of the action of tensile forces perpendicular to the fracture propagation line (Fig. 2 d, 2 e). The front of deformation bands reaches great depths and sometimes amounts to several hundred microns. As a result, in such areas, cracks easily propagate parallel to the dislocation slip lines, since there are no obstacles in their path. However, if a crack encounters in its path the transversely located bainite blocks, then it starts to slow down on them, as shown in Fig. 2 f. At the same time, the action of high applied tensile stresses sometimes leads to the initiation of secondary cracks in the areas close to the zone where the primary crack stops. Such areas are the MnS inclusions, spherical voids, PAGBs, and a favorable crystallographic texture between the plates (Fig. 2 e, 2 f, 3 a). Thus, more tortuous lines of crack propagation indicate the formation of bainite blocks with different crystallographic textures in these areas and demonstrate the best crack blocking action. In this case, the straight path of crack development implies the accelerated crack propagation in this area (Fig. 2 e). These facts are analyzed in detail by the EBSD method.

In the EBSD analysis of the crystallographic microtexture, grain orientations are represented as a rainbow color coding system on the studied surface and a simple way to identify the local orientation of grains (blocks, plates) in space is provided. The totality of grains forming a polycrystal as a whole consists of many elementary cells superimposed on each other. In this case, inside an elementary cell (or in a grain), one can distinguish various  $\{001\}$   $\langle hkl \rangle$ ,  $\{011\}$   $\langle hkl \rangle$ ,  $\{111\}$   $\langle hkl \rangle$ , etc. systems, along which a dislocation slip occurs. If, during cutting and further grinding of a sample along a certain section, a grain appears where the (111) plane is parallel to the section plane, then in the EBSD pattern, this grain is colored blue (Fig. 3 a). Similarly, grains with (001) are colored red, (101) – green, etc. In other words, the EBSD pattern is a distribution map of grain orientations in the plane of analysis of the section, where the  $\{001\}$ ,  $\{011\}$ ,  $\{111\}$ , etc. planes are parallel to the surface under the study (Fig. 3 a).

The EBSD analysis results clearly showed that the crack propagation nature has the straight-line sections, interruptions, and deflections (Fig. 3 a, 3 b). In particular, the transcrystalline type of crack propagation is typical for sections containing plates with  $\{101\}$   $\langle 0\bar{1}0 \rangle$ ,  $\{100\}$   $\langle 001 \rangle$ , and  $\{111\}$   $\langle \bar{1}00 \rangle$  orientations (Fig. 3 a). In this case, the intercrystalline type of crack propagation was identified for the bainite blocks belonging to the  $\{122\}$   $\langle 2\bar{1}0 \rangle$ ,  $\{111\}$   $\langle \bar{1}00 \rangle$ ,  $\{012\}$   $\langle \bar{1}\bar{1}0 \rangle$ , and  $\{100\}$   $\langle 001 \rangle$  orientations. CSL

grain boundaries between the adjacent plates (laths) demonstrated a significant influence on the crack development nature. The conditions for the formation of CSL grain boundaries in the steel bainitic structure are studied in most detail in the works [22–24]. In particular, it is shown that on CSL grain boundaries of the  $\Sigma 3$ ,  $\Sigma 11$ ,  $\Sigma 25b$ ,  $\Sigma 33c$ , and  $\Sigma 41c$  types, the intense phase transformations begin according to the  $\gamma \rightarrow \alpha$  scheme during the formation of the steel bainitic structure [22]. It is noted that CSL grain boundaries of the  $\Sigma 3$ ,  $\Sigma 11$ , and  $\Sigma 33c$  type are formed predominantly between parallel plates in a martensitic bundle and/or in a bainitic block [22; 23], while the  $\Sigma 25b$  type is characteristic of the martensitic structure [22]. The study showed that the  $\Sigma 41c$  type occurs in triple junctions of plates (laths) in a bundle containing a low-angle boundary, and two  $\Sigma 33c$ -type CSL grain boundaries [23]. On the other hand, in the work [24],  $\Sigma 13$  and  $\Sigma 39$  type CSL grain boundaries were mainly observed on the martensite-austenite and/or bainite-austenite boundaries, and the decrease in the  $\Sigma 11$  proportion was explained by a decrease in the martensite component. The type of  $\Sigma 3$ ,  $\Sigma 11$ ,  $\Sigma 13b$ ,  $\Sigma 25b$ ,  $\Sigma 29a$ ,  $\Sigma 33c$ ,  $\Sigma 39a$ , and  $\Sigma 41c$  CSL grain boundaries revealed in this work during the formation of the bainite structure does not contradict the literature data [22–24]. According to [22; 23], it can be argued that the intense phase transformations begin on the identified CSL boundaries. At the same time, the differences in their proportion are most likely associated with the manifestation of a structural gradient through the thickness of the coupling wall. Moreover, by changing the volume fraction of certain CSL grain boundaries, it is also possible to estimate the type of structures formed [22–24]. In particular, an increased fraction of the  $\Sigma 3$  type CSL grain boundaries can be explained by a multitude of bainite blocks containing parallel plates. A growth of fraction  $\Sigma 11$  near the crack is associated with a growth in the martensitic component, and the strengthening of  $\Sigma 13$  and  $\Sigma 39$  types of CSL indicates a growth in M/A areas in this zone.

The analysis showed that  $\Sigma 3$  CSL grain boundaries between the  $\{122\}$   $\langle 2\bar{1}0 \rangle$  and  $\{111\}$   $\langle \bar{1}00 \rangle$ ,  $\{012\}$   $\langle \bar{1}\bar{1}0 \rangle$ ,  $\{100\}$   $\langle 001 \rangle$  upper bainite plates suppress crack development, and the presence of CSL grain boundaries of the  $\Sigma 13b$ ,  $\Sigma 29a$ , and  $\Sigma 39a$  types, on the contrary, contribute to the accelerated propagation of microcracks. In this regard, it can be concluded that cracks tend to pass through  $\{101\}$   $\langle 0\bar{1}0 \rangle$ ,  $\{100\}$   $\langle 001 \rangle$ , and  $\{111\}$   $\langle \bar{1}00 \rangle$  plates and tend to deflect when colliding with  $\{122\}$   $\langle 2\bar{1}0 \rangle$ ,  $\{013\}$   $\langle 211 \rangle$ ,  $\{133\}$   $\langle \bar{1}\bar{2}1 \rangle$ , and  $\{3\bar{2}\bar{6}\}$   $\langle 201 \rangle$  plates.

## MAIN RESULTS AND CONCLUSIONS

The conducted research showed that when producing the PS coupling according to the GOST 31446 standard, a structural gradient is observed along the thickness of the coupling wall, which consists in the formation of plates of upper and lower bainite, martensite, and martensite-austenite areas. External loads applied to the coupling create stress concentrators at the plate boundaries and on non-metallic inclusions, which lead to the initiation and development of cracks and subsequent failure. The analysis of microtexture studies showed significant differences in the formation of crystallographic texture associated with the presence of a structural gradient during steel tempering.

It is identified that during the PS coupling operation, the  $\{101\} \langle 0\bar{1}0 \rangle$ ,  $\{100\} \langle 001 \rangle$ ,  $\{122\} \langle 2\bar{1}0 \rangle$ ,  $\{013\} \langle 211 \rangle$ , and  $\{3\bar{2}\bar{6}\} \langle 201 \rangle$  orientations of bainitic plates, which are undesirable to resistance at SSC, strengthen. It is shown that the  $\Sigma 3$  CSL grain boundaries between  $\{122\} \langle 2\bar{1}0 \rangle$  and  $\{111\} \langle \bar{1}00 \rangle$ ,  $\{012\} \langle \bar{1}\bar{1}0 \rangle$ ,  $\{100\} \langle 001 \rangle$  bainite plates demonstrate a blocking effect during microcrack propagation. In this case,  $\Sigma 13b$ ,  $\Sigma 29a$ , and  $\Sigma 39a$  CSL grain boundaries between the bainite plates, on the contrary, accelerate the propagation of microcracks. The obtained results are important for the formation in steel of a favorable structure and crystallographic texture resistant to SSC.

## REFERENCES

1. Askari M., Aliofkhaezai M., Afroukhteh S. A Comprehensive Review on Internal Corrosion and Cracking of Oil and Gas Pipelines. *Journal of Natural Gas Science and Engineering*, 2019, vol. 71, article number 102971. DOI: [10.1016/j.jngse.2019.102971](https://doi.org/10.1016/j.jngse.2019.102971).
2. Wang Z.B., Pang L., Zheng Y.G. A review on underdeposit corrosion of pipelines in oil and gas fields: Testing methods, corrosion mechanisms and mitigation strategies. *Corrosion Communications*, 2022, vol. 7, pp. 70–81. DOI: [10.1016/j.corcom.2022.03.007](https://doi.org/10.1016/j.corcom.2022.03.007).
3. Vyboyshchik M.A., Ioffe A.V. Scientific basis of development and the methodology of creation of steels for the production of oilfield casing and tubular goods with the increased strength and corrosion resistance. *Vektor nauki Tolyattinskogo gosudarstvennogo universiteta*, 2019, no. 1, pp. 13–20. DOI: [10.18323/2073-5073-2019-1-13-20](https://doi.org/10.18323/2073-5073-2019-1-13-20).
4. Tkacheva V.E., Markin A.N., Kshnyakin D.V., Mal'tsev D.I., Nosov V.V. Corrosion of downhole equipment in hydrogen sulfur-containing environments. *Praktika protivokorroziionnoy zashchity*, 2021, vol. 26, no. 2, pp. 7–26. DOI: [10.31615/j.corros.prot.2021.100.2-1](https://doi.org/10.31615/j.corros.prot.2021.100.2-1).
5. Sitdikov V.D., Nikolaev A.A., Ivanov G.V., Makatrov A.K., Malinin A.V. Microstructure and crystallographic structure of ferritic steel subjected to stress-corrosion cracking. *Letters on Materials*, 2022, vol. 12, no. 1, pp. 65–70. DOI: [10.22226/2410-3535-2022-1-65-70](https://doi.org/10.22226/2410-3535-2022-1-65-70).
6. Tale S., Ahmed R.M., Elgaddafi R.M., Teodoriu C. Sulfide Stress Cracking of C-110 Steel in a Sour Environment. *Corrosion and Materials Degradation*, 2021, vol. 2, no. 3, pp. 376–396. DOI: [10.3390/cmd2030020](https://doi.org/10.3390/cmd2030020).
7. Cheng Y. *Frank. Stress Corrosion Cracking of Pipelines*. Great Britain, Wiley Publ., 2013. 288 p.
8. Zhou Y. *Pipeline and Energy Plant Piping: Design and Technology*. Netherlands, Elsevier Science Publ., 2013. 392 p.
9. Sitdikov V.D., Nikolaev A.A., Makatrov A.K., Malinin A.V., Filyaeva I.M., Mironov I.V. An integrated approach to identifying causes and mechanisms of destruction of steel tubing couplings. *Neftyanoe khozyaystvo*, 2022, no. 6, pp. 48–51. EDN: [HKAMHC](https://www.edn.ru/HKAMHC).
10. Ren J.-Y., Li C.-S., Han Y., Li E., Gao C., Qiu C. Effect of initial martensite and tempered carbide on mechanical properties of 3Cr2MnNiMo mold steel. *Materials Science and Engineering: A*, 2021, vol. 812, article number 1410801. DOI: [10.1016/j.msea.2021.141080](https://doi.org/10.1016/j.msea.2021.141080).
11. Ohaeri E., Eduok U., Szpunar J. Hydrogen related degradation in pipeline steel: A review. *International Journal of Hydrogen Energy*, 2018, vol. 43, no. 31, pp. 14584–14617. DOI: [10.1016/j.ijhydene.2018.06.064](https://doi.org/10.1016/j.ijhydene.2018.06.064).
12. Pourazizi R., Mohtadi-Bonab M.A., Szpunar J.A. Investigation of different failure modes in oil and natural gas pipeline steels. *Engineering Failure Analysis*, 2020, vol. 109, article number 104400. DOI: [10.1016/j.engfailanal.2020.104400](https://doi.org/10.1016/j.engfailanal.2020.104400).
13. Arafin M.A., Szpunar J.A. A new understanding of intergranular stress corrosion cracking resistance of pipeline steel through grain boundary character and crystallographic texture studies. *Corrosion Science*, 2009, vol. 51, no. 1, pp. 119–128. DOI: [10.1016/j.corsci.2008.10.006](https://doi.org/10.1016/j.corsci.2008.10.006).
14. Liu J., Sun J., Wei S., Lu S. The Effect of Nickel Contents on the Microstructure Evolution and Toughness of 800 MPa Grade Low Carbon Bainite Deposited Metal. *Crystals*, 2021, vol. 11, no. 6, article number 709. DOI: [10.3390/cryst11060709](https://doi.org/10.3390/cryst11060709).
15. Zheng H., Fu L., Ji X., Ding Y., Wang W., Wen M., Shan A. Microstructural evolution and mechanical property of ultrafine-grained pearlitic steel by cold rolling: The influence of cementite morphology. *Materials Science and Engineering: A*, 2021, vol. 824, article number 141860. DOI: [10.1016/j.msea.2021.141860](https://doi.org/10.1016/j.msea.2021.141860).
16. Müller M., Britz D., Ulrich L., Staudt T., Mücklich F. Classification of Bainitic Structures Using Textural Parameters and Machine Learning Techniques. *Metals*, 2020, vol. 10, no. 5, article number 630. DOI: [10.3390/met10050630](https://doi.org/10.3390/met10050630).
17. Qian L., Li Z., Wang T., Li D., Zhang F., Meng J. Roles of pre-formed martensite in below-Ms bainite formation, microstructure, strain partitioning and impact absorption energies of low-carbon bainitic steel. *Journal of Materials Science & Technology*, 2022, vol. 96, pp. 69–84. DOI: [10.1016/j.jmst.2021.05.002](https://doi.org/10.1016/j.jmst.2021.05.002).
18. Pak J.H., Bhadeshia H.K.D.H., Karlsson L., Keehan E. Coalesced bainite by isothermal transformation of reheated weld metal. *Science and Technology of Welding and Joining*, 2008, vol. 13, no. 7, pp. 593–597. DOI: [10.1179/136217108X338926](https://doi.org/10.1179/136217108X338926).
19. Zajac S., Schwinn V., Tacke K.-H. Characterisation and Quantification of Complex Bainitic Microstructures in High and Ultra-High Strength Linepipe Steels. *Materials Science Forum*, 2005, vol. 500-501, pp. 387–394. DOI: [10.4028/www.scientific.net/MSF.500-501.387](https://doi.org/10.4028/www.scientific.net/MSF.500-501.387).
20. Rempelberg C., Allain S.Y.P., Geandier G., Teixeira J., Lebel F., Sourmail T. Carbide-Free Bainite Transformations Above and Below Martensite Start Temperature Investigated by In-Situ High-Energy X-Ray Diffraction. *JOM: The Journal of The Minerals, Metals & Materials Society*, 2021, vol. 73, no. 11, pp. 3181–3194. DOI: [10.1007/s11837-021-04903-8](https://doi.org/10.1007/s11837-021-04903-8).
21. Sun Y., Wang Q., Gu S., He Z., Wang Q., Zhang F. Sulfide Stress Cracking Behavior of a Martensitic Steel Controlled by Tempering Temperature. *Materials (Basel)*, 2018, vol. 11, no. 3, article number 412. DOI: [10.3390/ma11030412](https://doi.org/10.3390/ma11030412).
22. Lobanov M.L., Borodina M.D., Danilov S.V., Pyshmintsev I.Y., Struin A.O. Texture inheritance on phase transition in low-carbon, low-alloy pipe steel after thermomechanical controlled processing. *Steel in Translation*, 2017, vol. 47, no. 11, pp. 710–716. DOI: [10.17073/0368-0797-2017-11-910-918](https://doi.org/10.17073/0368-0797-2017-11-910-918).



- лургия. 2017. Т. 60. № 11. С. 910–918. DOI: [10.17073/0368-0797-2017-11-910-918](https://doi.org/10.17073/0368-0797-2017-11-910-918).
23. Лобанов М.Л., Русаков Г.М., Редикульцев А.А., Беликов С.В., Карабаналов М.С., Струина Е.Р., Гервасьев А.М. Исследование специальных разориентаций в речном мартенсите низкоуглеродистой стали методом ориентационной микроскопии // Физика металлов и металловедение. 2016. Т. 117. № 3. С. 266–271. DOI: [10.7868/S0015323016030086](https://doi.org/10.7868/S0015323016030086).
24. Song T., Cooman B.C.D. Martensite Nucleation at Grain Boundaries Containing Intrinsic Grain Boundary Dislocations // ISIJ International. 2014. Vol. 54. № 10. P. 2394–240. DOI: [10.2355/isijinternational.54.2394](https://doi.org/10.2355/isijinternational.54.2394).

## Особенности микроструктуры и микротекстуры среднеуглеродистой стали, подвергнутой сероводородному растрескиванию под напряжением

© 2023

Малинин Андрей Владимирович<sup>\*1,3</sup>, кандидат технических наук, заместитель генерального директора

Ситдиков Виль Даянович<sup>1,4</sup>, доктор физико-математических наук, заведующий лабораторией

Ткачева Валерия Эдуардовна<sup>1,5</sup>, кандидат технических наук, доцент, главный специалист

Макастров Артем Константинович<sup>1,6</sup>, кандидат технических наук, начальник управления

Валекжанин Илья Владимирович<sup>1,7</sup>, начальник отдела

Маркин Андрей Николаевич<sup>2</sup>, кандидат технических наук, доцент кафедры «Нефтегазовое дело»

<sup>1</sup>ООО «РН-БашНИПИнефть», Уфа (Россия)

<sup>2</sup>Филиал Тюменского индустриального университета в г. Нижневартовске, Нижневартовск (Россия)

\*E-mail: [MalininAV@bnipi.rosneft.ru](mailto:MalininAV@bnipi.rosneft.ru)

<sup>3</sup>ORCID: <https://orcid.org/0000-0003-1185-5648>

<sup>4</sup>ORCID: <https://orcid.org/0000-0002-9948-1099>

<sup>5</sup>ORCID: <https://orcid.org/0000-0001-6927-9781>

<sup>6</sup>ORCID: <https://orcid.org/0000-0002-2822-9072>

<sup>7</sup>ORCID: <https://orcid.org/0000-0001-9472-2968>

Поступила в редакцию 06.12.2022

Принята к публикации 06.03.2023

**Аннотация:** Повышение стойкости стальных изделий к сероводородному растрескиванию под напряжением (СРН) является одной из актуальных тем нефтегазовой промышленности. Среди различных факторов, определяющих устойчивость материала к СРН, выделяется структурно-фазовое состояние самого материала и связанная с ним кристаллографическая текстура. В данной работе эти особенности материала проанализированы методами растровой электронной микроскопии (РЭМ), просвечивающей электронной микроскопии (ПЭМ) и микрорентгеновской дифракции обратно рассеянных электронов (ДОРЭ). В качестве материала исследований выбрана муфта эксплуатационной колонны (ЭК), которая разрушилась по механизму водородного охрупчивания и последующего СРН. Муфта ЭК изготовлена из среднеуглеродистой стали. Впервые методом РЭМ по расположению и взаимной ориентации частиц цементита (Fe<sub>3</sub>C) при больших увеличениях продемонстрированы возможности идентификации в сталях составляющих верхнего бейнита, нижнего бейнита и отпущенного мартенсита. Наличие обнаруженных структурных составляющих стали подтверждено методом ПЭМ. Методом ДОРЭ проведены детальные исследования микротекстуры для установления типа и характера распространения микротрещины. Установлено, что процессы водородного охрупчивания и последующее СРН приводят к формированию {101} <0 $\bar{1}$ 0>, {100} <001>, {122} <2 $\bar{1}$ 0>, {013} <211>, {111} < $\bar{1}$ 00>, {133} < $\bar{1}$ 2 $\bar{1}$ >, {3 $\bar{2}$ 6} <201> ориентаций зерен. Показано, что усиление ориентировок {001} <110>, {100} <001>, {112} <111> и {133} < $\bar{1}$ 2 $\bar{1}$ > типов ухудшают стойкость материала к СРН. Методом ДОРЭ-анализа оценено влияние специальных границ зерен на характер распространения микротрещины. Обнаружено, что специальные границы  $\Sigma$  3 между {122} <2 $\bar{1}$ 0> и {111} < $\bar{1}$ 00>, {012} < $\bar{1}$ 10>, {100} <001> пластинами верхнего бейнита тормозят развитие микротрещины, а границы  $\Sigma$  13b,  $\Sigma$  29a и  $\Sigma$  39a, наоборот, способствуют ускоренному распространению микротрещин. Для сравнительного анализа проведены аналогичные исследования в неразрушенной (исходной) муфте до эксплуатации.

**Ключевые слова:** среднеуглеродистая сталь; бейнитная микроструктура; сероводородное растрескивание под напряжением; кристаллографическая текстура.

**Для цитирования:** Малинин А.В., Ситдиков В.Д., Ткачева В.Э., Макастров А.К., Валекжанин И.В., Маркин А.Н. Особенности микроструктуры и микротекстуры среднеуглеродистой стали, подвергнутой сероводородному растрескиванию под напряжением // Frontier Materials & Technologies. 2023. № 1. С. 33–44. DOI: [10.18323/2782-4039-2023-1-33-44](https://doi.org/10.18323/2782-4039-2023-1-33-44).

## Strain rate sensitivity of mechanical properties of the ZK60 alloy with the high degree of corrosion damage

© 2023

**Evgeny D. Merson**<sup>\*1</sup>, PhD (Physics and Mathematics),  
senior researcher of the Research Institute of Advanced Technologies

**Vitaly A. Poluyanov**<sup>2</sup>, PhD (Engineering),  
junior researcher of the Research Institute of Advanced Technologies

**Pavel N. Myagkikh**<sup>3</sup>, junior researcher of the Research Institute of Advanced Technologies

**Dmitry L. Merson**<sup>4</sup>, Doctor of Sciences (Physics and Mathematics), Professor,  
Director of the Research Institute of Advanced Technologies

Togliatti State University, Togliatti (Russia)

\*E-mail: Mersoned@gmail.com

<sup>1</sup>ORCID: <https://orcid.org/0000-0002-7063-088X>

<sup>2</sup>ORCID: <https://orcid.org/0000-0002-0570-2584>

<sup>3</sup>ORCID: <https://orcid.org/0000-0002-7530-9518>

<sup>4</sup>ORCID: <https://orcid.org/0000-0001-5006-4115>

Received 19.09.2022

Accepted 31.10.2022

**Abstract:** There is a strong belief that hydrogen absorbed by magnesium alloys during corrosion can cause their stress corrosion cracking. One of the characteristic markers indicating the involvement of diffusible hydrogen into the fracture mechanism of metals is the negative strain rate dependence of the embrittlement degree. Recent studies show that the loss of ductility of the ZK60 alloy specimens subjected to a short-term (1.5 h) pre-exposure in a corrosive medium actually decreases with the increasing strain rate. However, after the removal of corrosion products from the surface of the specimens, the strain rate dependence of the ductility loss becomes positive, which indicates the absence of hydrogen in the bulk of the metal. At short-term exposure in a corrosive environment, the deep penetration of hydrogen into a metal could be limited due to the insufficient time for hydrogen diffusion. The paper studies the mechanical behavior of the ZK60 alloy subjected to a longer (12 h) pre-exposure in a corrosive medium followed by tensile testing in air at various strain rates. The authors consider the effect of strain rate, long-term pre-exposure in a corrosive medium, and subsequent removal of corrosion products on the strength, ductility, stages of work hardening, and localized deformation, as well as on the state of the side and fracture surfaces of specimens. It is established that the ductility loss of the specimens pre-exposed in a corrosive medium for 12 h decreases with the increasing strain rate, regardless of whether the corrosion products have been removed from their surface or not. It is shown that in this case, the negative strain rate dependence of the ductility loss is associated not with hydrogen dissolved in the bulk of a metal but with the presence of severe corrosion damage of the specimens' surface. An explanation for the effect of corrosion damage on the mechanical properties and their strain rate sensitivity is proposed.

**Keywords:** magnesium alloys; ZK60 alloy; stress corrosion cracking; corrosion; strain rate; mechanical properties.

**Acknowledgments:** The research was financially supported by the Russian Science Foundation within the scientific project No. 18-19-00592.

**For citation:** Merson E.D., Poluyanov V.A., Myagkikh P.N., Merson D.L. Strain rate sensitivity of mechanical properties of the ZK60 alloy with the high degree of corrosion damage. *Frontier Materials & Technologies*, 2023, no. 1, pp. 45–55. DOI: 10.18323/2782-4039-2023-1-45-55.

### INTRODUCTION

Magnesium-based alloys with the unique complex of mechanical properties are the promising structural material for many manufacturing sectors, including automotive, air-space, and other industries. Moreover, magnesium alloys find their application as a material for bioresorbable implants, which can dissolve in a human body after performing their function. However, their low resistance to corrosion and stress corrosion cracking (SCC) is a great obstacle to a wider application of magnesium alloys in the specified areas.

Fracture of magnesium alloys in aggressive media can occur under the stresses significantly lower than the yield stress [1–3]. Despite the fact that, lately, the scientific community aims the significant efforts at the solution of the SCC problem, many issues related to the nature of

the behavior of magnesium under the effect of a corrosive medium remain open. Particularly, there is not a uniform point of view about the SCC mechanism. This phenomenon develops as a result of the simultaneous exposure of a mechanical stress and corrosive environment and can lead to the embrittlement of the majority of magnesium alloys [4–6]. The most common hypothesis is that the main cause of such embrittlement is hydrogen, which is formed and penetrates into the metal in the process of the corrosion reaction [7–9]. As an argument for this hypothesis, the fact is often mentioned that magnesium alloys are subjected to the so-called pre-exposure stress corrosion cracking (PESCC), which develops as a result of preliminary exposure of the metal to a corrosion environment and manifests itself in the form of a decrease in its mechanical properties and the appearance of a brittle component on a fracture surface during the subsequent mechanical tests in air.

Since the specimen does not come into contact with an aggressive environment directly during the mechanical tests, the observed embrittlement is associated with hydrogen absorbed by the metal in the process of preliminary exposure to a corrosive solution [13–15]. This phenomenon was observed in many magnesium alloys, which were held in corrosive media of various compositions [16–18]. Moreover, it was found that the reduction in the mechanical properties decreases with the increasing strain rate [19; 20]. Such a result is considered as an additional evidence of hydrogen participation in the PESCC mechanism [20], since the negative rate dependence of the loss of ductility is a characteristic feature of many metals and alloys embrittled by hydrogen [21; 22]. This dependence is explained by the fact that with an increase in the strain rate, a smaller amount of hydrogen is able to diffuse to the crack tip; therefore, the crack propagates at a higher external stress rather than in the presence of hydrogen. Recent studies of the ZK60 and AZ31 alloys have shown that the PESCC-associated embrittlement can be completely eliminated by the corrosion products removal from the specimen surface before testing in air, providing that the specimen surface is not severely damaged by anodic dissolution, during the pre-exposure to a corrosive environment [19; 23; 24]. At the same time, gas analysis of specimens with the removed corrosion products showed that the concentration of diffusible hydrogen in their volume is low [23; 24]. Later, it was identified that the negative strain rate dependence of the loss of ductility of specimens kept in a corrosive environment for 1.5 h becomes positive (the same as for specimens not exposed to a corrosive environment) after the corrosion products removal from the surface [19]. Based on the results, the authors concluded that the main reason for the PESCC-associated embrittlement is not hydrogen dissolved in the bulk of the metal but the embrittling agents, such as hydrogen or residual corrosive environment in the layer of corrosion products [19; 23; 24]. However, the study of the effect of the strain rate was carried out in the work [19] on the specimens kept in a corrosive environment for a relatively short period of time – for 1.5 h. It can be suggested that during this time, hydrogen did not have enough time to penetrate deeply into the bulk of the metal, therefore, it quickly escaped from the surface layer to the atmosphere after the removal of corrosion products.

In this regard, it is reasonable to carry out the research of the strain rate effect on the PESCC of the ZK60 alloy subjected to a longer exposure. It is important to emphasize that the previous works showed that the increase in the time of exposure of the ZK60 alloy specimens to a corrosive environment from 1.5 h to 12 h leads to the severe corrosive damages [23], which also can influ-

ence the mechanical properties and their sensitivity to a strain rate change.

The work is aimed to clarify the role of hydrogen and irreversible corrosive damage to a surface in the PESCC mechanism of ZK60 alloy.

## METHODS

The ZK60 commercial alloy produced by the hot extrusion was used as a research material. The alloy chemical composition identified using the ARL 4460 optical-emission spectrometer (Thermo Fisher Scientific) is shown in Table 1. The alloy has a microstructure with an average  $\alpha$ -phase grain size of 3  $\mu\text{m}$ . The microstructure images and its detailed description are given in one of the previous works [25].

The threaded cylindrical specimens for tensile tests with a gauge part of 6×30 mm in size were machined from a rod with a diameter of 25 mm along the extrusion direction. The obtained specimens were soaked at open-circuit potential in an aqueous corrosion solution of 4 % NaCl + 4 %  $\text{K}_2\text{Cr}_2\text{O}_7$  (the same solution was used in the work [19]) for 12 h at room temperature (24 °C) without applying the external mechanical stress. During soaking, only the specimen gauge part was in contact with the corrosive solution. After the exposure, the specimens were removed out of the corrosive environment and cleaned in an ethanol jet, and then dried with compressed air. Corrosion products were removed from some specimens immediately after the exposure by dipping specimens in a standard aqueous solution C.5.4 (20 %  $\text{CrO}_3$  + 1 %  $\text{AgNO}_3$ ) as per GOST R Standard 9.907 for 1 min, followed by rinsing with ethanol and drying with compressed air. Within 5 min after the end of exposure or corrosion products removal, a tensile test of a specimen was started, which was carried out in air at room temperature at constant initial strain rates in the range from  $5 \cdot 10^{-6}$  to  $5 \cdot 10^{-4} \text{ s}^{-1}$  (from 0.01 up to 1 mm/min) using the AG-X plus testing machine (Shimadzu).

For the reference, similar tests were conducted on specimens in the initial (reference) state, which were not subjected to exposure to a corrosive environment. After tests, the fracture and side surfaces of fractured specimens were analyzed using the SIGMA scanning electron microscope (Carl Zeiss).

## RESULTS

### Mechanical properties

Mechanical tests have shown (Fig. 1) that at the same strain rate, both the strength and ductility of specimens decrease remarkably as a result of exposure to a corrosive

*Table 1. Chemical composition of the ZK60 alloy, % wt.  
Таблица 1. Химический состав сплава ZK60, вес. %*

Mg	Al	Zn	Ca	Zr	Fe	Cu	Mn	Ce	Nd	Si
Base	0.002	5.417	0.0004	0.471	0.001	0.002	0.005	0.002	0.003	0.003

environment (Fig. 1 a, 1 b). In this case, the mechanical properties of the specimens are partially restored after the corrosion products removal. It has been identified that with an increase in the strain rate, the elongation of the specimens in the reference state decreases significantly, while their strength increases. At the same time, the ductility of specimens, which were exposed to a corrosive medium before testing, slightly changes with an increase in the strain rate regardless of whether the corrosion products were removed from them or not. The strength of specimens kept in a corrosive environment increases with an increase in the strain rate, but is much weaker than that of specimens in the reference state.

Since the mechanical properties of specimens in the reference state vary greatly depending on the strain rate, to assess the rate sensitivity of the alloy embrittlement degree, it is reasonable to use the value of the ductility and strength

loss with respect to the specimens in the reference state at a given strain rate. The research identified that the value of the ductility loss of specimens exposed to a corrosive environment decreases with the increase in the strain rate, while the strength loss, on the contrary, increases (Fig. 1 c, 1 d). This statement is true both for specimens with the removed corrosion products and for those from which the corrosion products were not removed.

The appearance of the strain-stress diagrams obtained during the testing of the specimens (Fig. 2) indicates that the decrease in the elongation of the specimens in the reference state as a result of an increase in the strain rate occurs mainly due to the reduction of the localized deformation part of the strain-stress diagram, while the change in the length of the strain hardening region is much less pronounced. This pattern is clearly demonstrated in Fig. 3, which shows the graphs of the change in the length of

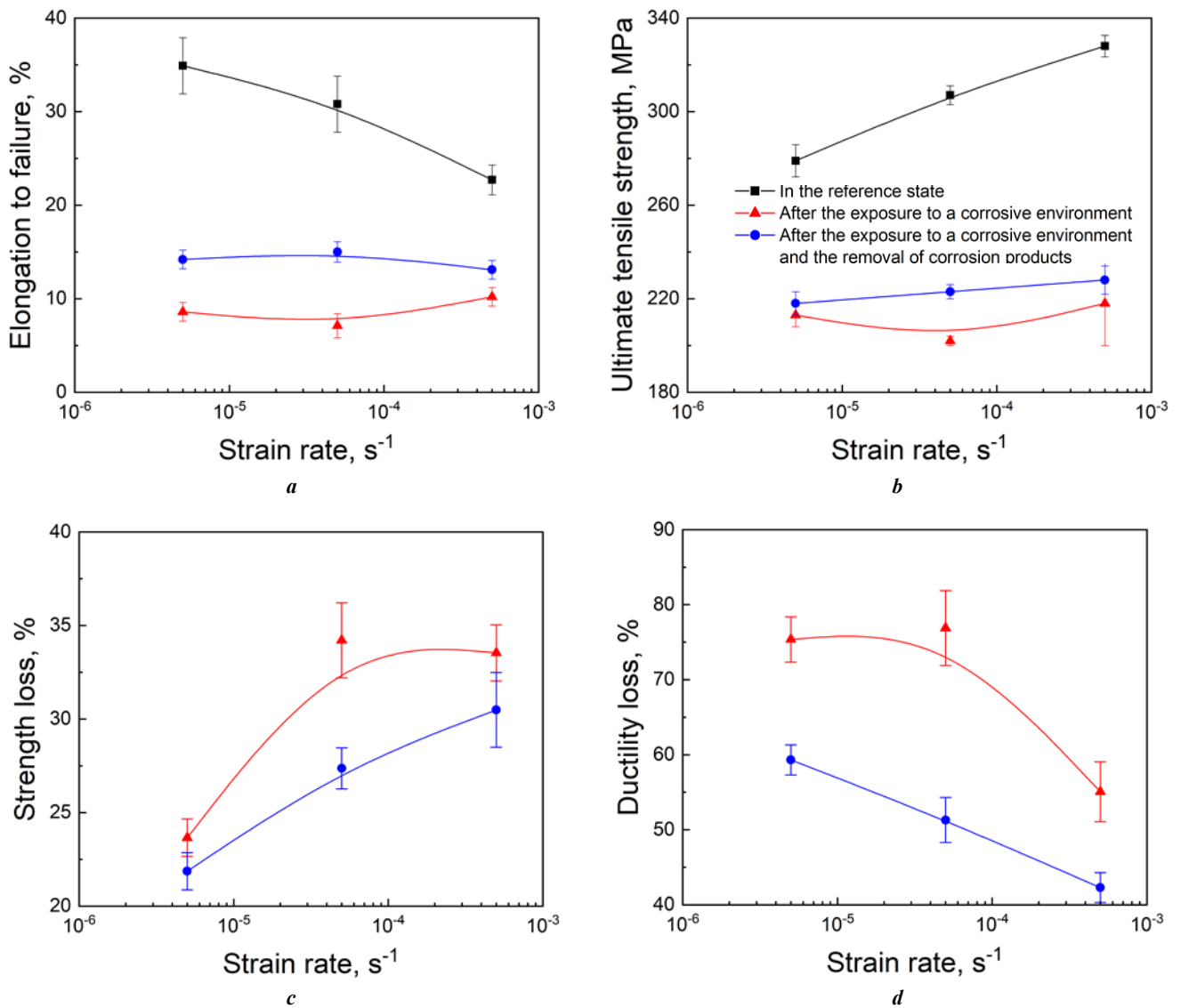


**Fig. 1.** The effect of strain rate on:  
*a* – the elongation to failure; *b* – the ultimate tensile strength;  
*c* – the ductility loss; *d* – the strength loss of the ZK60 alloy in different states

**Рис. 1.** Влияние скорости деформирования на:  
*a* – относительное удлинение; *b* – предел прочности; *c* – потерю пластичности;  
*d* – потерю прочности образцов сплава ZK60 в разных состояниях

the strain hardening –  $\delta_{SH}$  and localized deformation –  $\delta_l$  parts depending on the strain rate for specimens tested in different states. According to the dependencies in Fig. 3,  $\delta_l$  decreases much more than  $\delta_{SH}$  as a result of soaking in a corrosive environment. Moreover, after the corrosion products removal,  $\delta_{SH}$  increases to a level corresponding to the specimens in the reference state, while  $\delta_l$  just scarcely recovers. The  $\delta_{SH}$  and  $\delta_l$  values for specimens kept in a corrosive environment weakly depend on the strain rate, regardless of whether the corrosion products were removed from the specimens' surface or not. It should be noted that for these specimens, with the increase of the strain rate,  $\delta_{SH}$  slightly increases, while  $\delta_l$  slightly decreases.

### The analysis of fracture and side surfaces

Fig. 4 a–f indicates that the side surface of the specimens kept in a corrosive environment before testing has a typical hummocky relief formed as a result of uneven dissolution of the specimen during the soaking in a corrosive environment. To compare, Fig. 4 g–i shows the images of the side surfaces of the specimens in the reference state, which have a completely different relief without any signs of corrosion damage.

It is important to note that on the side surface of the specimens, from which the corrosion products were not removed after the exposure to a corrosive medium, there are numerous cracks oriented perpendicularly to the tensile axis (Fig. 4 a–c). At the same time, the specimens, from which the corrosion products were removed, do not exhibit such cracks (Fig. 4 d–f).

The fractographic analysis showed that in the peripheral part of the fracture surface of the specimens tested after soaking in the medium without the corrosion products removal, there is a typical annular zone with the brittle frac-

ture morphology, the area of which decreases with an increase in the strain rate (Fig. 5 a–c). At the same time, in the specimens, from which the corrosion products were removed before the start of the test (Fig. 5 d–f), as well as in the specimens in the reference state (Fig. 5 g–i), the fracture surfaces are completely ductile without any signs of brittle fracture regardless of the strain rate.

### DISCUSSION

According to the results obtained, the loss of ductility, the value of which characterizes the degree of the alloy embrittlement as a result of PESCC, decreases with an increase in the strain rate for all specimens kept in a corrosive environment for 12 h, including those, from which the corrosion products were removed after the soaking. At the same time, one of our recent works shows that the loss of ductility of the same alloy after keeping in a corrosive environment for 1.5 h and the subsequent corrosion products removal, on the contrary, increases with an increase in the strain rate [19]. Moreover, if the corrosion products were not removed from the specimens' surface after 1.5 h of soaking, the loss of ductility decreased with an increase in the strain rate in the same way as after 12 h of soaking in the present work.

Holding a generally accepted point of view, according to which the negative strain rate dependence of the ductility loss of magnesium alloys during the SCC and PESCC processes is associated with diffusible hydrogen dissolved in them [13; 15; 20], the behavior of the ZK60 alloy mechanical properties depending on the strain rate found in the present and previous [19] works can be wrongly interpreted as follows. As a result of a relatively short exposure to a corrosive environment for 1.5 h, hydrogen does not have enough time to deeply penetrate into the bulk of the metal

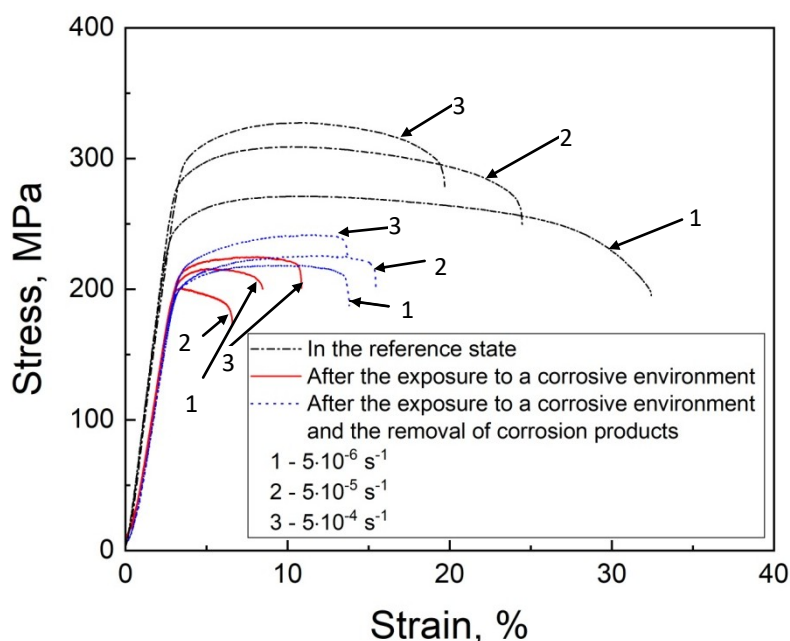
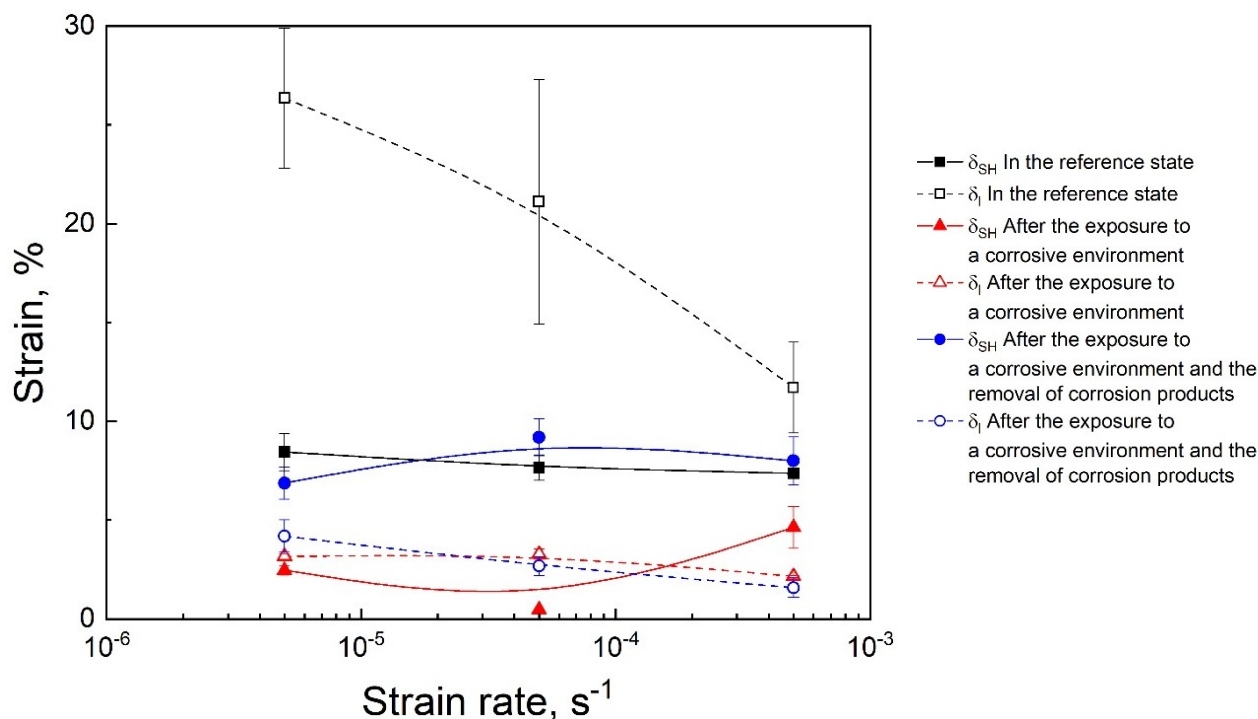


Fig. 2. The effect of strain rate on the stress-strain diagrams of the ZK60 alloy specimens in different states

Рис. 2. Влияние скорости деформирования на диаграммы растяжения образцов сплава ZK60 в разных состояниях



**Fig. 3.** The effect of strain rate on the length of strain-hardening –  $\delta_{SH}$  and localized deformation –  $\delta_l$  parts of the stress-strain diagrams of the ZK60 alloy specimens in different states  
**Рис. 3.** Влияние скорости деформирования на длину участка деформационного упрочнения –  $\delta_{SH}$  и локализованной деформации –  $\delta_l$  на диаграммах растяжения образцов сплава ZK60 в разных состояниях

matrix and is located in the surface layer under the crust of corrosion products preventing its exit from the specimen. Therefore, when retaining a layer of corrosion products on the specimens' surface during the tensile tests, hydrogen participates in the mechanism of nucleation and growth of brittle cracks, which ultimately leads to a premature fracture of the alloy, a decrease in its ductility, and the formation of a brittle zone on the fracture surface. With an increase in the strain rate, the amount of hydrogen that has enough time to diffuse to the crack tip decreases, therefore, the loss of ductility decreases. If the corrosion products are removed from the specimens' surface, then hydrogen is rapidly desorbed from the surface layer into the atmosphere, which leads to the recovery of the alloy ductility and a qualitative change in the dependence of the loss of its ductility on the strain rate. With a longer soaking in a corrosive environment for 12 h, hydrogen has enough time to penetrate much deeper into the bulk of the metal and, therefore, is not completely removed from the specimens after the corrosion products removal. For this reason, both the specimens with the removed corrosion products and those from which the corrosion products were not removed demonstrate a decrease in the loss of ductility with an increase in the strain rate.

An important argument against such an interpretation of the results obtained is the fact that the specimens, from the surface of which the corrosion products were removed after 12 h of exposure, demonstrate the total absence of a brittle zone on the fracture surface and brittle secondary cracks on the side surface, regardless of the strain rate at

which the test was carried out. Thus, the change in the loss of ductility of these specimens with an increase in the strain rate cannot be associated with the suppression of the brittle fracture mechanism, which is an intrinsic feature of the hydrogen embrittlement. Indeed, previous works show that the hydrogen concentration in the specimens kept in a corrosive environment, including for 12 h, and from which the corrosion products were then removed, is insignificant [23; 24]. The authors made an assumption that the main reason for the embrittlement of the specimens pre-exposed to a corrosive environment is the embrittling agents, such as hydrogen or residual corrosive environment located in the corrosion products layer [19; 23; 24]. The details of this mechanism will be researched in future studies. In the present work, it is reasonable to consider the features of the rate dependence of the properties of specimens with the removed corrosion products, in which these embrittling agents are totally absent.

If the fracture of specimens with the removed corrosion products occurs according to the common ductile mechanism, the same as for specimens in the reference state, the same character of the dependence of ductility on the strain rate for these two types of specimens should also be expected. In particular, this is exactly what was observed when the exposure time was 1.5 h [19]: the ductility of the specimens, both in the initial state and after the corrosion products removal, decreased with an increase in the strain rate, and, moreover, for the specimens with the removed corrosion products, a decrease in ductility with an increase in the strain rate was even stronger than that

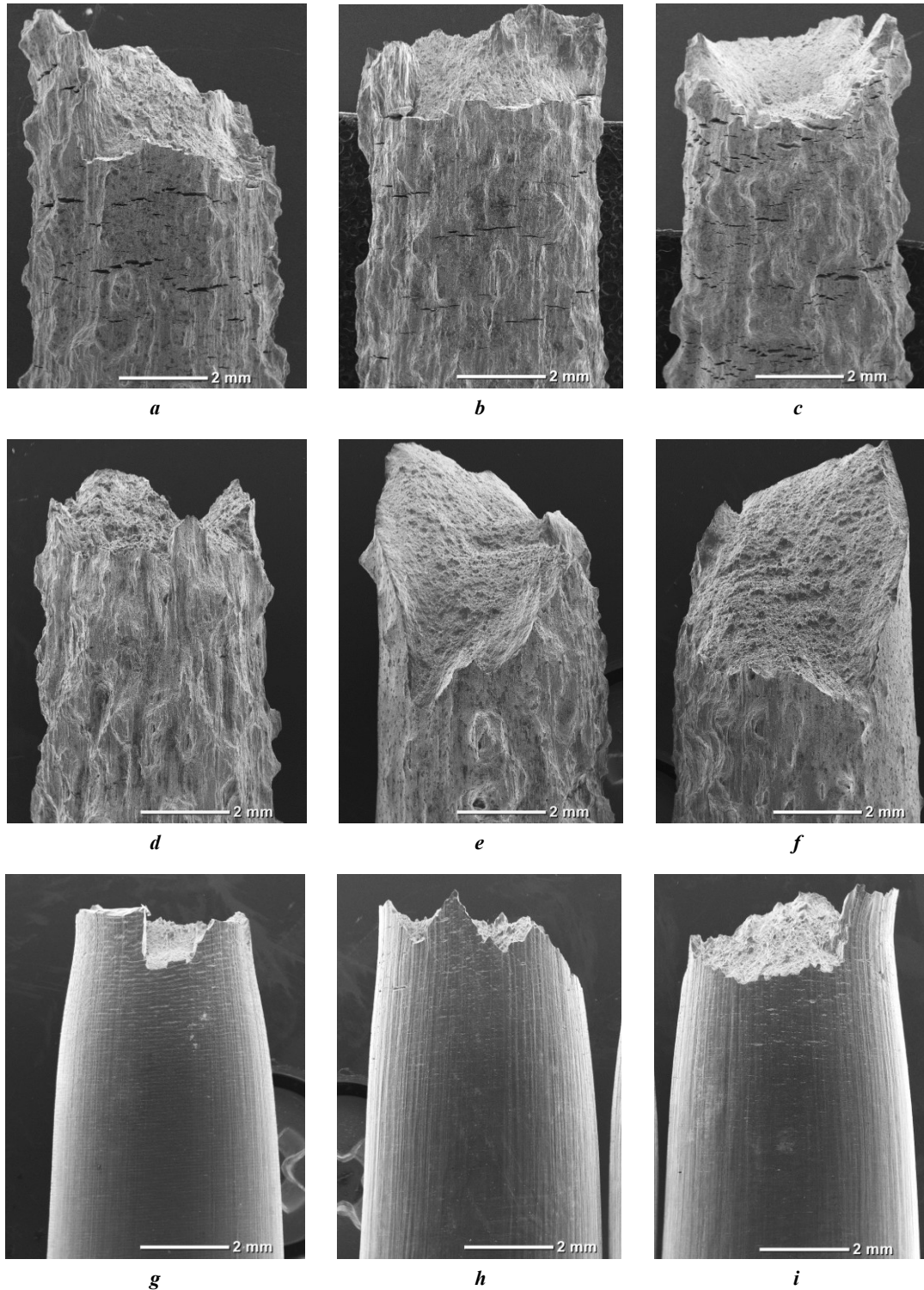


**Fig. 4.** The effect of strain rate (**a, d, g** –  $5 \cdot 10^{-6} \text{ s}^{-1}$ ; **b, e, h** –  $5 \cdot 10^{-5} \text{ s}^{-1}$ ; **c, f, i** –  $5 \cdot 10^{-4} \text{ s}^{-1}$ ) on the state of the side surface of the specimens tensile-tested in air:

**a–c** – after pre-exposure to the corrosive medium;

**d–f** – after pre-exposure to the corrosive medium and removal of corrosion products;

**g–i** – in the reference state. SEM

**Рис. 4.** Влияние скорости деформирования (**a, d, g** –  $5 \cdot 10^{-6} \text{ с}^{-1}$ ; **b, e, h** –  $5 \cdot 10^{-5} \text{ с}^{-1}$ ; **c, f, i** –  $5 \cdot 10^{-4} \text{ с}^{-1}$ ) на состояние боковой поверхности образцов, испытанных на растяжение на воздухе:

**a–c** – после выдержки в коррозионной среде;

**d–f** – после выдержки в коррозионной среде и удаления продуктов коррозии;

**g–i** – в исходном состоянии. СЭМ

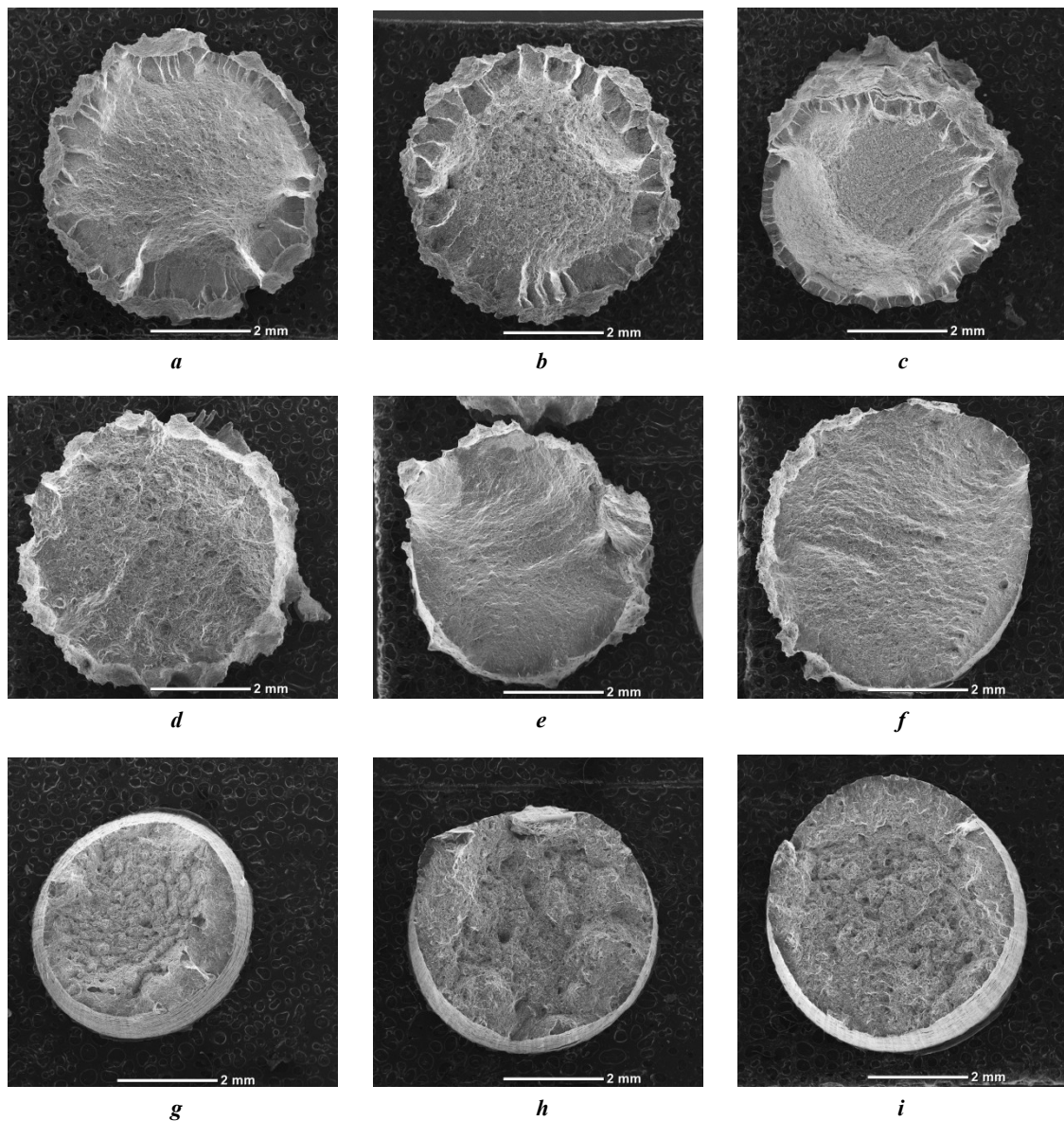


**Fig. 5.** The effect of strain rate (*a, d, g* –  $5 \cdot 10^{-6} \text{ s}^{-1}$ ; *b, e, h* –  $5 \cdot 10^{-5} \text{ s}^{-1}$ ; *c, f, i* –  $5 \cdot 10^{-4} \text{ s}^{-1}$ ) on the state of the fracture surface of the specimens tensile-tested in air:

*a–c* – after pre-exposure to the corrosive medium;

*d–f* – after pre-exposure to the corrosive medium and removal of corrosion products;

*g–i* – in the reference state. SEM

**Рис. 5.** Влияние скорости деформирования (*a, d, g* –  $5 \cdot 10^{-6} \text{ с}^{-1}$ ; *b, e, h* –  $5 \cdot 10^{-5} \text{ с}^{-1}$ ; *c, f, i* –  $5 \cdot 10^{-4} \text{ с}^{-1}$ ) на состояние излома образцов, испытанных на растяжение на воздухе:

*a–c* – после выдержки в коррозионной среде;

*d–f* – после выдержки в коррозионной среде и удаления продуктов коррозии;

*g–i* – в исходном состоянии. СЭМ

of the specimens in the initial state, due to which an increase in the loss of ductility occurred. However, as the results of this work show, in the case of soaking for 12 h with an increase in the strain rate, the ductility of the specimens with the removed corrosion products remains practically unchanged.

It might be supposed that the difference in the rate sensitivity of the ductility of the reference and pre-exposed specimens with the removed corrosion products can be associated with irreversible corrosion damage, the degree of which in the case of soaking for 12 h is significantly higher than after soaking for 1.5 h. Thus, the work [23] shows that

the surface roughness and the decrease in the cross section of the ZK60 alloy specimens resulting from corrosion after 12 h soaking in a 4 % NaCl + 4 %  $\text{K}_2\text{Cr}_2\text{O}_7$  solution were 4 times higher than after 1.5 h.

A decrease in the cross section of the specimens resulting from keeping in the medium leads to a decrease in the load of yielding and the maximum load to fracture, which results in an apparent decrease in the yield and ultimate tensile strength. A surface roughness increase associated with the occurrence of numerous deep corrosion pits, probably, greatly facilitates the initiation of cracks, which mainly affects the ductility of the specimens. The results

of the analysis of tensile diagrams showed that the drop of ductility resulting from 12 h exposure to a corrosive environment occurs primarily due to a great reduction in the length of the localized deformation part  $\delta_l$ , which, unlike  $\delta_{SH}$ , is not recovered after the corrosion products removal. It is well known that the formation of ductile cracks in metallic materials occurs due to the coalescence of voids appearing during tension of smooth specimens after the significant plastic deformation at the stage of localized flow in the neck area [26]. Apparently, in specimens subjected to the exposure to a corrosive medium, ductile cracks are formed due to the merging of corrosion pits; therefore, plastic deformation is not needed for the formation of voids, and fracture occurs soon after the deformation is localized in the neck.

According to the results of this work, a decrease in the elongation of the reference specimens with an increase in the strain rate occurs as well mainly due to a decrease in  $\delta_l$ . Consequently, an increase in the strain rate does not affect the elongation of the specimens with the removed corrosion products, since their  $\delta_l$  has already been reduced almost to a minimum due to severe corrosion damage. It should be mentioned that after the removal of corrosion products from the specimens, which were kept in a corrosive environment for 1.5 h and, thus, had much weaker corrosive damage, both  $\delta_l$  and  $\delta_{SH}$  were completely restored; therefore, an increase in the strain rate in this case led to a decrease in elongation as it was with the specimens in the reference state.

The results obtained indicate that the presence of a negative strain rate dependence of the ductility loss during PESCC of magnesium alloys is not always an unambiguous indicator of the diffusible hydrogen participation in the fracture mechanism.

According to the results of this study, in addition to a decrease in ductility with an increase in the strain rate, there is an increase in the strength of the specimens both in the initial state and after soaking and corrosion products removal. However, the strength of specimens kept in a corrosive medium grows much weaker with an increase in the strain rate than that of the specimens in the reference state. For this reason, the strength loss of specimens kept in a corrosive medium increases with an increase in the strain rate.

Differences in the rate sensitivity of strength of the specimens in the reference state and specimens kept in a corrosive environment can presumably be associated with corrosion damage as well. Probably, with an increase in the strain rate, the alloy becomes more sensitive to stress risers which are corrosion pits. At a low strain rate, they have enough time to become plastically blunt, which is accompanied by the stress relaxation near the stress risers, while at a high strain rate, the same pits remain relatively sharp, and therefore, the local fracture stress near them is achieved at a lower external stress.

Thus, on the one hand, an increase in the strain rate leads to an increase in the ultimate strength due to the difficulty of plastic deformation in the entire volume of the specimen. On the other hand, the local hindrance of plastic deformation near the stress risers prevents their blunting and, as a result, leads to a decrease in the ultimate tensile strength. Since the specimens in the reference state do not have large stress risers, their effect on the ultimate

tensile strength is insignificant, and it greatly increases with an increase in the strain rate. In addition, with the increasing strain rate of the specimens kept in a corrosive medium, a decrease in the ultimate tensile strength associated with an increase in the sharpness of stress risers compensates for the increase in the ultimate tensile strength from the hindrance of plastic deformation over the bulk of the specimen as a whole.

## MAIN RESULTS AND CONCLUSIONS

1. An increase in the degree of corrosion damage on the surface of the ZK60 alloy specimens resulting from an increase in the duration of their preliminary exposure to a corrosive environment can lead to a fundamental change in the strain rate sensitivity of the mechanical properties of these specimens during subsequent tests in air.

2. A decrease in the ZK60 alloy elongation with an increase in the strain rate occurs mainly due to a reduction of the localized deformation stage.

3. The formation of deep pits and other corrosion damages leads to a reduction of the length of the localized deformation part of the stress-strain diagram and does not affect the length of the strain hardening region.

4. With an increase in the strain rate, the elongation of specimens with a high degree of corrosion damage practically does not change, and the loss of their ductility with respect to the specimens not subjected to corrosion increases, since the localized deformation stage in the specimens damaged by corrosion is virtually absent.

5. The negative strain rate dependence of the ductility loss of the specimens, from the surface of which the corrosion products were removed after a long exposure to a corrosive medium, is associated with a high degree of corrosion damage to their surface and not with the presence of hydrogen in their bulk.

## REFERENCES

1. Dubey D., Kadali K., Panda S., Kumar A., Jain J., Mondal K., Singh S. Comparative study on the stress corrosion cracking susceptibility of AZ80 and AZ31 magnesium alloys. *Materials Science and Engineering A*, 2020, vol. 792, article number 139793. DOI: [10.1016/j.msea.2020.139793](https://doi.org/10.1016/j.msea.2020.139793).
2. He L., Yang J., Xiong Y., Song R. Effect of solution pH on stress corrosion cracking behavior of modified AZ80 magnesium alloy in simulated body fluid. *Materials Chemistry and Physics*, 2021, vol. 261, article number 124232. DOI: [10.1016/j.matchemphys.2021.124232](https://doi.org/10.1016/j.matchemphys.2021.124232).
3. Xiong Y., Shen Y., He L., Yang Z., Song R. Stress corrosion cracking behavior of LSP/MAO treated magnesium alloy during SSRT in a simulated body fluid. *Journal of Alloys and Compounds*, 2020, vol. 822, article number 153707. DOI: [10.1016/j.jallcom.2020.153707](https://doi.org/10.1016/j.jallcom.2020.153707).
4. Xiong Y., Hu X., Weng Z., Song R. Stress Corrosion Resistance of Laser Shock Peening/Microarc Oxidation Reconstruction Layer Fabricated on AZ80 Magnesium Alloy in Simulated Body Fluid. *Journal of Materials Engineering and Performance*, 2020, vol. 29, no. 9, pp. 5750–5756. DOI: [10.1007/s11665-020-05076-2](https://doi.org/10.1007/s11665-020-05076-2).
5. Merson E.D., Poluyanov V.A., Myagkikh P.N., Vinogradov A.Yu. Effect of grain size on mechanical

- properties and hydrogen occluding capacity of pure magnesium and alloy MA14 subjected to stress-corrosion cracking. *Letters on Materials*, 2020, vol. 10, no. 1, pp. 94–99. DOI: [10.22226/2410-3535-2020-1-94-99](https://doi.org/10.22226/2410-3535-2020-1-94-99).
6. Chen L., Blawert C., Yang J., Hou R., Wang X., Zheludkevich M.L., Li W. The stress corrosion cracking behaviour of biomedical Mg-1Zn alloy in synthetic or natural biological media. *Corrosion Science*, 2020, vol. 175, article number 108876. DOI: [10.1016/j.corsci.2020.108876](https://doi.org/10.1016/j.corsci.2020.108876).
  7. Gong X., Chen J., Yan H., Xia W., Su B., Yu Z., Yin H. Effects of minor Sr addition on biocorrosion and stress corrosion cracking of as-cast Mg-4Zn alloys. *Corrosion*, 2020, vol. 76, no. 1, pp. 71–81. DOI: [10.5006/3341](https://doi.org/10.5006/3341).
  8. Kappes M., Iannuzzi M., Carranza R.M. Hydrogen Embrittlement of Magnesium and Magnesium Alloys: A Review. *Journal of the Electrochemical Society*, 2013, vol. 160, no. 4, pp. C168–C178. DOI: [10.1149/2.023304jes](https://doi.org/10.1149/2.023304jes).
  9. Wang S.D., Xu D.K., Wang B.J., Sheng L.Y., Qiao Y.X., Han E.-H., Dong C. Influence of phase dissolution and hydrogen absorption on the stress corrosion cracking behavior of Mg-7%Gd-5%Y-1%Nd-0.5%Zr alloy in 3.5 wt.% NaCl solution. *Corrosion Science*, 2018, vol. 142, pp. 185–200. DOI: [10.1016/j.corsci.2018.07.019](https://doi.org/10.1016/j.corsci.2018.07.019).
  10. Prabhu D.B., Nampoothiri J., Elakkiya V., Narmadha R., Selvakumar R., Sivasubramanian R., Gopalakrishnan P., Ravi K.R. Elucidating the role of microstructural modification on stress corrosion cracking of biodegradable Mg-4Zn alloy in simulated body fluid. *Materials Science and Engineering C*, 2020, vol. 106, article number 110164. DOI: [10.1016/j.msec.2019.110164](https://doi.org/10.1016/j.msec.2019.110164).
  11. Bobby K.M., Dietzel W. Pitting-induced hydrogen embrittlement of magnesium-aluminium alloy. *Materials and Design*, 2012, vol. 42, pp. 321–326. DOI: [10.1016/j.matdes.2012.06.007](https://doi.org/10.1016/j.matdes.2012.06.007).
  12. Jiang P., Blawert C., Bohlen J., Zheludkevich M.L. Corrosion performance, corrosion fatigue behavior and mechanical integrity of an extruded Mg4Zn0.2Sn alloy. *Journal of Materials Science and Technology*, 2020, vol. 59, pp. 107–116. DOI: [10.1016/j.jmst.2020.04.042](https://doi.org/10.1016/j.jmst.2020.04.042).
  13. Kappes M., Iannuzzi M., Carranza R.M. Pre-exposure embrittlement and stress corrosion cracking of magnesium alloy AZ31B in chloride solutions. *Corrosion*, 2014, vol. 70, no. 7, pp. 667–677. DOI: [10.5006/1172](https://doi.org/10.5006/1172).
  14. Chen K., Lu Y., Tang H., Gao Y., Zhao F., Gu X., Fan Y. Effect of strain on degradation behaviors of WE43, Fe and Zn wires. *Acta Biomaterialia*, 2020, vol. 113, pp. 627–645. DOI: [10.1016/j.actbio.2020.06.028](https://doi.org/10.1016/j.actbio.2020.06.028).
  15. Stampella R.S., Procter R.P.M., Ashworth V. Environmentally-induced cracking of magnesium. *Corrosion Science*, 1984, vol. 24, no. 4, pp. 325–341. DOI: [10.1016/0010-938X\(84\)90017-9](https://doi.org/10.1016/0010-938X(84)90017-9).
  16. Song R.G., Blawert C., Dietzel W., Atrens A. A study on stress corrosion cracking and hydrogen embrittlement of AZ31 magnesium alloy. *Materials Science and Engineering A*, 2005, vol. 399, no. 1-2, pp. 308–317. DOI: [10.1016/j.msea.2005.04.003](https://doi.org/10.1016/j.msea.2005.04.003).
  17. Wang S.D., Xu D.K., Wang B.J., Sheng L.Y., Han E.H., Dong C. Effect of solution treatment on stress corrosion cracking behavior of an as-forged Mg-Zn-Y-Zr alloy. *Scientific Reports*, 2016, vol. 6, article number 29471. DOI: [10.1038/srep29471](https://doi.org/10.1038/srep29471).
  18. Jafari S., Raman R.K.S., Davies C.H.J. Stress corrosion cracking of an extruded magnesium alloy (ZK21) in a simulated body fluid. *Engineering Fracture Mechanics*, 2018, vol. 201, pp. 47–55. DOI: [10.1016/j.engfracmech.2018.09.002](https://doi.org/10.1016/j.engfracmech.2018.09.002).
  19. Merson E., Poluyanov V., Myagkikh P., Merson D., Vinogradov A. Effect of strain rate and corrosion products on pre-exposure stress corrosion cracking in the ZK60 magnesium alloy. *Materials Science and Engineering A*, 2022, vol. 830, article number 142304. DOI: [10.1016/j.msea.2021.142304](https://doi.org/10.1016/j.msea.2021.142304).
  20. Chakrapani D.G., Pugh E.N. Hydrogen embrittlement in a Mg-Al alloy. *Metallurgical Transactions A*, 1976, vol. 7, no. 2, pp. 173–178. DOI: [10.1007/BF02644454](https://doi.org/10.1007/BF02644454).
  21. Merson E.D., Myagkikh P.N., Klevtsov G.V., Merson D.L., Vinogradov A. Effect of Hydrogen Concentration and Strain Rate on Hydrogen Embrittlement of Ultra-Fine-Grained Low-Carbon Steel. *Advanced Structured Materials*, 2021, vol. 143, pp. 159–170 p. DOI: [10.1007/978-3-030-66948-5\\_10](https://doi.org/10.1007/978-3-030-66948-5_10).
  22. Wu X.Q., Kim I.S. Effects of strain rate and temperature on tensile behavior of hydrogen-charged SA508 Cl.3 pressure vessel steel. *Materials Science and Engineering A*, 2003, vol. 348, no. 1-2, pp. 309–318. DOI: [10.1016/s0921-5093\(02\)00737-2](https://doi.org/10.1016/s0921-5093(02)00737-2).
  23. Merson E., Poluyanov V., Myagkikh P., Merson D., Vinogradov A. On the role of pre-exposure time and corrosion products in stress-corrosion cracking of ZK60 and AZ31 magnesium alloys. *Materials Science and Engineering A*, 2021, vol. 806, article number 140876. DOI: [10.1016/j.msea.2021.140876](https://doi.org/10.1016/j.msea.2021.140876).
  24. Merson E., Poluyanov V., Myagkikh P., Merson D., Vinogradov A. Inhibiting stress corrosion cracking by removing corrosion products from the Mg-Zn-Zr alloy pre-exposed to corrosion solutions. *Acta Materialia*, 2021, vol. 205, article number 116570. DOI: [10.1016/j.actamat.2020.116570](https://doi.org/10.1016/j.actamat.2020.116570).
  25. Merson E., Myagkikh P., Poluyanov V., Merson D., Vinogradov A. On the role of hydrogen in stress corrosion cracking of magnesium and its alloys: Gas-analysis study. *Materials Science and Engineering A*, 2019, vol. 748, pp. 337–346. DOI: [10.1016/j.msea.2019.01.107](https://doi.org/10.1016/j.msea.2019.01.107).
  26. Li H., Fu M. Damage Evolution and Ductile Fracture. *Deformation-Based Processing of Materials. Behavior, Performance, Modeling, and Control*, 2019, pp. 85–136. DOI: [10.1016/B978-0-12-814381-0.00003-0](https://doi.org/10.1016/B978-0-12-814381-0.00003-0).

#### СПИСОК ЛИТЕРАТУРЫ

1. Dubey D., Kadali K., Panda S., Kumar A., Jain J., Mondal K., Singh S. Comparative study on the stress corrosion cracking susceptibility of AZ80 and AZ31 magnesium alloys // *Materials Science and Engineering A*. 2020. Vol. 792. Article number 139793. DOI: [10.1016/j.msea.2020.139793](https://doi.org/10.1016/j.msea.2020.139793).
2. He L., Yang J., Xiong Y., Song R. Effect of solution pH on stress corrosion cracking behavior of modified AZ80 magnesium alloy in simulated body fluid // *Materials Chemistry and Physics*. 2021. Vol. 261. Article number 124232. DOI: [10.1016/j.matchemphys.2021.124232](https://doi.org/10.1016/j.matchemphys.2021.124232).

3. Xiong Y., Shen Y., He L., Yang Z., Song R. Stress corrosion cracking behavior of LSP/MAO treated magnesium alloy during SSRT in a simulated body fluid // *Journal of Alloys and Compounds*. 2020. Vol. 822. Article number 153707. DOI: [10.1016/j.jallcom.2020.153707](https://doi.org/10.1016/j.jallcom.2020.153707).
4. Xiong Y., Hu X., Weng Z., Song R. Stress Corrosion Resistance of Laser Shock Peening/Microarc Oxidation Reconstruction Layer Fabricated on AZ80 Magnesium Alloy in Simulated Body Fluid // *Journal of Materials Engineering and Performance*. 2020. Vol. 29. № 9. P. 5750–5756. DOI: [10.1007/s11665-020-05076-2](https://doi.org/10.1007/s11665-020-05076-2).
5. Merson E.D., Poluyanov V.A., Myagkikh P.N., Vinogradov A.Yu. Effect of grain size on mechanical properties and hydrogen occluding capacity of pure magnesium and alloy MA14 subjected to stress-corrosion cracking // *Letters on Materials*. 2020. Vol. 10. № 1. P. 94–99. DOI: [10.22226/2410-3535-2020-1-94-99](https://doi.org/10.22226/2410-3535-2020-1-94-99).
6. Chen L., Blawert C., Yang J., Hou R., Wang X., Zheludkevich M.L., Li W. The stress corrosion cracking behaviour of biomedical Mg-1Zn alloy in synthetic or natural biological media // *Corrosion Science*. 2020. Vol. 175. Article number 108876. DOI: [10.1016/j.corsci.2020.108876](https://doi.org/10.1016/j.corsci.2020.108876).
7. Gong X., Chen J., Yan H., Xia W., Su B., Yu Z., Yin H. Effects of minor Sr addition on biocorrosion and stress corrosion cracking of as-cast Mg-4Zn alloys // *Corrosion*. 2020. Vol. 76. № 1. P. 71–81. DOI: [10.5006/3341](https://doi.org/10.5006/3341).
8. Kappes M., Iannuzzi M., Carranza R.M. Hydrogen Embrittlement of Magnesium and Magnesium Alloys: A Review // *Journal of the Electrochemical Society*. 2013. Vol. 160. № 4. P. C168–C178. DOI: [10.1149/2.023304jes](https://doi.org/10.1149/2.023304jes).
9. Wang S.D., Xu D.K., Wang B.J., Sheng L.Y., Qiao Y.X., Han E.-H., Dong C. Influence of phase dissolution and hydrogen absorption on the stress corrosion cracking behavior of Mg-7%Gd-5%Y-1%Nd-0.5%Zr alloy in 3.5 wt.% NaCl solution // *Corrosion Science*. 2018. Vol. 142. P. 185–200. DOI: [10.1016/j.corsci.2018.07.019](https://doi.org/10.1016/j.corsci.2018.07.019).
10. Prabhu D.B., Nampoothiri J., Elakkiya V., Narmadha R., Selvakumar R., Sivasubramanian R., Gopalakrishnan P., Ravi K.R. Elucidating the role of microstructural modification on stress corrosion cracking of biodegradable Mg-4Zn alloy in simulated body fluid // *Materials Science and Engineering C*. 2020. Vol. 106. Article number 110164. DOI: [10.1016/j.msec.2019.110164](https://doi.org/10.1016/j.msec.2019.110164).
11. Bobby K.M., Dietzel W. Pitting-induced hydrogen embrittlement of magnesium-aluminium alloy // *Materials and Design*. 2012. Vol. 42. P. 321–326. DOI: [10.1016/j.matdes.2012.06.007](https://doi.org/10.1016/j.matdes.2012.06.007).
12. Jiang P., Blawert C., Bohlen J., Zheludkevich M.L. Corrosion performance, corrosion fatigue behavior and mechanical integrity of an extruded Mg4Zn0.2Sn alloy // *Journal of Materials Science and Technology*. 2020. Vol. 59. P. 107–116. DOI: [10.1016/j.jmst.2020.04.042](https://doi.org/10.1016/j.jmst.2020.04.042).
13. Kappes M., Iannuzzi M., Carranza R.M. Pre-exposure embrittlement and stress corrosion cracking of magnesium alloy AZ31B in chloride solutions // *Corrosion*. 2014. Vol. 70. № 7. P. 667–677. DOI: [10.5006/1172](https://doi.org/10.5006/1172).
14. Chen K., Lu Y., Tang H., Gao Y., Zhao F., Gu X., Fan Y. Effect of strain on degradation behaviors of WE43, Fe and Zn wires // *Acta Biomaterialia*. 2020. Vol. 113. P. 627–645. DOI: [10.1016/j.actbio.2020.06.028](https://doi.org/10.1016/j.actbio.2020.06.028).
15. Stampella R.S., Procter R.P.M., Ashworth V. Environmentally-induced cracking of magnesium // *Corrosion Science*. 1984. Vol. 24. № 4. P. 325–341. DOI: [10.1016/0010-938X\(84\)90017-9](https://doi.org/10.1016/0010-938X(84)90017-9).
16. Song R.G., Blawert C., Dietzel W., Atrens A. A study on stress corrosion cracking and hydrogen embrittlement of AZ31 magnesium alloy // *Materials Science and Engineering A*. 2005. Vol. 399. № 1-2. P. 308–317. DOI: [10.1016/j.msea.2005.04.003](https://doi.org/10.1016/j.msea.2005.04.003).
17. Wang S.D., Xu D.K., Wang B.J., Sheng L.Y., Han E.H., Dong C. Effect of solution treatment on stress corrosion cracking behavior of an as-forged Mg-Zn-Y-Zr alloy // *Scientific Reports*. 2016. Vol. 6. Article number 29471. DOI: [10.1038/srep29471](https://doi.org/10.1038/srep29471).
18. Jafari S., Raman R.K.S., Davies C.H.J. Stress corrosion cracking of an extruded magnesium alloy (ZK21) in a simulated body fluid // *Engineering Fracture Mechanics*. 2018. Vol. 201. P. 47–55. DOI: [10.1016/j.engfracmech.2018.09.002](https://doi.org/10.1016/j.engfracmech.2018.09.002).
19. Merson E., Poluyanov V., Myagkikh P., Merson D., Vinogradov A. Effect of strain rate and corrosion products on pre-exposure stress corrosion cracking in the ZK60 magnesium alloy // *Materials Science and Engineering A*. 2022. Vol. 830. Article number 142304. DOI: [10.1016/j.msea.2021.142304](https://doi.org/10.1016/j.msea.2021.142304).
20. Chakrapani D.G., Pugh E.N. Hydrogen embrittlement in a Mg-Al alloy // *Metallurgical Transactions A*. 1976. Vol. 7. № 2. P. 173–178. DOI: [10.1007/BF02644454](https://doi.org/10.1007/BF02644454).
21. Merson E.D., Myagkikh P.N., Klevtsov G.V., Merson D.L., Vinogradov A. Effect of Hydrogen Concentration and Strain Rate on Hydrogen Embrittlement of Ultra-Fine-Grained Low-Carbon Steel // *Advanced Structured Materials*. 2021. Vol. 143. P. 159–170 p. DOI: [10.1007/978-3-030-66948-5\\_10](https://doi.org/10.1007/978-3-030-66948-5_10).
22. Wu X.Q., Kim I.S. Effects of strain rate and temperature on tensile behavior of hydrogen-charged SA508 C1.3 pressure vessel steel // *Materials Science and Engineering A*. 2003. Vol. 348. № 1-2. P. 309–318. DOI: [10.1016/s0921-5093\(02\)00737-2](https://doi.org/10.1016/s0921-5093(02)00737-2).
23. Merson E., Poluyanov V., Myagkikh P., Merson D., Vinogradov A. On the role of pre-exposure time and corrosion products in stress-corrosion cracking of ZK60 and AZ31 magnesium alloys // *Materials Science and Engineering A*. 2021. Vol. 806. Article number 140876. DOI: [10.1016/j.msea.2021.140876](https://doi.org/10.1016/j.msea.2021.140876).
24. Merson E., Poluyanov V., Myagkikh P., Merson D., Vinogradov A. Inhibiting stress corrosion cracking by removing corrosion products from the Mg-Zn-Zr alloy pre-exposed to corrosion solutions // *Acta Materialia*. 2021. Vol. 205. Article number 116570. DOI: [10.1016/j.actamat.2020.116570](https://doi.org/10.1016/j.actamat.2020.116570).
25. Merson E., Myagkikh P., Poluyanov V., Merson D., Vinogradov A. On the role of hydrogen in stress corrosion cracking of magnesium and its alloys: Gas-analysis study // *Materials Science and Engineering A*. 2019. Vol. 748. P. 337–346. DOI: [10.1016/j.msea.2019.01.107](https://doi.org/10.1016/j.msea.2019.01.107).
26. Li H., Fu M. Damage Evolution and Ductile Fracture // *Deformation-Based Processing of Materials. Behavior, Performance, Modeling, and Control*. 2019. P. 85–136. DOI: [10.1016/B978-0-12-814381-0.00003-0](https://doi.org/10.1016/B978-0-12-814381-0.00003-0).

# Скоростная чувствительность механических свойств сплава ZK60 с высокой степенью коррозионных повреждений

© 2023

*Мерсон Евгений Дмитриевич*\*<sup>1</sup>, кандидат физико-математических наук, старший научный сотрудник НИИ прогрессивных технологий

*Полуянов Виталий Александрович*<sup>2</sup>, кандидат технических наук, младший научный сотрудник НИИ прогрессивных технологий

*Мягких Павел Николаевич*<sup>3</sup>, младший научный сотрудник НИИ прогрессивных технологий

*Мерсон Дмитрий Львович*<sup>4</sup>, доктор физико-математических наук, профессор, директор НИИ прогрессивных технологий

*Тольяттинский государственный университет, Тольятти (Россия)*

\*E-mail: Mersoned@gmail.com

<sup>1</sup>ORCID: <https://orcid.org/0000-0002-7063-088X>

<sup>2</sup>ORCID: <https://orcid.org/0000-0002-0570-2584>

<sup>3</sup>ORCID: <https://orcid.org/0000-0002-7530-9518>

<sup>4</sup>ORCID: <https://orcid.org/0000-0001-5006-4115>

*Поступила в редакцию 19.09.2022*

*Принята к публикации 31.10.2022*

**Аннотация:** Существует устойчивое мнение, что водород, поглощаемый магниевыми сплавами в процессе коррозии, может вызывать их коррозионное растрескивание под напряжением. Одним из характерных признаков участия диффузионно-подвижного водорода в механизме разрушения металлов является отрицательная скоростная зависимость степени охрупчивания. В недавних исследованиях было показано, что потеря пластичности образцов сплава ZK60, подвергнутых кратковременному (1,5 ч) воздействию коррозионной среды, действительно уменьшается с ростом скорости деформации. Однако после удаления продуктов коррозии с поверхности образцов скоростная зависимость потери пластичности становится положительной, что свидетельствует об отсутствии водорода в объеме металла. При кратковременной выдержке в коррозионной среде глубокое проникновение водорода в металл могло быть ограничено недостаточным для диффузии водорода временем. В работе исследовано механическое поведение сплава ZK60, подвергнутого более длительной (12 ч) предварительной выдержке в коррозионной среде с последующим испытанием на растяжение в атмосфере воздуха при различных скоростях деформации. Рассмотрено влияние скорости деформирования, длительной выдержки в коррозионной среде и последующего удаления продуктов коррозии на прочность, пластичность, стадии деформационного упрочнения и локализованной деформации, а также на состояние боковой поверхности и изломов образцов. Установлено, что потеря пластичности образцов, выдержанных в течение 12 ч в коррозионной среде, уменьшается с ростом скорости деформирования независимо от того, были удалены продукты коррозии с их поверхности или нет. Показано, что в данном случае отрицательная скоростная зависимость потери пластичности связана не с водородом, растворенным в объеме металла, а с наличием глубоких коррозионных повреждений поверхности образцов. Предложено объяснение влияния коррозионных повреждений на механические свойства и чувствительность этих свойств к изменению скорости деформации.

**Ключевые слова:** магниевые сплавы; сплав ZK60; коррозионное растрескивание под напряжением; коррозия; скорость деформации; механические свойства.

**Благодарности:** Исследование выполнено при финансовой поддержке РФФ в рамках научного проекта № 18-19-00592.

**Для цитирования:** Мерсон Е.Д., Полуянов В.А., Мягких П.Н., Мерсон Д.Л. Скоростная чувствительность механических свойств сплава ZK60 с высокой степенью коррозионных повреждений // Frontier Materials & Technologies. 2023. № 1. С. 45–55. DOI: 10.18323/2782-4039-2023-1-45-55.



# Statistical dependences of influence of ultrasonic exposure time on the strength and other parameters of a polypropylene welded joint

© 2023

*Sergey V. Murashkin*<sup>1</sup>, PhD (Engineering),  
assistant professor of Chair “Nanotechnologies, Materials Science, and Mechanics”  
*Aleksandr S. Selivanov*\*<sup>2</sup>, PhD (Engineering), Director of the Institute of Mechanical Engineering  
*Nikolay G. Spiridonov*<sup>3</sup>, postgraduate student,  
assistant of Chair “Nanotechnologies, Materials Science, and Mechanics”  
*Elena B. Savina*<sup>4</sup>, master

Togliatti State University, Togliatti (Russia)

\*E-mail: selivas@inbox.ru

<sup>1</sup>ORCID: <https://orcid.org/0000-0002-9613-7313>

<sup>2</sup>ORCID: <https://orcid.org/0000-0001-5267-0629>

<sup>3</sup>ORCID: <https://orcid.org/0000-0003-2283-0104>

<sup>4</sup>ORCID: <https://orcid.org/0000-0002-6312-6431>

Received 30.06.2022

Accepted 21.03.2023

**Abstract:** Polypropylene is one of the most popular thermoplastic materials used in industry. To produce goods from this material, the ultrasonic welding method is often used. However, despite a large number of scientific papers, the influence of some parameters of the ultrasonic welding mode on the strength characteristics of polypropylene joints remains unstudied. The paper presents the results of experimental studies of contact spot ultrasonic welding of plates 3 mm thick made of 01003-26 grade polypropylene. The authors considered the process of gradual penetration of the ultrasonic tool working face into polypropylene to a depth equal to the total thickness of the welded plates. Statistical dependences of the depth of the tool face penetration into the material and the force of material separation on the ultrasound exposure time are obtained. The influence of the depth of the ultrasonic tool working face penetration on the tearing force of welded specimens is determined. A significant increase in the tearing force from 150 to 400 N was found at the tool penetration depth of more than 3.5 mm due to an increase in the nominal area of mutual mixing of the material between the welded plates caused by the flow of molten material into the gap. The authors proposed a hypothesis about the flow of the molten material in the direction opposite to the direction of penetration of the working tool by forming traveling Rayleigh waves. However, its confirmation requires additional studies of the influence of the ultrasonic welding mode parameters and the size of the gap between the parts to be joined on the rate of the molten material flow into the gap.

**Keywords:** ultrasonic welding of plastics; polypropylene; welded joint strength; welding tool working part; ultrasonic welding time; depth of penetration of an ultrasonic tool face.

**For citation:** Murashkin S.V., Selivanov A.S., Spiridonov N.G., Savina E.B. Statistical dependences of influence of ultrasonic exposure time on the strength and other parameters of a polypropylene welded joint. *Frontier Materials & Technologies*, 2023, no. 1, pp. 57–67. DOI: 10.18323/2782-4039-2023-1-57-67.

## INTRODUCTION

Today, various polymeric materials begin actively to displace metals due to some of their technical and economic indicators. First of all, this refers to significant corrosion resistance, high mechanical properties at a relatively low density and lower cost than that of metals and alloys [1; 2]. According to the scale of production, among thermoplastic polymeric materials, which are characterized by the ability to pass when heated to a viscous and then liquid state, polyolefins occupy the leading place. This group includes low-density and high-density polyethylene, polypropylene, etc. In terms of the production growth rates, these materials surpass all other polymeric materials, and at present, polyethylene ranks first in world production, and polypropylene is the fourth [3]. The mass use of polyolefins for manufacturing various products involves the improvement of technological processes for their joining. Ultrasonic welding of polymeric materials remains one of the most popular methods for joining parts when assembling products and building structures [4; 5].

However, due to the complexity of ultrasonic equipment and ignorance of the influence of various welding mode parameters and additional factors (welding time, welding force, substrate material, soaking time, energy concentrator shape, etc.) on the strength characteristics of a resulting joint, manufacturers of plastic goods made of polypropylene and polyethylene encounter the problems of determining the ultrasonic welding optimal modes, which would provide the required strength indicators of a finished product.

The studies presented in [6] are aimed at searching for optimal modes of ultrasonic welding of polypropylene. The authors emphasize the influence of variable welding parameters, namely, welding time, soaking time, and vibration amplitude, on the strength characteristics of H110MA grade polypropylene specimens. Based on the results of the experiments, the optimal values of technological variables were determined to ensure maximum tearing strength: the welding time – 1200 ms, the soaking time – 900 ms, and the vibration amplitude – 75 %.

In [7], the optimal modes for ultrasonic welding of polypropylene filled with 10 % glass fiber were found.

The results of the experiments showed that the maximum breaking force of about 2.3 kN is achieved with a welding force of 1.5 bar, a vibration amplitude of 32 microns, and a welding time of 0.4 s.

The authors of [8] investigate the influence of the amplitude and welding time on the strength characteristics of polypropylene, arguing that they are the most important parameters of the weld joint strength. Ultrasonic welding of the specimens was performed using a pyramidal energy concentrator, which made it possible to ensure the welded joint shear strength equal to 22.36 MPa (319 % of the initial strength).

The authors of [9] state that it is the shape of the energy concentrator that has the greatest effect on the strength of the joint, and the pyramidal energy concentrator allows obtaining the most durable joint made of pure polypropylene.

In the work [10], the authors state that the main factors affecting the strength of a welded joint made of polypropylene are the welding time and the welding force. According to the results of the experiments, it was found that the welding time of less than 2 s and the welding force of less than 2 N do not provide a monolithic joint, and the welding time of 8 s and the welding force of 8 N lead to the formation of pores and defects in the weld. The optimal modes for ultrasonic welding of polypropylene specimens with a thickness of 4 mm are: the welding time is 4–6 s, the welding force is 5–7 N.

The authors [11] believe that the level of deterioration in the mechanical and thermal properties of polypropylene goods after ultrasonic welding depends on the change in the crystalline structure, glass transition temperature, and the weight loss, since polypropylene undergoes crystal reorientations during melting. As a result, a phase is formed that has an intermediate crystalline order and differs from the normal phase. After welding polypropylene, the glass transition temperatures tend to change from 5 to 10 K/min.

Studies allowing a more detailed understanding of the degree of impact of ultrasonic vibrations on the polypropylene structure are presented in [12]. The authors identified that after ultrasonic welding, the strength of welded joints after 300–600 h of aging reaches 90–100 % of the base material strength. However, significant strength instability is observed, which can be traced even on one product, when the strength of various sections of a weld ranges from 50 to 100 % of the base material strength. It is explained by complex wave processes during the ultrasound propagation in welded plastic parts, which leads to an uneven change in the structure of the weld material [13].

A more detailed analysis of the effect of ultrasonic vibrations on the formation of a polypropylene welded joint using modern techniques, such as differential scanning calorimetry, thermogravimetric analysis, Fourier transform infrared spectroscopy, and scanning electron microscopy, was carried out in [14]. The analysis of the degree of stretching of samples after ultrasonic welding allowed concluding that an increase in the main parameters of the process (pressure, time, and vibration amplitude) leads to an increase in the strength of the weld, to the contrary, a decrease in plasticity was noted. Using scanning electron microscopy, the authors revealed the formation

of voids, which is closely correlated with the amplitude of vibrations.

The works [15–17] present evidence that the strength of a welded joint during ultrasonic welding directly depends on the amount of melt located between the contact surfaces. In this case, the amount of melt is determined by a whole complex of ultrasonic welding modes and depends on the amplitude and frequency of vibrations, welding force, the depth of the coupler end face penetration into the material, the time of exposure to ultrasound, and other parameters [18].

Based on the analysis of scientific publications, it can be concluded that the influence of welding time, vibration amplitude, welding force, energy concentrator geometry on the strength characteristics of polypropylene samples and the structure of the resulting weld is well studied in the literature. All these factors directly determine the amount of melt formed between the parts during the welding process. However, the amount of melt in the gap is also influenced by the working tool end face penetration depth, which directly depends on the time of exposure to ultrasound. This issue has not been addressed in the scientific literature.

The study aims at the improvement of the strength of polypropylene welded joints obtained in the process of ultrasonic welding by adjusting the time of exposure to ultrasound on the welding zone and the depth of penetration of the welding coupler end face into polypropylene.

## METHODS

Ultrasonic welding of samples was carried out using a technological complex for ultrasonic welding of plastics consisting of a welding device and an UZG-2M ultrasonic generator. The device for ultrasonic welding consists of an ultrasonic vibrating system (USVS) placed inside a metal case. The ultrasonic vibrating system contains a magnetostriction converter of electrical energy into the energy of mechanical extension vibrations and an ultrasonic coupler rigidly connected to the end face of the converter. The ultrasonic coupler working part has the form of a cylindrical rod with a flat end 5 mm in diameter.

The ultrasonic welding technological complex was installed on an FHV-50PD universal milling machine using specially designed equipment. The equipment includes:

- a device for orienting and fixing sample plates during ultrasonic welding, made in the form of a prism with a square base, on the upper end of which there are two mutually perpendicular slots-lodgments for sample plates;
- a unit for fastening the USW device to the quill of the machine is a bracket with two terminal clamps for clamping the quill and USW device, respectively;
- a device for creating a constant static pressure of the ultrasonic coupler working end face on the welding zone includes a calibrated load mounted to the steering wheel of the lever-rack mechanism of the machine spindle head;
- a device for measuring the pressing force of the ultrasonic coupler working end face to the contact surface of the sample plates consists of a 7039-2023 spring according to the ГОСТ 13165-1967 standard and a rectangular prism with a blind cylindrical hole located in the center of one of its faces.

During calibration, the spring was installed in the prism hole until it stops. The result of the calibration is a straight line equation

$$\Delta(F) = b \cdot F, \quad (1)$$

where  $\Delta(F)$  – is the dependence of deformation on the force of compression of the spring;

$b$  – is the proportionality coefficient,  $b=0.122$  mm/N;

$F$  – is the spring compression force, N.

Rectangular plates cut from 01003-26 sheet polypropylene 3 mm thick according to the ГОСТ 26996-1986 standard were used as samples (Fig. 1).

Contact spot ultrasonic overlap welding of samples was carried out according to the scheme shown in Fig. 2.

The welding cycle consisted of sequential execution of the following actions:

- applying a constant static pressure  $P_{st}$  equal to  $1.32 \pm 0.10$  MPa, which corresponds to a spring compression force  $F$  equal to  $26 \pm 2$  N;

- exposure for 3 s for pre-compression of sample plates under pressure  $P_{st}$ ;

- turning on the ultrasonic vibrations (without relieving pressure);

- switching off the ultrasonic vibrations after a time  $t_i = 1.2 \dots 3.6$  s;

- exposure of the welded joint sample under a pressure  $P_{st}$  for 3 s;

- removal of static pressure  $P_{st}$ .

The static pressure  $P_{st}$  is applied before the ultrasonic vibrations are turned on (the pre-compression time  $t_p$  is 3 s), it is considered constant throughout the entire welding cycle and is removed with a delay of  $t_d$ . The delay time is 3 s. The time of exposure to ultrasound  $t_i$  varies from 1.2 to 3.6 s.

Before the first cycle and every 15 USW cycles, the spring compression deformation was measured and, using the equation (1), the pressing force value was calculated, which was controlled within the specified limits of  $26 \pm 2$  N.

Sample plates having glossy (with low roughness) flat surfaces on both sides (Fig. 1) were installed in the corresponding lodgments (Fig. 3), evenly fixed and pressed together with screws.

The USW mode: generator output power is  $330 \pm 10$  W, amplitude and frequency of vibrations are  $67 \pm 3$   $\mu\text{m}$  and  $21915 \pm 5$  Hz, respectively; the force of pressing the welding tool (WT) working end face to the samples was applied in the direction perpendicular to their joint plane and was maintained within the range of  $26 \pm 2$  N using a calibrated load mounted to the steering wheel of the lever-rack mechanism of the machine spindle head. After each completed cycle, the WT surface temperature was controlled by immersing it for two minutes in a container with cold water, then blown with compressed air at a temperature of  $22 \pm 2$  °C and wiped with a napkin. The time of ultrasound exposure to the welding zone was set according to the generator timer in the range of 1.2...3.6 s with a step of 0.2 s. At each time value, five experiments were performed (five welded joint samples were created). The joint samples were marked with Arabic numerals as they were created (Fig. 3) and prepared for measuring the depth of coupler working end face penetration into polypropylene.

The depth of ultrasonic coupler penetration into the material was measured using a stand equipped with measuring heads of the C-IV ГОСТ 10197-1970 type according to the scheme (Fig. 4). The welded joint thickness  $H$  was measured with an ABSOLUTE Digimatic 547-401 thickness gauge having a measurement range from 0 to 12 mm, a resolution of 1  $\mu\text{m}$ , and a precision of  $\pm 3$   $\mu\text{m}$ .

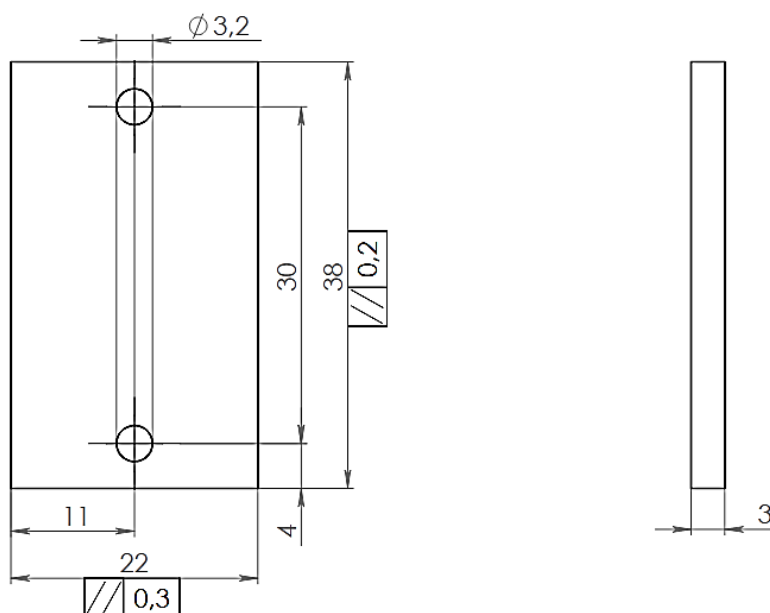
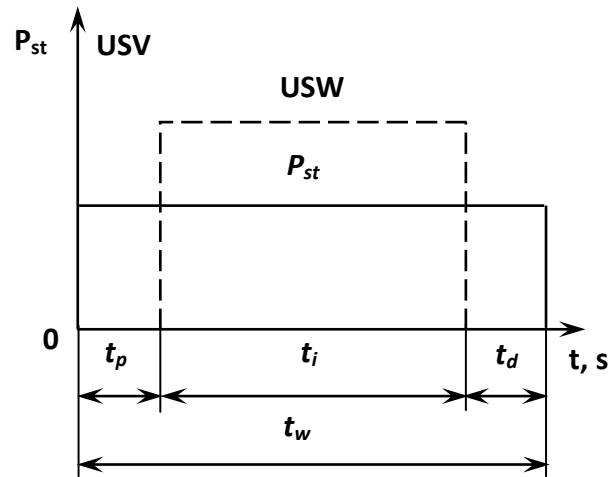


Fig. 1. A sample plate  
Рис. 1. Образец-пластина



**Fig. 2.** “Static pressure – ultrasound” USW working cycle:

$P_{st}$  – static pressure; USV – the ultrasonic vibrations;  $t_p$  – the time of preliminary pressing of samples;  $t_i$  – the ultrasonic vibration exposure time;  $t_d$  – the static pressure-off delay time;  $t_w$  – the welding time

**Рис. 2.** Рабочий цикл УЗС «статическое давление – ультразвук»:

$P_{st}$  – статическое давление; USV – ультразвуковые колебания;  $t_p$  – время предварительного сжатия образцов;  $t_i$  – время воздействия УЗК;  $t_d$  – время задержки снятия статического давления;  $t_w$  – время сварки

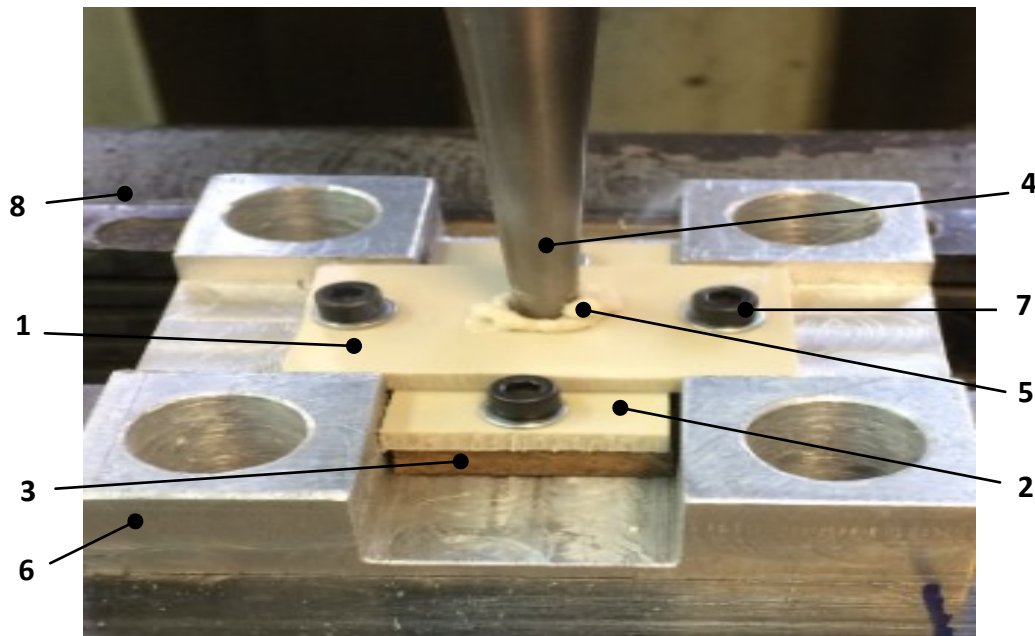


**Fig. 3.** The creation of a sample of a polypropylene welded joint on a milling machine:

1 and 2 – the upper and lower plates-samples respectively; 3 – the heat insulating substrate; 4 – the welding tool; 5 – the overlap of a pressed-out melt;

6 – the lodgments’ prism; 7 – screws and washers for sample fixation; 8 – the machine-tool clamps

**Рис. 3.** Создание образца сварного соединения полипропилена на фрезерном станке:

1 и 2 – верхний и нижний образцы-пластины соответственно; 3 – термоизоляционная подкладка;

4 – сварочный инструмент; 5 – наплыв выдавленного расплава;

6 – призма ложементов; 7 – винты и шайбы для крепления образцов; 8 – тиски станочные

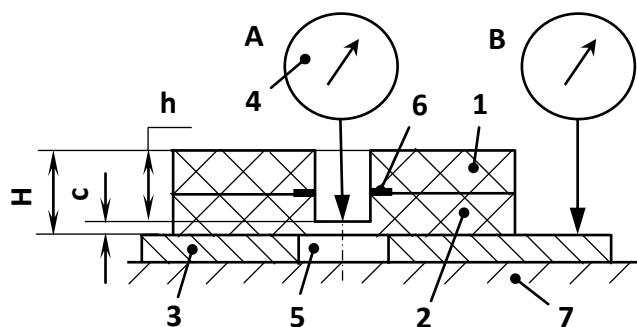


**Fig. 4.** The scheme for measuring the thickness of the “bottom” using a C-IV type stand:  
1 and 2 – the upper and lower welded joint plates respectively; 3 – the metal plane-parallel plate;  
4 – ICh-10 type detecting head rigidly fixed on the C-IV type stand; 5 – a hole in the plate;

6 – a welded joint; 7 – the support table of the C-IV type stand;  
H – total thickness of the plates in a welded joint; h – the depth of WT working face penetration; c – the “bottom” thickness;  
A – measurement location; B – the location of “zero” setting

**Рис. 4.** Схема измерения толщины «дна» при помощи стойки типа C-IV:

1 и 2 – верхняя и нижняя пластины сварного соединения соответственно;

3 – металлическая плоскопараллельная пластина;

4 – индикаторная головка типа ИЧ-10, жестко закрепленная на стойке типа C-IV; 5 – отверстие в пластине;

6 – сварной шов; 7 – опорный столик стойки типа C-IV; H – общая толщина пластин в сварном соединении;

h – глубина внедрения рабочего торца СИ; c – толщина «дна»; A – положение измерения; B – положение установки «нуля»

The depth of coupler penetration into the material was determined by the formula (Fig. 4)

$$h = H - c,$$

where  $h$  – is the depth of WT working end face penetration into polypropylene, mm;

$H$  – is the total thickness of the plates included in a welded joint, mm;

$c$  – is the “bottom” thickness, mm.

The welded specimens were tested for tensile strength in accordance with the ГОСТ Р 55142-2012 standard after their holding for 24 h to complete the material polymerization process. The tests were performed on an Instron (USA) 5966 model tensile-testing machine equipped with a force sensor with a measurement range of 10 kN and a measurement tolerance of  $\pm 0.5\%$ . The testing was carried out in the following sequence:

- the tested samples were conditioned for at least 4 h according to the ГОСТ 12423-2013 standard at a temperature of  $(23 \pm 2)^\circ\text{C}$  and relative humidity  $(50 \pm 5)\%$ ;

- a welded joint sample was fixed in the device (Fig. 5) and installed in the testing machine so that the upper and lower clamping plates were pressed by the jaws of the machine corresponding clamps;

- the sample was loaded with a tensile force in the direction perpendicular to the joint plane of the welded joint plates, at a speed of 1 mm/min until the plates were completely separated from each other;

- the maximum force applied to destruct the welded joint sample was recorded;

- the type of destruction was determined according to the ГОСТ Р 58121.3-2018 standard.

Statistical processing of the measurement results was performed according to the ГОСТ 14359-1969 standard

using the STATISTICA software. The MATHCAD software was used to approximate the experimental results and obtain analytical dependencies.

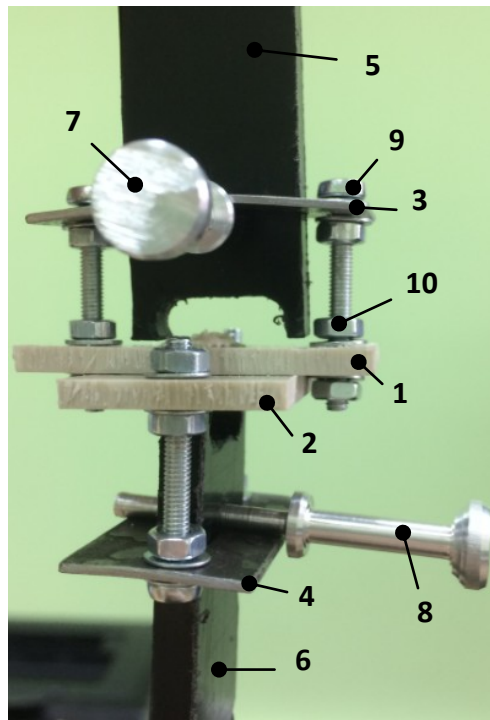
## RESULTS

Fig. 6 presents the results of experimental studies of the dependence of the depth of ultrasonic tool end face penetration and the material tearing force on the time of exposure to ultrasound. As follows from the figure, the depth of tool end face penetration is proportional to the time of ultrasound exposure to the welded materials and is determined mainly by the time of melting the material and its displacement under the action of the feed force of the ultrasonic tool. The dependence of the tearing force of the material on the time of exposure to ultrasound has a different nature and is not linear.

Fig. 7 presents a graph constructed according to the experimental values in the “tearing force” – “tool penetration depth” coordinates. As follows from the analysis of the graph, when the tool penetration depth changes to 3.5 mm, the material tearing force changes rather smoothly from 50 to 150 N. With a tool penetration depth of more than 3.5 mm, a significant increase in the tearing force from 150 to 400 N is observed.

During the tests, the authors noted that the deformation in the direction of application of tensile forces increases to the yield point, then almost immediately the destruction of the welded joint occurs. Fig. 8 shows the appearance and the state of the welded joint samples during loading by the tensile force at the moments of its maximum and minimum values. From the figure, it can be observed that at the moment of applying the maximum force, the plates were strongly bent (Fig. 8 a).

The weld is deformed, and with the formation of the neck, the joint is destroyed. The type of fracture is



**Fig. 5.** A device for fixing a welded joint sample on a tensile testing machine:

1 and 2 – the upper and lower welded joint plates respectively;  
 3 and 4 – the upper and lower bearing metal plates; 5 and 6 – the upper and lower locking plates;  
 7 and 8 – the support pins; 9 – the adjusting screw; 10 – the anchor nuts

**Рис. 5.** Приспособление для крепления образца сварного соединения на разрывную машину:

1 и 2 – верхняя и нижняя пластины сварного соединения соответственно;  
 3 и 4 – верхняя и нижняя опорные металлические пластины;  
 5 и 6 – верхняя и нижняя зажимные пластины;  
 7 и 8 – опорные пальцы; 9 – регулировочный винт; 10 – крепежные гайки

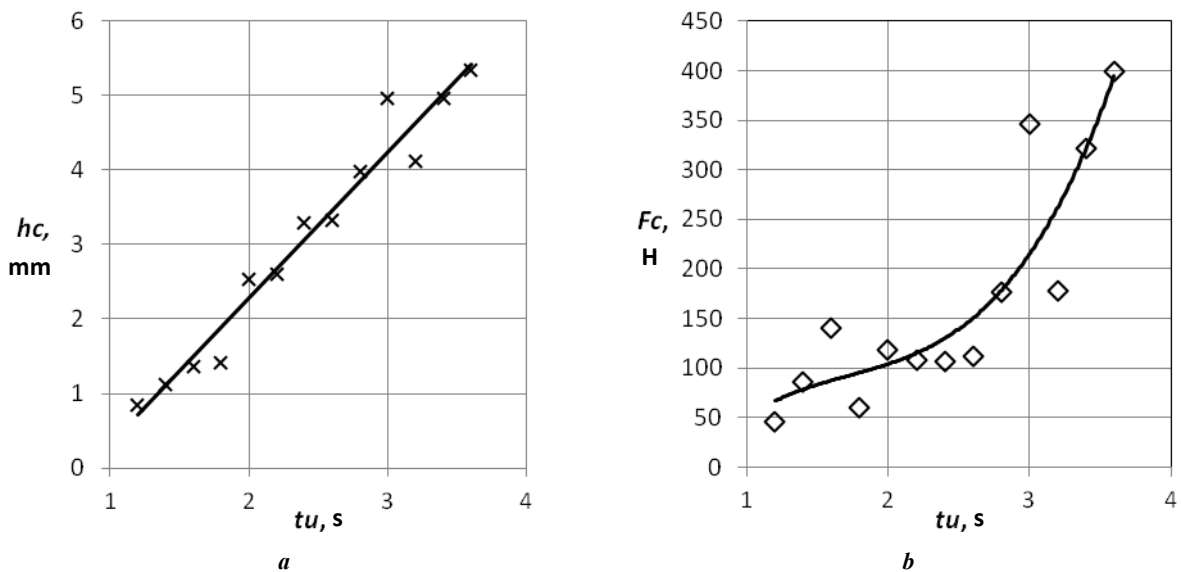


**Fig. 6.** Experimental values and approximating them graphical dependences of the depth of tool face penetration into the material (a) and the force of material separation (b) on the ultrasound exposure time

**Рис. 6.** Экспериментальные значения и аппроксимирующие их графические зависимости глубины внедрения торца инструмента в материал (a) и усилия отрыва материала (b) от времени воздействия ультразвука

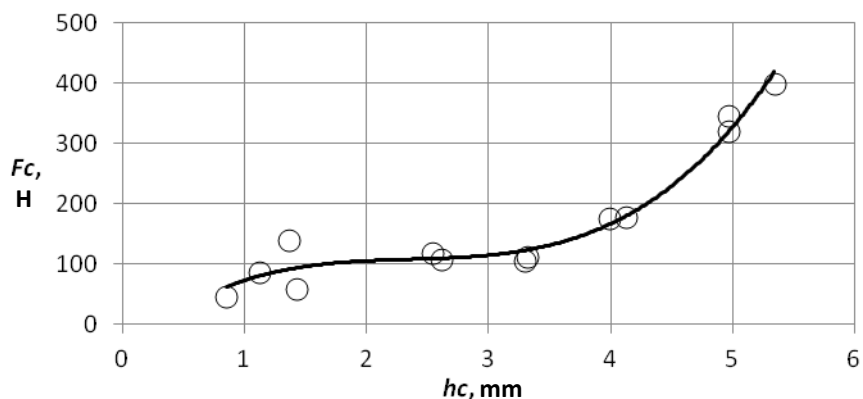


**Fig. 7.** Experimental values and approximating them graphical dependence of the force of material separation on the depth of tool face penetration into the material during ultrasonic welding  
**Рис. 7.** Экспериментальные значения и аппроксимирующая их графическая зависимость усилия отрыва материала от глубины внедрения торца инструмента в материал при ультразвуковой сварке

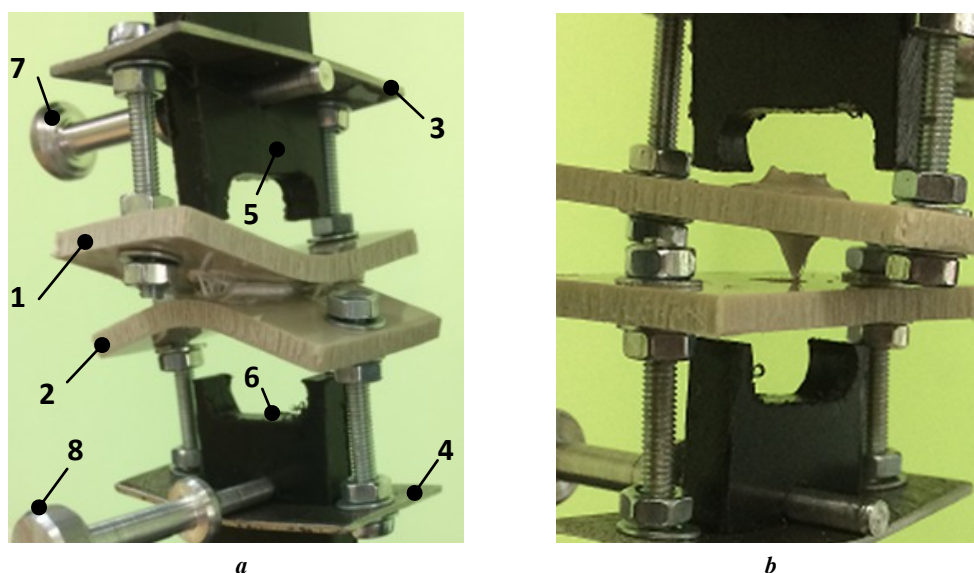


**Fig. 8.** The state of the sample during testing:  
**a** – at the moment of maximum force tearing the welded joint plates from each other; **b** – at the moment of tearing off.  
 In the figure: 1 and 2 – the upper and lower welded joint plates respectively; 3 and 4 – the upper and lower bearing metal plates;  
 5 and 6 – the upper and lower locking plates; 7 and 8 – the support pins

**Рис. 8.** Состояние образца при испытании:  
**a** – в момент максимальной силы, отрывающей пластины сварного соединения друг от друга; **b** – в момент отрыва.  
 На рисунке: 1 и 2 – верхняя и нижняя пластины сварного соединения соответственно;  
 3 и 4 – верхняя и нижняя опорные металлические пластины; 5 и 6 – верхняя и нижняя зажимные пластины; 7 и 8 – опорные пальцы

plastic over the entire separation surface. After separation, the tensile force disappears, the bending deformations are removed, and the plates return to their initial position (Fig. 8 b).

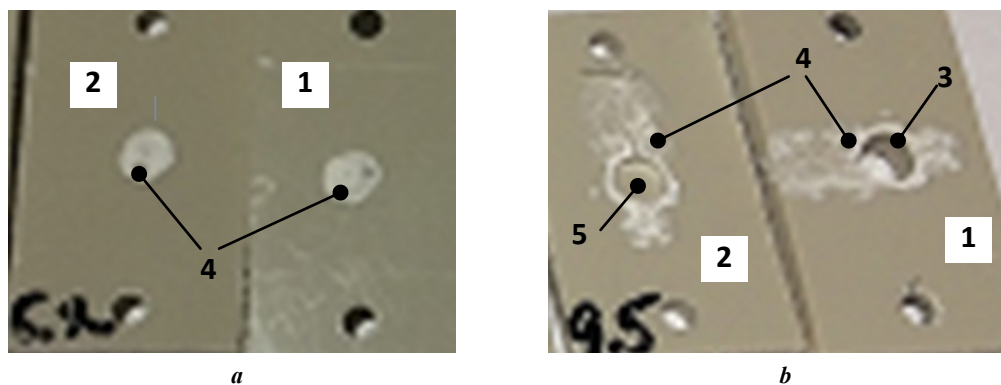
The three-dimensional surface, along which the destruction of the welded joint occurs as a result of the separation of the plates from each other, visually represents a group of many pimples and dimples of arbitrary shape and size.

Fig. 9 shows the appearance of the welded joint fracture surfaces for samples when the tool face penetration depth does not exceed the plate thickness (Fig. 9 a) and when it exceeds (Fig. 9 b). In the first case, the tool end face penetration depth is 2.64 mm, the tearing force was 146.80 N,

and the fracture surface is limited by a circle with a diameter almost equal to the WT end face diameter. In the second case, the tool end face penetration depth was 3.93 mm, the tearing force was 233.68 N, and the fracture surface diameter was much larger. Fig. 9 b shows traces of the melt flow even beyond the plate.

## DISCUSSION

The analysis of the results states that with an increase in the exposure time, an increase in the tearing force occurs which is caused by an increase in the nominal area



**Fig. 9.** Typical view of the welded joint fracture surface after separation of the plates from each other:

**a** – welded joint sample No. 6.2 ( $t_f=2.2$  s;  $h=2.64$  mm;  $F=146.80$  N);

**b** – welded joint sample No. 9.5 ( $t_f=2.8$  s;  $h=3.93$  mm;  $F=233.68$  N).

In the figure: 1 and 2 – the upper and lower welded joint plates respectively;

3 – the surface of a through hole formed as a result of WT face penetration to a depth of 3.93 mm;

4 – joint fracture surfaces; 5 – a dimple in the form of a recess hole

**Рис. 9.** Характерный вид поверхности разрыва сварного соединения после отрыва пластин друг от друга:

**a** – образец сварного соединения № 6.2 ( $t_f=2,2$  с;  $h=2,64$  мм;  $F=146,80$  Н);

**b** – образец сварного соединения № 9.5 ( $t_f=2,8$  с;  $h=3,93$  мм;  $F=233,68$  Н).

На рисунке: 1 и 2 – верхняя и нижняя пластины сварного соединения соответственно;

3 – поверхность сквозного отверстия, образовавшегося в результате внедрения торца СИ на глубину 3,93 мм;

4 – поверхности разрыва соединения; 5 – углубление в виде глухого отверстия

of material intermixing. This increase in the strength of welded joints was noted in many works [15–17], however, in them, an increase in the amount of melt occurs due to the application of energy concentrators of various shapes and sizes, which increase the roughness of the surfaces to be joined [18; 19].

In our case, ultrasonic welding of polypropylene plates with a flat glossy contact surface having a low roughness was performed. Taking into account that the thickness of the welded samples was 3 mm, and the tool penetration depth was more than 5 mm, i.e., above the interface between the samples, the increase in the intermixing area, and, accordingly, in the tearing force, can only be associated with the flow of molten material into the gap between the contact surfaces of the specimens to be joined during welding.

Although polypropylene is a polycrystalline material, it is very soft and capable of forming a mechanical surface joint even at poor melting [20]. This provides good adhesion of the molten material in the gap between the surfaces of the plates, and, consequently, an increase in the tearing force. On this basis, it would be very useful to carry out a similar experiment using other materials, for example, an amorphous material such as polystyrene and a harder polycrystalline material such as polyphenylene sulfide.

Moreover, the work did not study the effect of the size of the gap between the parts to be joined on the amount and distribution of the material melt flowing into it, which is of practical interest from the point of view of assembling parts before ultrasonic welding.

The flow of molten polypropylene up the working tool walls in the direction opposite to the direction of its penetration, and the material flow into the gap between the plates being joined, is apparently associated with a decrease in the friction force due to high-frequency vibrations, which contribute to the formation of surface traveling Ray-

leigh waves. The observed phenomenon can be applied in practice for ultrasonic welding of polypropylene products without using the energy concentrators, which will simplify the design of the parts to be joined, and, consequently the methods of their production. However, this issue requires a more detailed study and determination of quantitative dependences of the material flow rate on the amplitude, vibration frequency, and other ultrasound parameters.

## MAIN RESULTS

1. The dependence of the ultrasonic tool end face penetration depth is directly proportional to the time of exposure to ultrasound when welding polypropylene.

2. The dependence of the tearing force of the welded joint of materials welded by ultrasonic with overlap on the time of ultrasound exposure is non-linear and increases sharply when a certain time of ultrasound exposure is reached.

3. With an increase in the depth of the tool end face penetration to the interface between the plates, the strength of a welded joint gradually increases, and beyond the interface, the strength growth rate increases.

4. The welded joint strength increases with an increase in the amount of melt located between the contacting surfaces of the plates.

## REFERENCES

1. Volkov S.S., Maloletkov A.V., Kobernik N.V. Peculiarities of formation of welded joints in ultrasonic welding of plastics. *Svarochnoe proizvodstvo*, 2018, no. 2, pp. 50–55. EDN: [MIEUZE](#).
2. Volkov S.S., Remizov A.L., Shestel L.A. Developing systems for automatic control of the process of ultrasonic welding of plastic materials. *Izvestiya vysshikh*

- uchebnykh zavedeniy. Mashinostroenie*, 2017, no. 12, pp. 376–440. DOI: [10.18698/0536-1044-2017-12-37-44](https://doi.org/10.18698/0536-1044-2017-12-37-44).
3. Komarov G.V. New progress in the field of welding polymeric materials. *Polimernye materialy*, 2017, no. 9, pp. 44–49.
  4. Unnikrishnan T.G., Kavan P. A review study in ultrasonic-welding of similar and dissimilar thermoplastic polymers and its composites. *Materials Today: Proceedings*, 2022, vol. 56, no. 6, pp. 3294–3300. DOI: [10.1016/j.matpr.2021.09.540](https://doi.org/10.1016/j.matpr.2021.09.540).
  5. Komarov G.V. Some trends in welding polymeric materials. *Polimernye materialy*, 2018, no. 9, pp. 56–59.
  6. Rajput Ch., Kumari S., Prajapati V., Dinbandhu, Abhishek K. Experimental investigation on peel strength during ultrasonic welding of polypropylene H110MA. *Materials Today: Proceedings*, 2020, vol. 26, no. 2, pp. 1302–1305. DOI: [10.1016/j.matpr.2020.02.259](https://doi.org/10.1016/j.matpr.2020.02.259).
  7. Nikoi R., Sheikhi M.M., Arab N.B.M. Experimental analysis of effects of ultrasonic welding on weld strength of polypropylene composite samples. *International Journal of Engineering*, 2015, vol. 28, no. 3, pp. 447–453.
  8. Raza S.F., Khan S.A., Mughal M.P. Optimizing the weld factors affecting ultrasonic welding of thermoplastics. *The International Journal of Advanced Manufacturing Technology*, 2019, vol. 103, pp. 2053–2067. DOI: [10.1007/s00170-019-03681-7](https://doi.org/10.1007/s00170-019-03681-7).
  9. Liu S.-J., Chang I.-T., Hung S.-W. Factors affecting the joint strength of ultrasonically welded polypropylene composites. *Polymer Composites*, 2004, vol. 22, no. 1, pp. 132–141. DOI: [10.1002/pc.10525](https://doi.org/10.1002/pc.10525).
  10. Fu X., Yuan X., Li G., Wu Y., Tong H., Kang S., Luo J., Pan Z., Lu W. A study on ultrasonic welding of thermoplastics with significant differences in physical properties under different process parameters. *Materials Today Communications*, 2022, vol. 33, article number 105009. DOI: [10.1016/j.matcom.2022.105009](https://doi.org/10.1016/j.matcom.2022.105009).
  11. Chinnadurai T., Prabaharan N., Mohan Raj N., Pandian M.K. Ultrasonically welded and non-welded polypropylene and PC-ABS blend thermal analysis. *Journal of Thermal Analysis and Calorimetry*, 2018, vol. 132, pp. 1813–1824. DOI: [10.1007/s10973-018-7052-y](https://doi.org/10.1007/s10973-018-7052-y).
  12. Mozgovoy I.V., Nelin A.G., Davidan G.M., Mozgovoy E.I., Mozgovoy O.I. The study of the effect of energy fields on polypropylene. *Omskiy nauchnyy vestnik*, 2006, no. 10, pp. 76–84. EDN: [HGKGXS](https://www.edn.ru/HGKGXS).
  13. Chinnadurai T., Arungalai Vendan S., Rusu C.C., Scutelnicu E. Experimental investigations on the polypropylene behavior during ultrasonic welding. *Materials and Manufacturing Processes*, 2018, vol. 33, no. 7, pp. 718–726. DOI: [10.1080/10426914.2017.1303155](https://doi.org/10.1080/10426914.2017.1303155).
  14. Tao W., Su X., Wang H., Zhang Z., Li H., Chen J. Influence mechanism of welding time and energy director to the thermoplastic composite joints by ultrasonic welding. *Journal of Manufacturing Processes*, 2019, vol. 37, pp. 196–202. DOI: [10.1016/j.jmapro.2018.11.002](https://doi.org/10.1016/j.jmapro.2018.11.002).
  15. Zhao T., Broek Ch., Palardy G., Fernandez Villegas I., Benedictus R. Towards robust sequential ultrasonic spot welding of thermoplastic composites: Welding process control strategy for consistent weld quality. *Composites Part A: Applied Science and Manufacturing*, 2018, vol. 109, pp. 355–367. DOI: [10.1016/j.compositesa.2018.03.024](https://doi.org/10.1016/j.compositesa.2018.03.024).
  16. Volkov S.S., Nerovnyy V.M., Shestel L.A. The Effect of Thermal Energy Concentration on the Strength of Welded Surfaces in the Ultrasonic Welding of Plastics. *Izvestiya vysshikh uchebnykh zavedeniy. Mashinostroenie*, 2018, no. 1, pp. 63–70. DOI: [10.18698/0536-1044-2018-1-63-70](https://doi.org/10.18698/0536-1044-2018-1-63-70).
  17. Klubovich V.V., Klushin V.A., Khrushchev E.V., Marusich V.I. The study of ultrasonic welding of polymers. *Metallurgiya mashinostroeniya*, 2017, no. 5, pp. 31–40. EDN: [XFGRXL](https://www.edn.ru/XFGRXL).
  18. Volkov S.S., Prilutskiy M.A. The influence of the roughness of the welded surfaces on the quality of the weld when using ultrasonic welding of heterogeneous plastic materials. *Izvestiya vysshikh uchebnykh zavedeniy. Mashinostroenie*, 2016, no. 2, pp. 53–58. EDN: [VKQDNV](https://www.edn.ru/VKQDNV).
  19. Marcus M., Wenning J., Parsons J., Savitski A. Comparative analysis of energy director styles on polybutylene terephthalate with servo-driven ultrasonic welder. *SPE ANTEC Indianapolis*. USA, JW Marriott Indianapolis Publ., 2016, pp. 1266–1273.
  20. Marcus M., Cohn H., Drechsler J., Grodek D., Savitski A. Development of an approach to determine minimum amplitude required for ultrasonic welding. *SPE ANTEC Indianapolis*. USA, JW Marriott Indianapolis Publ., 2017, pp. 39–44.

#### СПИСОК ЛИТЕРАТУРЫ

1. Волков С.С., Малолетков А.В., Коберник Н.В. Особенности образования сварных соединений при ультразвуковой сварке пластмасс // Сварочное производство. 2018. № 2. С. 50–55. EDN: [MIEUZF](https://www.edn.ru/MIEUZF).
2. Волков С.С., Ремизов А.Л., Шестель Л.А. Разработка систем автоматического управления процессом ультразвуковой сварки пластмасс // Известия высших учебных заведений. Машиностроение. 2017. № 12. С. 376–440. DOI: [10.18698/0536-1044-2017-12-37-44](https://doi.org/10.18698/0536-1044-2017-12-37-44).
3. Комаров Г.В. Новые достижения в области сварки полимерных материалов // Полимерные материалы. 2017. № 9. С. 44–49.
4. Unnikrishnan T.G., Kavan P. A review study in ultrasonic-welding of similar and dissimilar thermoplastic polymers and its composites // Materials Today: Proceedings. 2022. Vol. 56. № 6. P. 3294–3300. DOI: [10.1016/j.matpr.2021.09.540](https://doi.org/10.1016/j.matpr.2021.09.540).
5. Комаров Г.В. Некоторые тенденции в сварке полимерных материалов // Полимерные материалы. 2018. № 9. С. 56–59.
6. Rajput Ch., Kumari S., Prajapati V., Dinbandhu, Abhishek K. Experimental investigation on peel strength during ultrasonic welding of polypropylene H110MA // Materials Today: Proceedings. 2020. Vol. 26. № 2. P. 1302–1305. DOI: [10.1016/j.matpr.2020.02.259](https://doi.org/10.1016/j.matpr.2020.02.259).
7. Nikoi R., Sheikhi M.M., Arab N.B.M. Experimental analysis of effects of ultrasonic welding on weld strength of polypropylene composite samples // International Journal of Engineering. 2015. Vol. 28. № 3. P. 447–453.
8. Raza S.F., Khan S.A., Mughal M.P. Optimizing the weld factors affecting ultrasonic welding of thermoplastics // The International Journal of Advanced Manufacturing Technology. 2019. Vol. 103. P. 2053–2067. DOI: [10.1007/s00170-019-03681-7](https://doi.org/10.1007/s00170-019-03681-7).

9. Liu S.-J., Chang I.-T., Hung S.-W. Factors affecting the joint strength of ultrasonically welded polypropylene composites // *Polymer Composites*. 2004. Vol. 22. № 1. P. 132–141. DOI: [10.1002/pc.10525](https://doi.org/10.1002/pc.10525).
10. Fu X., Yuan X., Li G., Wu Y., Tong H., Kang S., Luo J., Pan Z., Lu W. A study on ultrasonic welding of thermoplastics with significant differences in physical properties under different process parameters // *Materials Today Communications*. 2022. Vol. 33. Article number 105009. DOI: [10.1016/j.mtcomm.2022.105009](https://doi.org/10.1016/j.mtcomm.2022.105009).
11. Chinnadurai T., Prabaharan N., Mohan Raj N., Pandian M.K. Ultrasonically welded and non-welded polypropylene and PC-ABS blend thermal analysis // *Journal of Thermal Analysis and Calorimetry*. 2018. Vol. 132. P. 1813–1824. DOI: [10.1007/s10973-018-7052-y](https://doi.org/10.1007/s10973-018-7052-y).
12. Мозговой И.В., Нелин А.Г., Давидан Г.М., Мозговой Е.И., Мозговой О.И. Исследование воздействия энергетических полей на полиэтилен // *Омский научный вестник*. 2006. № 10. С. 76–84. EDN: [HGKGSX](https://www.edn.ru/HGKGSX).
13. Chinnadurai T., Arungalai Vendan S., Rusu C.C., Scutelnicu E. Experimental investigations on the polypropylene behavior during ultrasonic welding // *Materials and Manufacturing Processes*. 2018. Vol. 33. № 7. P. 718–726. DOI: [10.1080/10426914.2017.1303155](https://doi.org/10.1080/10426914.2017.1303155).
14. Tao W., Su X., Wang H., Zhang Z., Li H., Chen J. Influence mechanism of welding time and energy director to the thermoplastic composite joints by ultrasonic welding // *Journal of Manufacturing Processes*. 2019. Vol. 37. P. 196–202. DOI: [10.1016/j.jmapro.2018.11.002](https://doi.org/10.1016/j.jmapro.2018.11.002).
15. Zhao T., Broek Ch., Palardy G., Fernandez Villegas I., Benedictus R. Towards robust sequential ultrasonic spot welding of thermoplastic composites: Welding process control strategy for consistent weld quality // *Composites Part A: Applied Science and Manufacturing*. 2018. Vol. 109. P. 355–367. DOI: [10.1016/j.compositesa.2018.03.024](https://doi.org/10.1016/j.compositesa.2018.03.024).
16. Волков С.С., Неровный В.М., Шестель Л.А. Влияние концентрации тепловой энергии на прочность поверхностей при ультразвуковой сварке пластмасс // *Известия высших учебных заведений. Машиностроение*. 2018. № 1. С. 63–70. DOI: [10.18698/0536-1044-2018-1-63-70](https://doi.org/10.18698/0536-1044-2018-1-63-70).
17. Клубович В.В., Клушин В.А., Хрущев Е.В., Марусич В.И. Исследование ультразвуковой сварки полимеров // *Металлургия машиностроения*. 2017. № 5. С. 31–40. EDN: [XFGRXL](https://www.edn.ru/XFGRXL).
18. Волков С.С., Прилуцкий М.А. Влияние шероховатости свариваемых поверхностей на качество их соединения при ультразвуковой сварке разнородных пластмасс // *Известия высших учебных заведений. Машиностроение*. 2016. № 2. С. 53–58. EDN: [VKQDNV](https://www.edn.ru/VKQDNV).
19. Marcus M., Wenning J., Parsons J., Savitski A. Comparative analysis of energy director styles on polybutylene terephthalate with servo-driven ultrasonic welder // *SPE ANTEC Indianapolis, USA: JW Marriott Indianapolis*, 2016. P. 1266–1273.
20. Marcus M., Cohn H., Drechsler J., Grodek D., Savitski A. Development of an approach to determine minimum amplitude required for ultrasonic welding // *SPE ANTEC Indianapolis, USA: JW Marriott Indianapolis*, 2017. P. 39–44.

## Статистические зависимости влияния времени воздействия ультразвука на прочность и другие параметры сварного соединения полипропилена

© 2023

*Мурашкин Сергей Викторович*<sup>1</sup>, кандидат технических наук,  
доцент кафедры «Нанотехнологии, материаловедение и механика»  
*Селиванов Александр Сергеевич*<sup>\*2</sup>, кандидат технических наук,  
директор института машиностроения  
*Спиридонов Николай Германович*<sup>3</sup>, аспирант,  
ассистент кафедры «Нанотехнологии, материаловедение и механика»  
*Савина Елена Борисовна*<sup>4</sup>, магистр

*Тольяттинский государственный университет, Тольятти (Россия)*

\*E-mail: [selivas@inbox.ru](mailto:selivas@inbox.ru)

<sup>1</sup>ORCID: <https://orcid.org/0000-0002-9613-7313>

<sup>2</sup>ORCID: <https://orcid.org/0000-0001-5267-0629>

<sup>3</sup>ORCID: <https://orcid.org/0000-0003-2283-0104>

<sup>4</sup>ORCID: <https://orcid.org/0000-0002-6312-6431>

*Поступила в редакцию 30.06.2022*

*Принята к публикации 21.03.2023*

**Аннотация:** Полипропилен является одним из наиболее востребованных термопластичных материалов, применяемых в промышленности. Для изготовления изделий из данного материала зачастую применяется способ ультразвуковой сварки. Однако, несмотря на большое количество научных работ, влияние некоторых параметров режима ультразвуковой сварки на прочностные характеристики соединений полипропилена остается неизученным. В работе представлены результаты экспериментальных исследований контактной точечной ультразвуковой сварки пластин толщиной 3 мм из полипропилена марки 01003-26. Рассмотрен процесс постепенного внедрения рабочего торца ультразвукового инструмента в полипропилен до глубины, равной общей толщине свариваемых пластин. Получены статистические зависимости глубины внедрения торца инструмента в материал и усилия отрыва материала от времени воздействия ультразвука. Определено влияние глубины внедрения рабочего торца ультразвукового инструмента на усилие отрыва сваренных образцов. Обнаружено значительное увеличение усилия отрыва с 150 до 400 Н при глубине внедрения инструмента свыше 3,5 мм, обусловленное ростом номинальной

площади взаимного перемешивания материала между свариваемыми пластинами, вызванного затеканием расплавленного материала в зазор. Предложена гипотеза о течении расплавленного материала в сторону, противоположную направлению внедрения рабочего инструмента, путем формирования бегущих волн Релея. Однако ее подтверждение требует проведения дополнительных исследований влияния параметров режима ультразвуковой сварки и величины зазора между соединяемыми деталями на скорость затекания расплавленного материала в зазор.

**Ключевые слова:** ультразвуковая сварка пластмасс; полипропилен; прочность сварного соединения; рабочая часть сварочного инструмента; время ультразвуковой сварки; глубина внедрения торца ультразвукового инструмента.

**Для цитирования:** Мурашкин С.В., Селиванов А.С., Спиридонов Н.Г., Савина Е.Б. Статистические зависимости влияния времени воздействия ультразвука на прочность и другие параметры сварного соединения полипропилена // Frontier Materials & Technologies. 2023. № 1. С. 57–67. DOI: 10.18323/2782-4039-2023-1-57-67.



## Fatigue strength of 30XГСА–40ХМФА welded joints produced by rotary friction welding

© 2023

**Elena Yu. Priymak**\*<sup>1,2,4</sup>, PhD (Engineering), Head of the Laboratory of Metal Science and Heat Treatment, assistant professor of Chair of Materials Science and Technology of Materials

**Elena A. Kuzmina**<sup>1</sup>, Head of Technical Department

**Sergey V. Gladkovskii**<sup>3,5</sup>, Doctor of Sciences (Engineering), chief researcher

**Dmitry I. Vichuzhanin**<sup>3,6</sup>, PhD (Engineering), senior researcher

**Valeria E. Veselova**<sup>3,7</sup>, junior researcher

<sup>1</sup>ZBO Drill Industries, Inc., Orenburg (Russia)

<sup>2</sup>Orenburg State University, Orenburg (Russia)

<sup>3</sup>Institute of Engineering Science of Ural Branch of the Russian Academy of Sciences, Yekaterinburg (Russia)

\*E-mail: elena-pijmak@yandex.ru

<sup>4</sup>ORCID: <https://orcid.org/0000-0002-4571-2410>

<sup>5</sup>ORCID: <https://orcid.org/0000-0002-3542-6242>

<sup>6</sup>ORCID: <https://orcid.org/0000-0002-6508-6859>

<sup>7</sup>ORCID: <https://orcid.org/0000-0002-4955-6435>

Received 02.11.2022

Accepted 16.02.2023

**Abstract:** Rotary friction welding (RFW) is used in the production of drill pipes for solid mineral prospecting. The need for the creation of the lightened drill strings for high-speed diamond drilling of ultradeep wells dictates the necessity of a greater focus on the study of a weld zone and setting the RFW technological parameters. This paper presents the results of experimental studies of a welded joint of a drill pipe of the H standard size according to ISO 10097, made of the 30XГСА (pipe body) and 40ХМФА (tool joint) steels under the cyclic loads. The authors evaluated the influence of the force applied to the workpieces in the process of friction of the contacting surfaces (force during heating), and postweld tempering at a temperature of 550 °C on the cyclic life of welded joints, under the conditions of alternate tension-compression at the cycle amplitude stress of  $\pm 420$  MPa. The study determined that with an increase in the force during heating, the microstructure changes occur in the zone of thermomechanical influence, contributing to an increase in the fatigue strength of welded joints. The authors identified the negative effect of postweld tempering on the fatigue strength of welded joints, which is expressed in the decrease in the number of cycles before failure by 15–40 %, depending on the magnitude of the force during heating. The optimal RFW mode of the specified combination of steels is determined, which provides the largest number of cycles before failure: the force during heating (at friction)  $F_h=120$  kN, forging force  $F_{for}=160$  kN, rotational frequency during heating  $n=800$  Rpm, and upset during heating  $l=8$  mm. A series of fatigue tests have been carried out at various values of the cycle amplitude stress of the welded joint produced at the optimal mode and the 30XГСА steel base metal; limited endurance curves have been plotted. It is shown that the differences in the limited endurance curves of the pipe body material (30XГСА steel) and the welded joint are insignificant. The obtained results are supplemented by the microhardness measurement data and fractographs of fractured samples, revealing the mechanism of crack propagation under the cyclic loads.

**Keywords:** rotary friction welding; drill pipes; welded joint; fatigue strength; limited endurance curve; 30XГСА steel; 40ХМФА steel.

**Acknowledgments:** The reported study was funded by RFBR according to the research project No. 20-38-90032.

To perform mechanical tests, the equipment of the “Plastometry” Core Facility Center of Institute of Engineering Science of the UB RAS was used.

**For citation:** Priymak E.Yu., Kuzmina E.A., Gladkovskii S.V., Vichuzhanin D.I., Veselova V.E. Fatigue strength of 30XГСА–40ХМФА welded joints produced by rotary friction welding. *Frontier Materials & Technologies*, 2023, no. 1, pp. 69–81. DOI: 10.18323/2782-4039-2023-1-69-81.

### INTRODUCTION

Rotary friction welding (RFW) refers to the process of producing welded joints of parts that are rotary bodies. It has a number of technological advantages compared to other types of welding and allows welding partially weldable and difficult-to-weld materials in various combinations, which determines its application in various industries. This technology is used when producing drill pipes with welded tool joints for the oil and mining industry, during geological

exploration for solid minerals. At the same time, the exaggeration of mining and geological drilling conditions associated with a greater depth of rock occurrence, determines the necessity to create lightened drill pipe structures by reducing the wall thickness of the drill pipe body when using a stronger pipe billet. Considering that the drill string during high-speed diamond drilling operates under difficult mechanical loading conditions, a more careful approach is required to the choice of materials and the setting of welding modes.

As a rule, drill pipes are a welded structure of a tool joint with a pipe body made of medium- and low-carbon alloy steels connected by RFW<sup>1</sup>. As a pipe body for lightened constructions of drill pipes, it is supposed to use a pipe billet made of 30XГCA steel, which after quenching and tempering, ensures the required properties: constrained yield strength  $\geq 750$  MPa, ultimate tensile strength  $\geq 850$  MPa, and elongation  $\geq 12$  %. As a material for the drill pipe tool joint, various grades of medium-carbon alloy steels can be used, which after quenching and tempering, ensure the following mechanical properties: constrained yield strength  $\geq 930$  MPa, ultimate tensile strength  $\geq 1050$  MPa, and relative elongation  $\geq 10$  %. 40XMΦA steel is the most widely used.

The search and analysis of works aimed at the detailed study of the microstructure and properties of friction welded joints made of medium-carbon alloy steels showed the insufficient information in this area. There are some publications presenting the results of the studies of the microstructure and properties of welded joints of drill pipes made of N80 steels (analogue to 35Г2) in the normalized state with 42CrMo4 steel (analogue to 40XM) after quenching and tempering [1], AISI 8630 steel (analogue to 30XMH) [2], and welded joints of ASTM A 106 Grade B steel (analogue to 20Г) in the hot-rolled state and 4140 steel (analogue to 40XГM) after normalization and after toughening [3; 4]. These works, as well as other studies [5; 6] indicate that the mechanical properties of welded joints during tensile tests with properly selected welding modes meet or, in some cases, even exceed the mechanical properties of the weakest welded material. However, the working conditions of drill pipes during operation are determined by the impact of both the static and sign-variable cyclic loads. Therefore, the study of the fatigue strength of the RFW-produced joints of drill pipe elements is important to assess the reliability and performance of the structure.

It is known that the fatigue properties of welded joints, including those RFW-produced, are determined both by the chemical composition of welded materials and the microstructural features of the welded joint zone and the level of residual welding stresses [7; 8]. In this case, welded joints performed by the friction welding methods have higher fatigue strength characteristics than welded joints produced by fusion welding [9–11]. In the work [12], it was established that a higher endurance limit of a welded joint compared to the base material can be obtained by friction welding of stainless steels. However, when welding dissimilar steels, such as medium-carbon steel and austenitic stainless steel, the fatigue strength of a welded joint decreased by 30 % compared to medium-carbon steel and by 40 % compared to austenitic steel [13]. During friction welding of AISI 1040 medium-carbon steel (analogue to 40Г), the fatigue strength of a welded joint is close to the fatigue strength of the base metal of this steel [14]. However, the fatigue strength of a welded joint in the combination of 32G2 and 40HN steels is inferior to the fatigue strength of 32G2 steel by up to 30 % [15].

At the same time, welding parameters and post-weld heat treatment affect the microstructure and properties of welded joints, which is shown in publications using the examples of both the joints of medium-carbon steels [16; 17] and combinations of low-carbon steel with stainless steel [18] and aluminium alloy [19], as well as other alloys [20] and their combinations [21].

The need to create lightened structures of geological exploration drill pipes dictates the necessity to study the fatigue properties when changing the modes of welding and post-weld heat treatment also in a welded joint of 30XГCA and 40XMΦA steels intended for use, which has not been studied by now. It is necessary to understand the degree of strength uniformity of the weld zone with the drill pipe body (30XГCA steel).

Early studies of mentioned combination of steels identified the optimal range of RFW parameters, which provides maximum tensile strength at their interface (at the joint): heating force  $F_h=40\text{--}120$  kN, forging force  $F_{\text{for}}=100\text{--}160$  kN, rotational speed during heating  $n=700\text{--}900$  Rpm, and upset during heating  $l=-7\text{--}9$  mm [22]. However, the obtained values of optimal parameters show that the range of force values during heating ensuring a high-quality welded joint in the junction of materials, is rather wide, therefore, a more detailed assessment of the influence of this parameter on the fatigue strength of a joint containing all microstructural zones formed during welding is of interest.

The work is aimed at evaluating the influence of the parameters of rotary friction welding and post-weld tempering on the fatigue resistance of welded joints of 30XГCA and 40XMΦA steels, and determining the optimal parameters ensuring the maximum degree of strength uniformity of the weld zone with the base material – 30XГCA steel.

## METHODS

Friction welding was performed on pipe billets with a diameter of 92 mm and a wall thickness of 8 mm made of 40XMΦA steel and pipe billets with a diameter of 89 mm and a wall thickness of 4 mm (H standard size according to ISO 10097) made of 30XГCA steel previously quenched and high-tempered.

Chemical composition of the original steels is shown in Table 1.

Welding was carried out on the Thompson-60 equipment complete with a software package that allows setting and controlling welding parameters. The RFW process consists of the stage of heating the billets during friction as a result of applying an axial force on the side of the rotating workpiece, and the forging stage, which consists of applying an additional axial force after the rotation stops. Thus, the main RFW parameters are the force during heating, (during friction as a result of the contact of two rotating pipes),  $F_h$  (kN), the forging force  $F_{\text{for}}$  (kN), the rotational speed during heating  $n$  (Rpm), and the upset during heating  $l$  (mm) [23].

Welding modes selected for current study are shown in Table 2.

The mechanical properties of welded joints and the base metal are shown in Table 3. It also contains the mechanical properties of welded joints after tempering in a laboratory furnace at a temperature of 550 °C during 1 hour.

<sup>1</sup>ГОСТ P 51245–99. General-purpose steel drill pipes. General technical specifications. M.: Publishing House of Standards, 1999. 15 p.

Fatigue tests of the samples were carried out on the INSTRON 8801 universal testing machine according to the alternate tension-compression scheme with a cycle asymmetry coefficient  $R=-1$ , and a loading frequency of 5 Hz. The standard size of samples for fatigue tests of the base metal and welded joints is shown in Fig. 1. In this case, the sample shape corresponded to type III according to the ГОСТ 25.509-79 standards and the dimensions were adjusted to ensure its stability under alternating cyclic loading at the increased loads.

In the course of testing the samples of welded joints produced under various welding modes, in the initial state and after tempering, the number of cycles to failure was determined at a stress amplitude of  $\sigma_a=\pm 420$  MPa. Three samples per mode were subjected to tests followed by the calculation of the average value of cyclic durability. After determining the optimal mode that ensures the maximum durability of welded specimens. Tests were carried out at various stresses both for welded specimens under the selected mode, and monolithic specimens made of 30XГСА steel for the construction of limited endurance curves and their comparative evaluation.

The study of the microstructure of welded joints was carried out on transverse microslices after etching with a 4 % solution of nitric acid in ethanol using an Olympus DSX1000 optical microscope. The microhardness was measured along the length of the thermomechanical effect zone (TMEZ), with a step of 0.5 mm according to the ГОСТ 9450-76 standard on a HVS-1000 microhardness tester, applying a load of 2 N for 10 s. The fractographic analysis of the destroyed samples was carried out on a Tescan VEGA II XMU scanning electron microscope.

## RESULTS

A typical macro- and microstructure of a welded joint of 30XГСА and 40XMΦА steels after rotary friction welding is shown in Fig. 2. Directly near the joint zone, it is martensite with the bainite areas. In the TMEZ peripheral areas, a finely-dispersed ferrite-carbide microstructure is observed as a result of a decrease in temperature exposure.

Microhardness distribution across the width of TMEZ in the initial state after welding and tempering is shown in Fig. 3.

Near the zone of joining two steels, there are areas with high microhardness in relation to the base metal caused by the formation of martensite structures (Fig. 3 a). The force during heating has some influence both on the microhardness values and the TMEZ length. With an increase in the force during heating in the range from 40 kN (mode No. 1) to 120 kN (mode No. 3), the TMEZ length decreases from 7.85 to 5.25 mm. The maximum values of microhardness are observed in the samples obtained with a heating force of 120 kN and amount 669 HV 0.2 for 40XMΦА steel and 608 HV 0.2 for 30XГСА steel. The minimum HV 0.2 values correspond to the peripheral TMEZ areas in the welded joint produced with the lowest force during heating of 40 kN. In these areas, the microhardness of 30XГСА steel is 264–280 HV 0.2, the one of 40XMΦА steel is 298–335 HV 0.2, while the microhardness of the base metal of 30XГСА steel reaches 294–306 HV 0.2, and the one of 40XMΦА steel is 362–367 HV 0.2. Thus, the most weakened zone in this welded joint (mode No. 1) in relation to all its areas, is the peripheral area of the 30XГСА steel TMEZ.

**Table 1.** Chemical composition of steels intended for the production of drill pipes, % by weight  
*Таблица 1.* Химический состав сталей, предназначенных для производства буровых труб, % по масс.

Steel Grade	C	Mn	Si	S	P	Cr	Ni	Cu	Mo	V
30XГСА pipe body	0.33	1.02	1.12	0.003	0.011	0.99	–	0.04	–	–
40XMΦА tool joint	0.41	0.48	0.27	0.004	0.008	0.97	0.08	0.06	0.27	0.11

**Table 2.** Rotary friction welding modes selected for the experiment  
*Таблица 2.* Режимы ротационной сварки трением, выбранные для эксперимента

Mode No.	Force during heating $F_h$ , kN	Forging force $F_{for}$ , kN	Upset during heating $l$ , mm	Rotational speed $n$ , Rpm
1	40	160	8	800
2	80			
3	120			

**Table 3.** Mechanical properties of the RFW-produced welded joints of the 30XГСА and 40ХМФА steels and base materials\*  
**Таблица 3.** Механические свойства сварных соединений сталей 30XГСА и 40ХМФА, выполненных ротационной сваркой трением, и материалов основы\*

Test sample	RFW mode No.	$\sigma_{0,2}$ , МПа	$\sigma_B$ , МПа	$\delta$ , %	$\psi$ , %
Welded joint	1	760/758**	849/841	8.0/7.0	34.5/33.5
	2	757/755	883/851	10.0/9.0	33.0/33.5
	3	771/768	894/882	10.5/10.5	35.0/36.0
30XГСА	–	767	888	13.0	36.5
40ХМФА	–	1111	1205	10.5	38.0

\* Mechanical properties are obtained for the samples with the working part length of 50 mm, width of 15 mm, and thickness of 4 mm at the INSTRON 8801 test unit according to the GOST 6996-66 and GOST 1497-84 standards.

\*\* In the numerator, mechanical properties of a welded joint after rotary friction welding are indicated; in the denominator – the ones after tempering.

\* Механические свойства получены на образцах с длиной рабочей части 50 мм, шириной 15 мм и толщиной 4 мм на испытательной установке INSTRON 8801 в соответствии с ГОСТ 6996-66 и ГОСТ 1497-84.

\*\* В числителе приведены механические свойства сварного соединения после ротационной сварки трением, а в знаменателе – после отпуска.

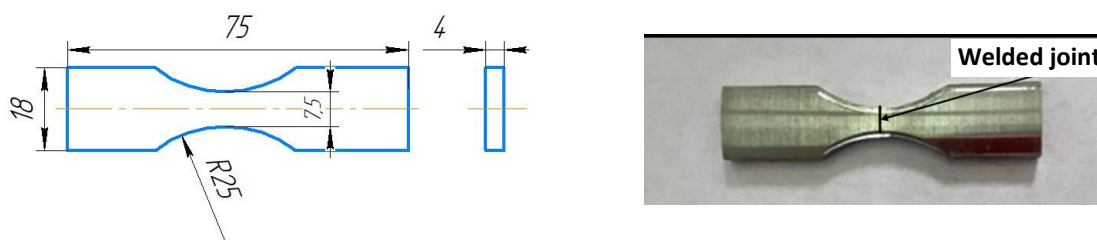


**Fig. 1.** A sample with a welded joint for fatigue tests  
**Рис. 1.** Образец со сварным соединением для испытаний на усталость

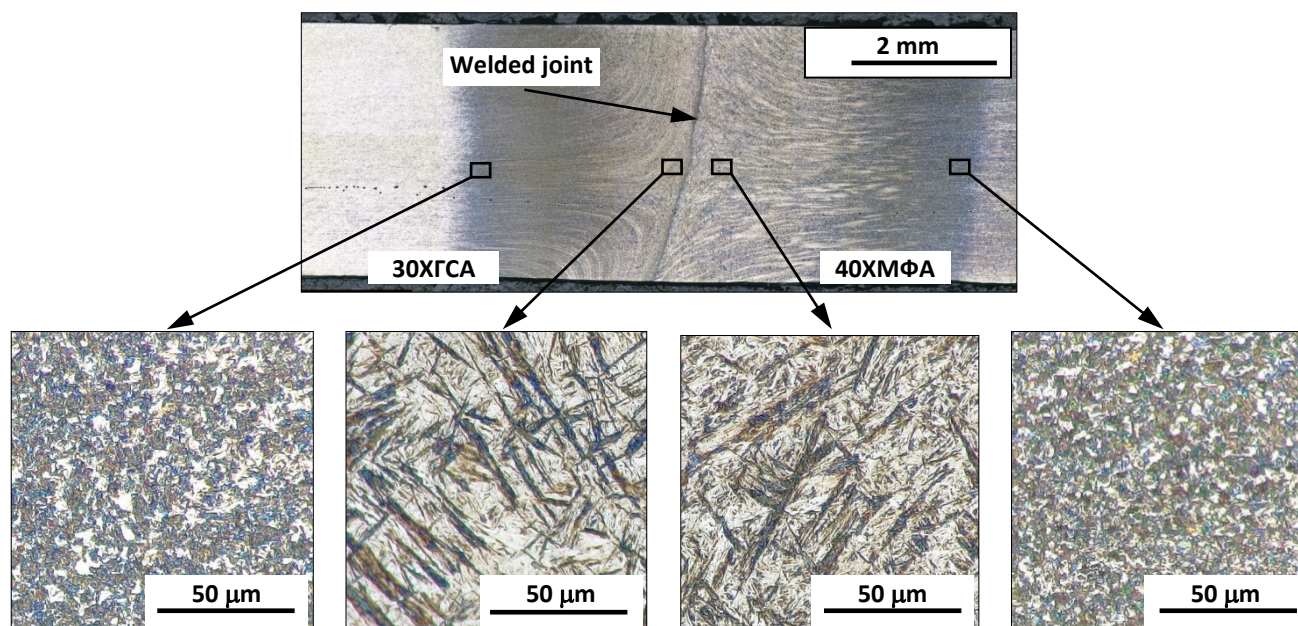


**Fig. 2.** Macro- and microstructure of a welded joint of the 30XГСА and 40ХМФА steels produced by rotary friction welding (mode No. 2)

**Рис. 2.** Макро- и микроструктура сварного соединения сталей 30XГСА и 40ХМФА, полученная ротационной сваркой трением (режим № 2)

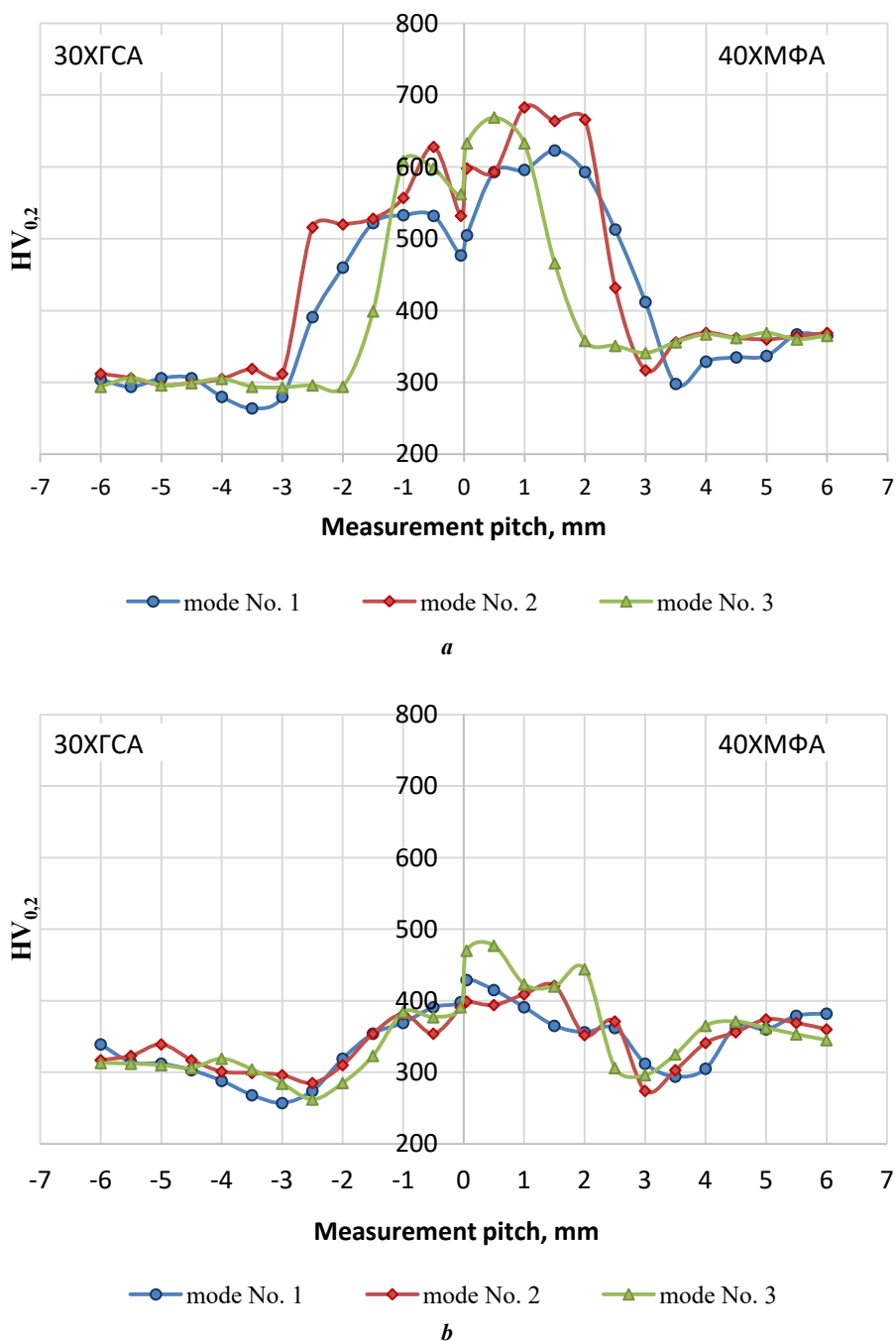


**Fig. 3.** Microhardness distribution in welded joints of the 30XГСА–40XМФА steels: *a* – after friction welding; *b* – after friction welding and further tempering at 550 °C  
**Рис. 3.** Распределение микротвердости в сварных соединениях сталей 30XГСА–40XМФА: *a* – после сварки трением; *b* – после сварки трением и последующего отпуска при 550 °C

Post-weld tempering caused a decrease in microhardness in the thermomechanical effect zone in all samples and, as a result, a partial elimination of the mechanical inhomogeneity typical for the initial state of a welded joint. However, it should be noted that in the welded joints, performed according to modes No. 2 and No. 3, in the peripheral TMEZ areas, the microhardness in the initial state was at the base metal level, and local weakening of these areas with respect to the base metal is observed after tempering. In the welded joint, obtained according to mode No. 1, in the weakening zone formed earlier during

welding, an additional decrease in microhardness is observed (Fig. 3 b).

Fig. 4 shows the number of cycles before failure of samples of welded joints during fatigue testing.

The obtained results (Fig. 4) show that with an increase in the force during heating, the durability of the samples increases. At the same time, tempering reduces the number of cycles to failure by 40, 20, and 15 % after the implementation of modes No. 1, No. 2, and No. 3, respectively.

During the tests, the failure of all samples was recorded from the side of 30XГСА steel at a distance of 3 to 5 mm

from the junction of two steels. Fig. 5 shows the appearance of tested samples.

Fig. 6, 7 demonstrate the macro- and microstructure of fractures of tested samples.

The fracture surface of all tested samples is a typical fatigue fracture, where the zone of the fatigue crack initiation and development (area 1), as well as the fracture zone (area 2) are observed (Fig. 6 and 7). The fatigue zone in all samples of welded joints is from 65 to 75 %, which indicates a high resistance of the material to crack propagation. In this case, the fatigue crack initiation occurred from the surface of the samples on the inner part of the pipe billet.

The fatigue fracture zones of samples produced with the force during heating equal to 40 kN (mode No. 1) at  $\sigma_a=420$  MPa with and without tempering have a plateau-like fracture surface with the fragments of a grooved microrelief (Fig. 6 b, 6 e). The tempered sample has a smoother microrelief (Fig. 6 e). However, the distance between the fatigue grooves is higher, which indicates

a higher crack propagation rate in this sample. The fracture zones of both samples (Fig. 6 c, 6 f) are of the viscous type and contain small and shallow viscous pits.

The fractures of samples of welded joints produced with the force during heating equal to 80 kN (mode No. 2) had an identical structure to that described above in the initial state and after tempering. However, samples obtained with the force during heating equal to 120 kN (mode No. 3), both with subsequent tempering (Fig. 7 e) and without it (Fig. 7 b), are characterized by a smoother microrelief without evident fatigue grooves. Taking into account the fact that the total TMEZ length at this welding mode is 5.25 mm, the failure of the sample, most likely, occurred in the zone of the base metal of 30XГСА steel (Fig. 5). In the fracture of the samples, pores are observed, which were probably initiated by the non-metallic inclusions in the original billet. The fracture zones of both samples (Fig. 7 c, 7 f), as well as in the previous samples, are characterized by the viscous shallow-pitted microrelief.

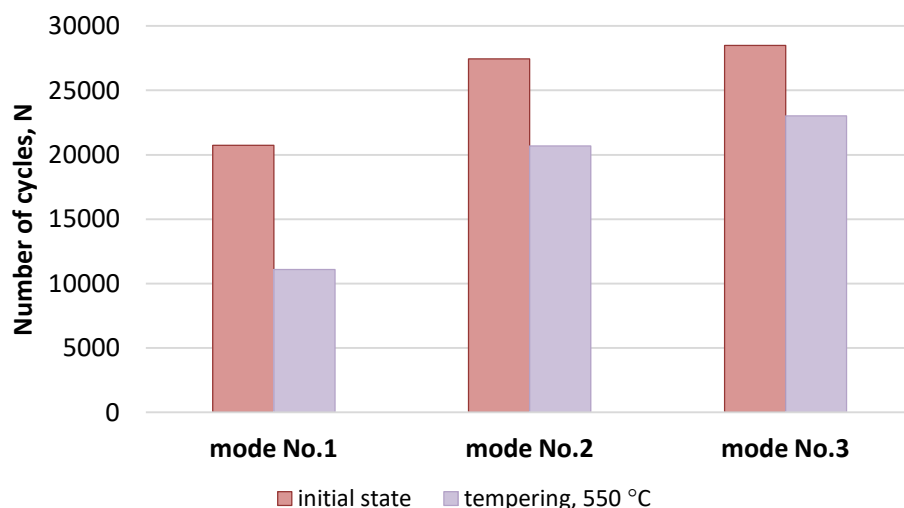


**Fig. 4.** The number of cycles before failure of samples of welded joints of the 30XГСА–40ХМФА steels in the initial state and after tempering during cyclic tests with an amplitude of  $\sigma_a=\pm 420$  MPa

**Рис. 4.** Количество циклов до разрушения образцов сварных соединений сталей 30XГСА–40ХМФА в исходном состоянии и после отпуска при циклических испытаниях с амплитудой  $\sigma_a=\pm 420$  МПа

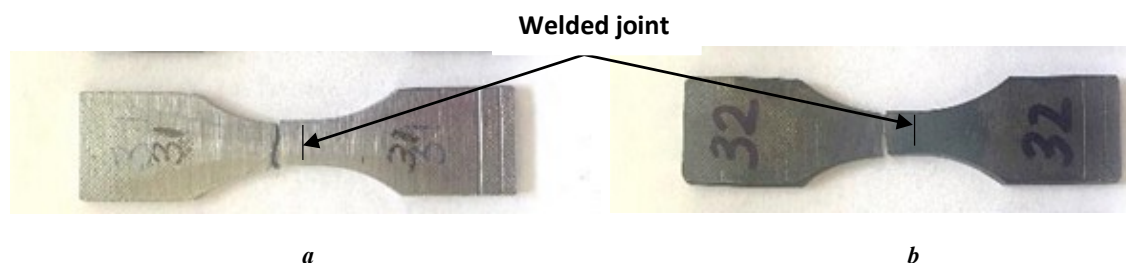


**Fig. 5.** The appearance of broken specimens after cyclic tests (at the left – 30XГСА steel):

**a** – mode No. 3 after welding; **b** – mode No. 3 after tempering

**Рис. 5.** Внешний вид разрушенных образцов после циклических испытаний (слева сталь 30XГСА):

**a** – режим № 3 после сварки; **b** – режим № 3 после отпуска

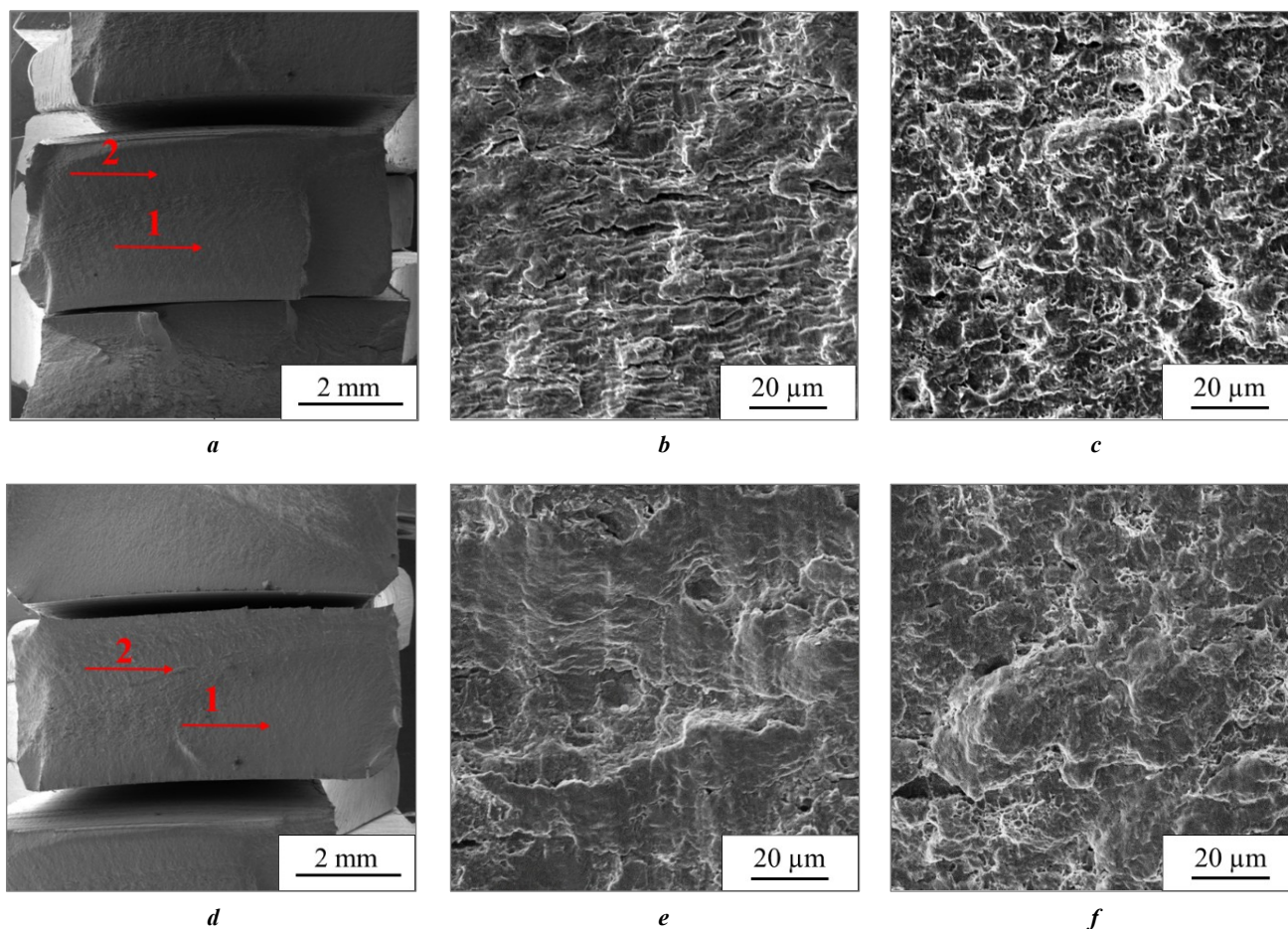


**Fig. 6.** Macro- (*a, d*) and microstructure (*b, c, e, f*) of fractures of welded joints after endurance tests after welding according to the mode No. 1 in the initial state (*a–c*,  $\sigma_a=420$  MPa,  $N=24142$ ) and after tempering (*d–f*,  $\sigma_a=420$  MPa,  $N=13631$ ): *a, d* – general appearance; *b, e* – area 1 (fatigue zone); *c, f* – area 2 (fracture zone)  
**Рис. 6.** Макро- (*a, d*) и микростроение (*b, c, e, f*) изломов сварных соединений после испытаний на усталостную прочность после сварки по режиму № 1 в исходном состоянии (*a–c*,  $\sigma_a=420$  МПа,  $N=24142$ ) и после отпуска (*d–f*,  $\sigma_a=420$  МПа,  $N=13631$ ): *a, d* – общий вид; *b, e* – участок 1 (зона усталости); *c, f* – участок 2 (зона долома)

Thus, a welded joint produced with the force during heating  $F_h=120$  kN (mode No. 3) without subsequent tempering has the highest fatigue strength among the investigated welding modes. Therefore, comparative tests of welded joints and the pipe body material for the construction of limited endurance curves were carried out in this mode. The curves in semilogarithmic coordinates obtained during testing are shown in Fig. 8.

The comparative evaluation of the limited endurance curves (Fig. 8) of this welded joint and the 30XГСА base steel shows that the differences are insignificant. In the low-cycle fatigue area ( $N<1000$ ), the 30XГСА base steel has a bit higher fatigue resistance, while in the high-cycle fatigue area, the base steel and the welded joint have the same averaged level of the fatigue strength. A characteristic feature of the mechanical behaviour of welded joints under the cyclic loading conditions at all stress amplitudes is the destruction both in the zone of the initial material of 30XГСА steel and in the 30XГСА steel TMEZ, regardless of the  $\sigma_a$  value, which indicates the strength uniformity of these zones.

The morphology of the fracture surface of samples of welded joints and 30XГСА steel formed at different amplitude stresses is shown in Fig. 9, 10.

It is evident that at fracture in the stress range of  $\pm 495$ –508 MPa, there are some differences in the structure of fracture of welded joints and the 30XГСА steel base metal (Fig. 9). On the fatigue fracture surface of the welded joint specimen (Fig. 9 b), stepped plateau-like areas surrounded by dimples were formed. The fatigue grooves are indistinct. A rougher relief of the fatigue fracture zone is observed in the base metal specimen (Fig. 9 e). The crack initiation occurs in two areas of the sample, near the defects or inclusions (Fig. 9 d). The fracture zones of both samples (Fig. 9 c, 9 f) are characterized by the shallow-pitted microrelief.

With a decrease in the active stress and an increase in the number of cycles to failure, the plateau-like areas occupy the major area of the fatigue fracture zone (Fig. 10 a, 10 b, 10 d, 10 f). However, the fatigue grooves are clearly formed only in the small areas of fracture surfaces; in other areas, they are poorly formed and broken under the influence

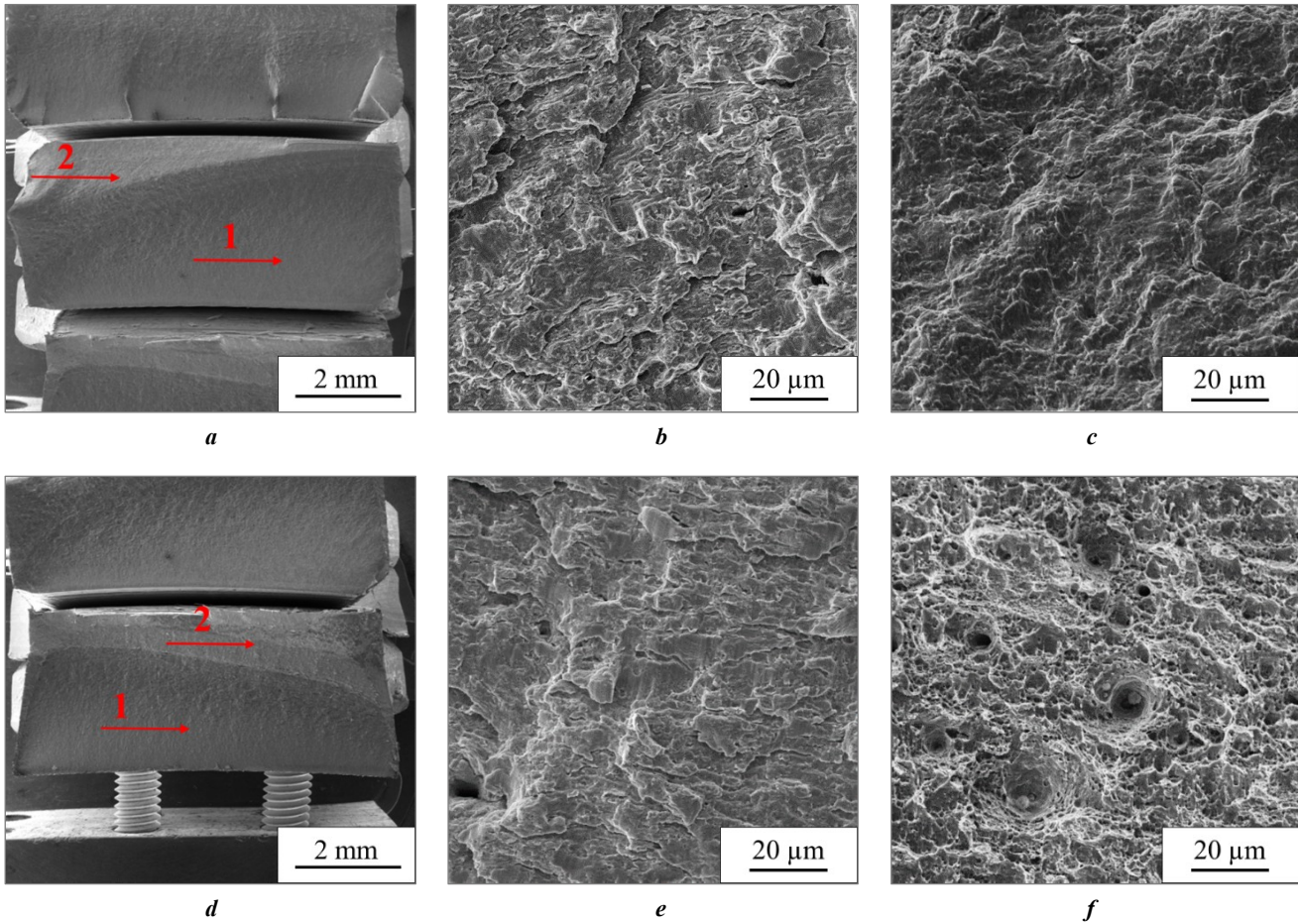


**Fig. 7.** Macro- (*a, d*) and microstructure (*b, c, e, f*) of fractures of welded joints after endurance tests after welding according to the mode No. 3 in the initial state (*a–c*,  $\sigma_a=420$  MPa,  $N=32825$ ) and after tempering (*d–f*,  $\sigma_a=420$  MPa,  $N=23384$ ): *a, d* – general appearance; *b, e* – area 1 (fatigue zone); *c, f* – area 2 (fracture zone)

**Рис. 7.** Макро- (*a, d*) и микростроение (*b, c, e, f*) изломов сварных соединений после испытаний на усталостную прочность после сварки по режиму № 3 в исходном состоянии (*a–c*,  $\sigma_a=420$  МПа,  $N=32825$ ) и после отпуски (*d–f*,  $\sigma_a=420$  МПа,  $N=23384$ ): *a, d* – общий вид; *b, e* – участок 1 (зона усталости); *c, f* – участок 2 (зона долома)

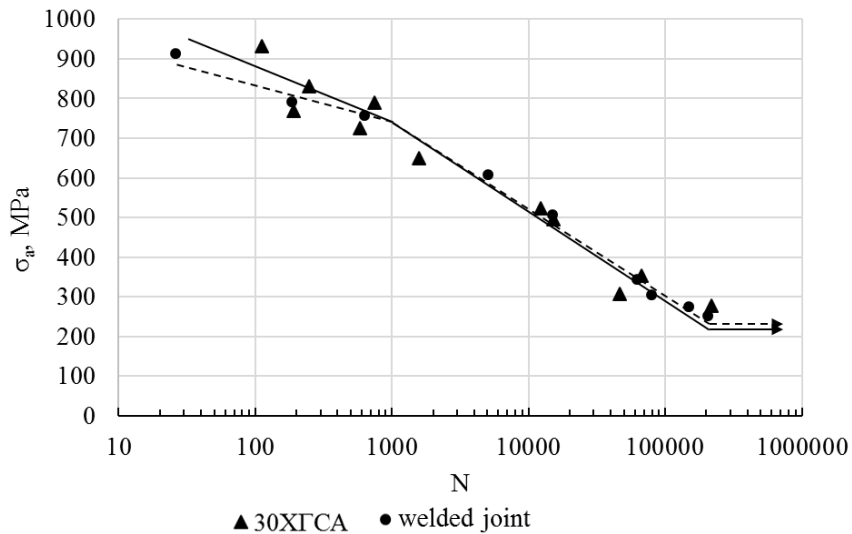


**Fig. 8.** Limited endurance curves of the 30XГСА steel and a welded joint of 30XГСА–40XMΦA steels  
**Рис. 8.** Кривые ограниченной выносливости стали 30XГСА и сварного соединения сталей 30XГСА–40XMΦA

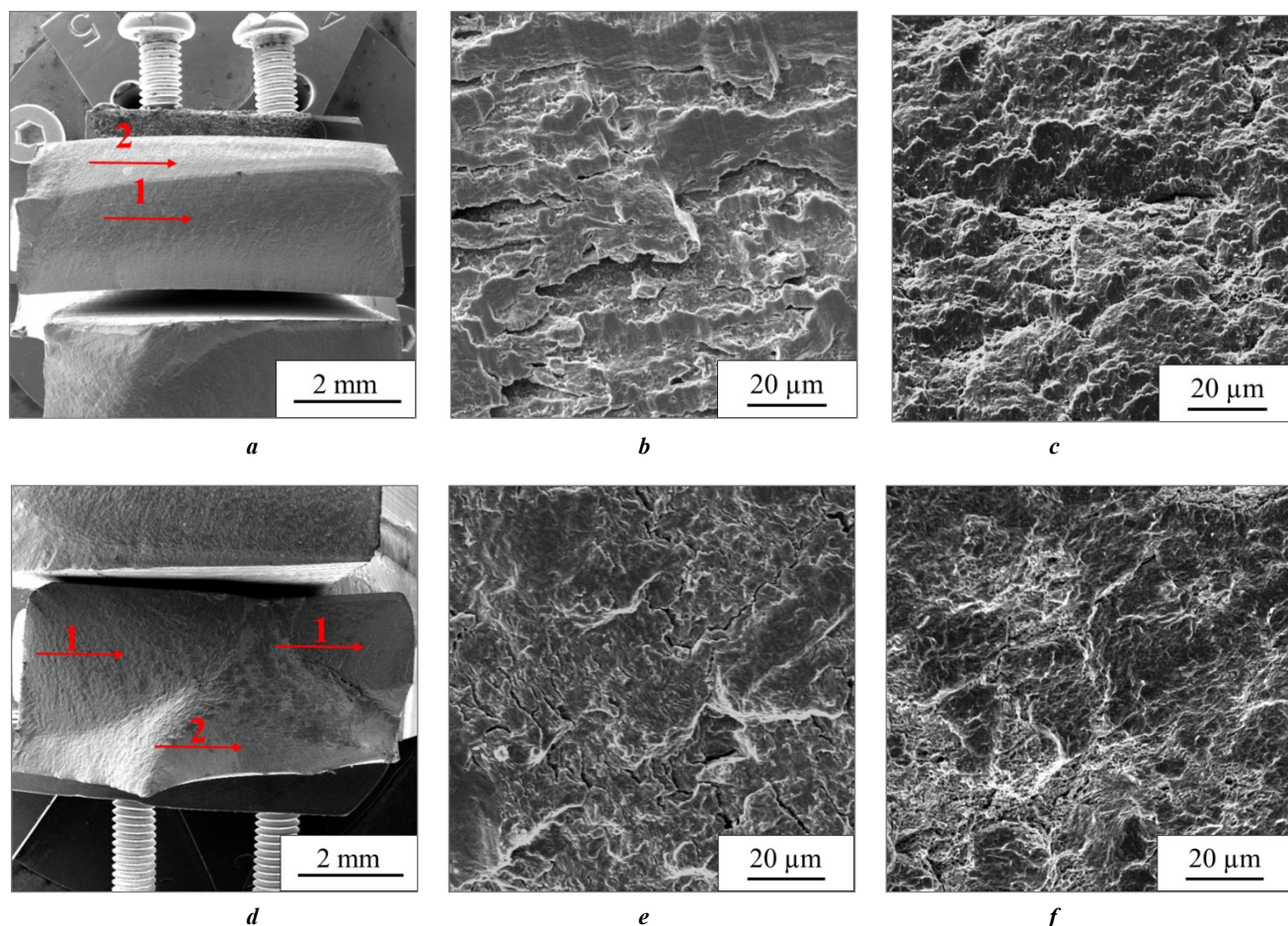


**Fig. 9.** Macro- (a, d) and microstructure (b, c, e, f) of fractures of a 30XГСА–40XMΦA welded joint ( $\sigma_a=495$  MPa,  $N=15077$ ) (a–c) and a monolithic specimen of the 30XГСА steel ( $\sigma_a=508$  MPa,  $N=14965$ ) (d–f) obtained at low-cycle fatigue tests:

a, d – general appearance; b, e – area 1 (fatigue zone); c, f – area 2 (fracture zone)

**Рис. 9.** Макро- (a, d) и микростроение (b, c, e, f) изломов сварного соединения 30XГСА–40XMΦA ( $\sigma_a=495$  МПа,  $N=15077$ ) (a–c) и монолитного образца стали 30XГСА ( $\sigma_a=508$  МПа,  $N=14965$ ) (d–f), полученных при испытаниях в условиях малоциклового усталости:

a, d – общий вид; b, e – участок 1 (зона усталости); c, f – участок 2 (зона долома)

of various factors accompanying fracture. Despite this, the fatigue fracture is well identified in all samples when studying the propagation of the direction of secondary cracks perpendicular to the main crack. Secondary cracks are more clearly expressed in the sample with a welded joint (Fig. 10 b) compared to the base metal. Most probably, this occurs due to the formation of a crystallographic texture in the welded joint zone under the influence of the thermal deformation cycle of welding [24]. The fracture zones of both samples (Fig. 10 c, 10 f) have a typical shallow-pitted relief.

## DISCUSSION

The results of the study showed that the welded joint of 30XГСА and 40XMΦA steels under certain welding parameters is capable of ensuring a full-strength structure with the 30XГСА steel both under the static tension, as established in the work [25], and under cyclic loading. One of the RFW parameters affecting the properties of a welded joint is the force during heating. The present study identified that with an increase in the force during heating, the TME zones strengthen at the reduction in their length

from the side of each type of steel, which contributes to an increase in the fatigue endurance of the studied welded joints. Most probably, this effect is caused by the intensification of the processes of strain hardening in the TME zones implemented during RFW, as established in the work [12]. However, when the deformed microstructure is heated, the recovery and polygonization processes develop, which are accompanied by local softening of the materials in the TMEZ and a decrease in fatigue endurance, which was also observed in the work [26]. The fatigue crack growth rate increases, which is confirmed by the results of microfractographic analysis. Therefore, tempering of a welded joint of 30XГСА–40XMΦA steels will have a negative impact on the properties of the structure.

## MAIN RESULTS AND CONCLUSIONS

1. The study identified that with an increase in the force during heating in the process of RFW of tubular billets of the H standard size according to ISO 10097 made of 30XГСА and 40XMΦA steels in the range from 40 to 120 kN, microstructural changes occur, accompanied by

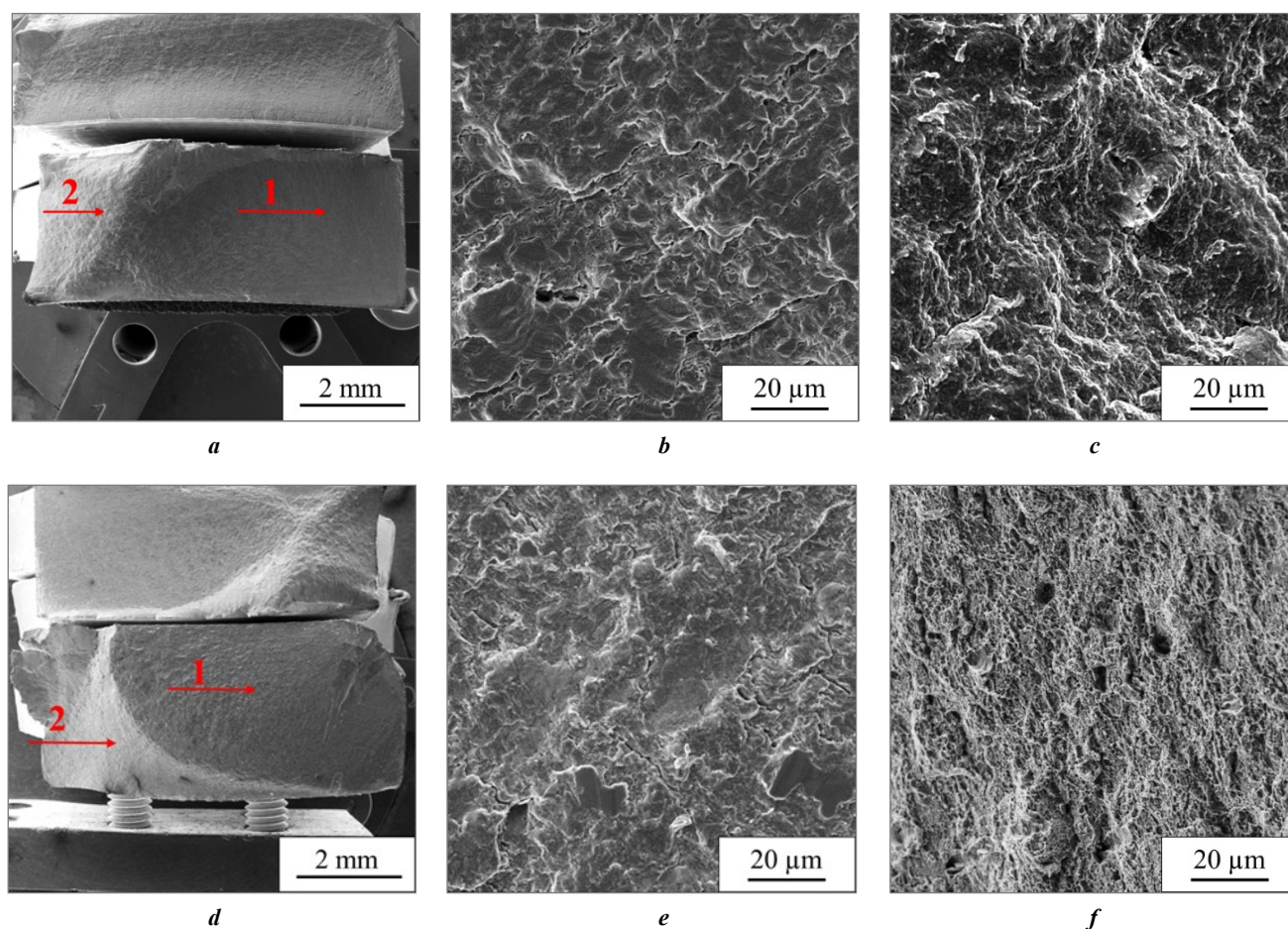


**Fig. 10.** Macro- (a, d) and microstructure (b, c, e, f) of fractures of 30XГСА–40ХМФА welded joints ( $\sigma_a=354$  MPa,  $N=67321$ ) (a–c) and a monolithic specimen of the 30XГСА steel ( $\sigma=342$  MPa,  $N=62400$ ) (d–f) obtained at multicycle fatigue tests:

a, d – general appearance; b, e – area 1 (fatigue zone); c, f – area 2 (fracture zone)

**Рис. 10.** Макро- (a, d) и микростроение (b, c, e, f) изломов сварных соединений 30XГСА–40ХМФА ( $\sigma_a=354$  МПа,  $N=67321$ ) (a–c) и монолитного образца стали 30XГСА ( $\sigma=342$  МПа,  $N=62400$ ) (d–f), полученных при испытаниях в условиях многоциклового усталости:

a, d – общий вид; b, e – участок 1 (зона усталости); c, f – участок 2 (зона долома)

a reduction in the TMEZ length and strengthening of the peripheral areas, which contributes to an increase in the fatigue strength of welded joints.

2. Post-weld tempering causes a decrease in the number of cycles before failure compared to the initial state of welded joints by 15–40 %, depending on the welding mode. In this case, tempering leads to the formation of a smoother microrelief in the fracture and an increase in the distance between the fatigue failure grooves.

3. Based on the research, the optimal RFW mode was determined for the lightened structures of the H standard size exploration drill pipes, which corresponds to the force during heating (at friction)  $F_n=120$  kN, the forging force  $F_{for}=160$  kN, the rotational speed during heating  $n=800$  Rpm, and the upset during heating  $l=8$  mm. With the specified RFW process parameters, the fatigue strength of welded joints is comparable to the fatigue strength of the base metal of the weakest 30XГСА steel, which is confirmed by the limited endurance curves and the almost identical nature of the destruction revealed by macro- and microfractographic studies.

## REFERENCES

1. Emre H.E., Kaçar R. Effect of Post Weld Heat Treatment Process on Microstructure and Mechanical Properties of Friction Welded Dissimilar Drill Pipe. *Materials Research*, 2015, vol. 18, no. 3, pp. 503–508. DOI: [10.1590/1516-1439.308114](https://doi.org/10.1590/1516-1439.308114).
2. Banerjee A., Ntovas M., Da Silva L., Rahimi S., Wynne B. Inter-relationship between microstructure evolution and mechanical properties in inertia friction welded 8630 low-alloy steel. *Archives of Civil and Mechanical Engineering*, 2021, vol. 21, article number 149. DOI: [10.1007/s43452-021-00300-9](https://doi.org/10.1007/s43452-021-00300-9).
3. Khadeer Sk.A., Babu P.R., Kumar B.R., Kumar A.S. Evaluation of friction welded dissimilar pipe joints between AISI 4140 and ASTM A 106 Grade B steels used in deep exploration drilling. *Journal of Manufacturing Processes*, 2020, vol. 56, pp. 197–205. DOI: [10.1016/j.jmapro.2020.04.078](https://doi.org/10.1016/j.jmapro.2020.04.078).
4. Kumar A.S., Khadeer Sk.A., Rajinikanth V., Pahari S., Kumar B.R. Evaluation of bond interface characteristics of rotary friction welded carbon steel to low alloy steel pipe joints. *Materials Science & Engineering A*, 2021,

- vol. 824, article number 141844. DOI: [10.1016/j.msea.2021.141844](https://doi.org/10.1016/j.msea.2021.141844).
5. Li P., Wang S., Xia Y., Hao X., Lei Z., Dong H. Inhomogeneous microstructure and mechanical properties of rotary friction welded AA2024 joints. *Journal of Materials Research and Technology*, 2020, vol. 9, no. 3, pp. 5749–5760. DOI: [10.1016/j.jmrt.2020.03.100](https://doi.org/10.1016/j.jmrt.2020.03.100).
  6. Nagaraj M., Ravisankar B. Effect of Severe Plastic Deformation on Microstructure and Mechanical Behaviour of Friction-Welded Structural Steel IS2062. *Transactions of the Indian Institute of Metals*, 2019, vol. 72, pp. 751–756. DOI: [10.1007/s12666-018-1527-1](https://doi.org/10.1007/s12666-018-1527-1).
  7. Jeffrey W.S., Thomas G.H., McColskey J.D., Victor F.P., Ramirez A.J. Characterization of mechanical properties, fatigue-crack propagation, and residual stresses in a microalloyed pipeline-steel friction-stir weld. *Materials and Design*, 2015, vol. 88, pp. 632–642. DOI: [10.1016/j.matdes.2015.09.049](https://doi.org/10.1016/j.matdes.2015.09.049).
  8. Abdulstaar M.A., Al-Fadhlah K.J., Wagner L. Microstructural variation through weld thickness and mechanical properties of peened friction stir welded 6061 aluminum alloy joints. *Materials Characterization*, 2017, vol. 126, pp. 64–73. DOI: [10.1016/j.matchar.2017.02.011](https://doi.org/10.1016/j.matchar.2017.02.011).
  9. Mc Pherson N.A., Galloway A.M., Cater S.R., Hambling S.J. Friction stir welding of thin DH36 steel plate. *Science and Technology of Welding & Joining*, 2013, vol. 18, pp. 441–450. DOI: [10.1179/1362171813Y.0000000122](https://doi.org/10.1179/1362171813Y.0000000122).
  10. Baillie P., Campbell S., Galloway A., Cater S.R., Mcpherson N.A. A Comparison of Double Sided Friction Stir Welding in Air and Underwater for 6mm S275 Steel Plate. *International Journal of Chemical, Nuclear, Metallurgical and Materials Engineering*, 2014, vol. 8, pp. 651–655. DOI: [10.13140/2.1.2306.2400](https://doi.org/10.13140/2.1.2306.2400).
  11. Ericsson M., Sandstrom R. Influence of welding speed on the fatigue of friction stir welds, and comparison with MIG and TIG. *International Journal of Fatigue*, 2003, vol. 25, no. 12, pp. 1379–1387. DOI: [10.1016/S0142-1123\(03\)00059-8](https://doi.org/10.1016/S0142-1123(03)00059-8).
  12. Yamamoto Y., Ochi H., Sawai T., Ogawa K., Tsujino R., Yasutomi M. Tensile Strength and Fatigue Strength of Friction-Welded SUS304 Stainless Steel Joints-Evaluation of Joint Strength by Deformation Heat Input in Upset Stage and Upset Burn-Off Length. *Journal of the Society of Materials Science Japan*, 2004, vol. 53, no. 5, pp. 512–517. DOI: [10.2472/jsms.53.5.12](https://doi.org/10.2472/jsms.53.5.12).
  13. Paventhan R., Lakshminarayanan P.R., Balasubramanian V. Fatigue behaviour of friction welded medium carbon steel and austenitic stainless steel dissimilar joints. *Materials and Design*, 2011, vol. 32, no. 4, pp. 1888–1894. DOI: [10.1016/j.matdes.2010.12.011](https://doi.org/10.1016/j.matdes.2010.12.011).
  14. Sahin M. Joining with friction welding of high speed and medium carbon steel. *Journal of Materials Processing Technology*, 2005, vol. 168, no. 2, pp. 168–202. DOI: [10.1016/j.jmatprotec.2004.11.015](https://doi.org/10.1016/j.jmatprotec.2004.11.015).
  15. Atamashkin A.S., Priymak E.Yu., Tulibaev E.S., Stepanchukova A.V. Endurance limit and mechanism of fracture of friction welded joints of exploration drill pipes in the conditions of multi-cycle fatigue. *Chernye metally*, 2021, no. 5, pp. 33–38. DOI: [10.17580/chm.2021.05.06](https://doi.org/10.17580/chm.2021.05.06).
  16. Belkahla Y., Mazouzi A., Lebouachera S.E.I., Hassan A.J., Fides M., Hvizdoš P., Cheniti B., Miroud D. Rotary friction welded C45 to 16NiCr6 steel rods: statistical optimization coupled to mechanical and microstructure approaches. *The International Journal of Advanced Manufacturing Technology*, 2021, vol. 116, pp. 2285–2298. DOI: [10.1007/s00170-021-07597-z](https://doi.org/10.1007/s00170-021-07597-z).
  17. Selvamani S.T., Vigneshwar M., Nikhil M., Hariharan S.J., Palanikumar K. Enhancing the Fatigue Properties of Friction Welded AISI 1020 Grade Steel Joints using Post Weld Heat Treatment Process in Optimized Condition. *Materials Today: Proceedings*, 2019, vol. 16-2, pp. 1251–1258. DOI: [10.1016/j.matpr.2019.05.222](https://doi.org/10.1016/j.matpr.2019.05.222).
  18. Mercan S., Aydin S., Özdemir N. Effect of welding parameters on the fatigue properties of dissimilar AISI 2205–AISI 1020 joined by friction welding. *International Journal of Fatigue*, 2015, vol. 81, pp. 78–90. DOI: [10.1016/j.ijfatigue.2015.07.023](https://doi.org/10.1016/j.ijfatigue.2015.07.023).
  19. Barrionuevo G.O., Mullo J.L., Ramos-Grez J.A. Predicting the ultimate tensile strength of AISI 1045 steel and 2017-T4 aluminum alloy joints in a laser-assisted rotary friction welding process using machine learning: a comparison with response surface methodology. *The International Journal of Advanced Manufacturing Technology*, 2021, vol. 116, pp. 1247–1257. DOI: [10.1007/s00170-021-07469-6](https://doi.org/10.1007/s00170-021-07469-6).
  20. Lukin V.I., Ovsepyan S.V., Kovalchuk V.G., Samorukov M.L. Features of rotary friction welding of high-temperature nickel alloy VZh175. *Trudy VIAM*, 2017, no. 12, pp. 3–12. DOI: [10.18577/2307-6046-2017-0-12-1-1](https://doi.org/10.18577/2307-6046-2017-0-12-1-1).
  21. Fang Y., Jiang X., Mo D., Zhu D., Luo Z. A review on dissimilar metals' welding methods and mechanisms with interlayer. *The International Journal of Advanced Manufacturing Technology*, 2019, vol. 102, pp. 2845–2863. DOI: [10.1007/s00170-019-03353-6](https://doi.org/10.1007/s00170-019-03353-6).
  22. Kuzmina E.A., Priymak E.Yu., Kirilenko A.S. Optimization of parameters of friction stir welded unlike joints of medium-carbon alloy steels 30KhGSA and 40KhMFA. *Metal Science and Heat Treatment*, 2023, vol. 64, no. 9-10, pp. 596–602. DOI: [10.1007/s11041-023-00855-9](https://doi.org/10.1007/s11041-023-00855-9).
  23. Vill V.I. *Svarka metallov treniem* [Friction welding of metals]. Moscow, Mashinostroenie Publ., 1970. 176 p.
  24. Priymak E.Yu., Lobanov M.L., Belikov S.V., Karabanalov M.S., Yakovleva I.L. Structure Formation Patterns and Crystallographic Texture in Welded Joints of Medium-Carbon Alloy Steels in the Process of Rotary Friction Welding. *Physics of Metals and Metallography*, 2022, vol. 123, no. 6, pp. 559–566. DOI: [10.1134/S0031918X22060126](https://doi.org/10.1134/S0031918X22060126).
  25. Kuzmina E.A., Priymak E.Yu., Kirilenko A.S., Semka Ya.S. Influence of the heating force in rotational friction welding on mechanical properties and tensile fracture mechanism of dissimilar welded joints of 30KhGSA and 40KhMFA steels. *Chernye metally*, 2022, no. 12, pp. 49–57. DOI: [10.17580/chm.2022.12.07](https://doi.org/10.17580/chm.2022.12.07).
  26. Atamashkin A.S., Priymak E.Yu. The influence of postweld tempering on mechanical behavior of friction welded joints of 32G2 and 40HN steels under high-cycle fatigue. *Vektor nauki Tolyattinskogo gosudarstvennogo universiteta*, 2021, no. 3, pp. 7–18. DOI: [10.18323/2073-5073-2021-3-7-18](https://doi.org/10.18323/2073-5073-2021-3-7-18).

#### СПИСОК ЛІТЕРАТУРИ

1. Emre H.E., Kaçar R. Effect of Post Weld Heat Treatment Process on Microstructure and Mechanical Properties of Friction Welded Dissimilar Drill Pipe // *Materials*

- Research. 2015. Vol. 18. № 3. P. 503–508. DOI: [10.1590/1516-1439.308114](https://doi.org/10.1590/1516-1439.308114).
2. Banerjee A., Ntovas M., Da Silva L., Rahimi S., Wynne B. Inter-relationship between microstructure evolution and mechanical properties in inertia friction welded 8630 low-alloy steel // *Archives of Civil and Mechanical Engineering*. 2021. Vol. 21. Article number 149. DOI: [10.1007/s43452-021-00300-9](https://doi.org/10.1007/s43452-021-00300-9).
  3. Khadeer Sk.A., Babu P.R., Kumar B.R., Kumar A.S. Evaluation of friction welded dissimilar pipe joints between AISI 4140 and ASTM A 106 Grade B steels used in deep exploration drilling // *Journal of Manufacturing Processes*. 2020. Vol. 56. P. 197–205. DOI: [10.1016/j.jmapro.2020.04.078](https://doi.org/10.1016/j.jmapro.2020.04.078).
  4. Kumar A.S., Khadeer Sk.A., Rajinikanth V., Pahari S., Kumar B.R. Evaluation of bond interface characteristics of rotary friction welded carbon steel to low alloy steel pipe joints // *Materials Science & Engineering A*. 2021. Vol. 824. Article number 141844. DOI: [10.1016/j.msea.2021.141844](https://doi.org/10.1016/j.msea.2021.141844).
  5. Li P., Wang S., Xia Y., Hao X., Lei Z., Dong H. Inhomogeneous microstructure and mechanical properties of rotary friction welded AA2024 joints // *Journal of Materials Research and Technology*. 2020. Vol. 9. № 3. P. 5749–5760. DOI: [10.1016/j.jmrt.2020.03.100](https://doi.org/10.1016/j.jmrt.2020.03.100).
  6. Nagaraj M., Ravisankar B. Effect of Severe Plastic Deformation on Microstructure and Mechanical Behaviour of Friction-Welded Structural Steel IS2062 // *Transactions of the Indian Institute of Metals*. 2019. Vol. 72. P. 751–756. DOI: [10.1007/s12666-018-1527-1](https://doi.org/10.1007/s12666-018-1527-1).
  7. Jeffrey W.S., Thomas G.H., McColskey J.D., Victor F.P., Ramirez A.J. Characterization of mechanical properties, fatigue-crack propagation, and residual stresses in a microalloyed pipeline-steel friction-stir weld // *Materials and Design*. 2015. Vol. 88. P. 632–642. DOI: [10.1016/j.matdes.2015.09.049](https://doi.org/10.1016/j.matdes.2015.09.049).
  8. Abdulstaar M.A., Al-Fadhlah K.J., Wagner L. Microstructural variation through weld thickness and mechanical properties of peened friction stir welded 6061 aluminum alloy joints // *Materials Characterization*. 2017. Vol. 126. P. 64–73. DOI: [10.1016/j.matchar.2017.02.011](https://doi.org/10.1016/j.matchar.2017.02.011).
  9. Mc Pherson N.A., Galloway A.M., Cater S.R., Hambling S.J. Friction stir welding of thin DH36 steel plate // *Science and Technology of Welding & Joining*. 2013. Vol. 18. P. 441–450. DOI: [10.1179/1362171813Y.0000000122](https://doi.org/10.1179/1362171813Y.0000000122).
  10. Baillie P., Campbell S., Galloway A., Cater S.R., Mcpherson N.A. A Comparison of Double Sided Friction Stir Welding in Air and Underwater for 6mm S275 Steel Plate // *International Journal of Chemical, Nuclear, Metallurgical and Materials Engineering*. 2014. Vol. 8. P. 651–655. DOI: [10.13140/2.1.2306.2400](https://doi.org/10.13140/2.1.2306.2400).
  11. Ericsson M., Sandstrom R. Influence of welding speed on the fatigue of friction stir welds, and comparison with MIG and TIG // *International Journal of Fatigue*. 2003. Vol. 25. № 12. P. 1379–1387. DOI: [10.1016/S0142-1123\(03\)00059-8](https://doi.org/10.1016/S0142-1123(03)00059-8).
  12. Yamamoto Y., Ochi H., Sawai T., Ogawa K., Tsujino R., Yasutomi M. Tensile Strength and Fatigue Strength of Friction-Welded SUS304 Stainless Steel Joints-Evaluation of Joint Strength by Deformation Heat Input in Upset Stage and Upset Burn-Off Length // *Journal of the Society of Materials Science Japan*. 2004. Vol. 53. № 5. P. 512–517. DOI: [10.2472/jsms.53.512](https://doi.org/10.2472/jsms.53.512).
  13. Paventhan R., Lakshminarayanan P.R., Balasubramanian V. Fatigue behaviour of friction welded medium carbon steel and austenitic stainless steel dissimilar joints // *Materials and Design*. 2011. Vol. 32. № 4. P. 1888–1894. DOI: [10.1016/j.matdes.2010.12.011](https://doi.org/10.1016/j.matdes.2010.12.011).
  14. Sahin M. Joining with friction welding of high speed and medium carbon steel // *Journal of Materials Processing Technology*. 2005. Vol. 168. № 2. P. 168–202. DOI: [10.1016/j.jmatprotec.2004.11.015](https://doi.org/10.1016/j.jmatprotec.2004.11.015).
  15. Атамашкин А.С., Приймак Е.Ю., Тулибаев Е.С., Степанчукова А.В. Предел выносливости и механизм разрушения фрикционных сварных соединений геолого-разведочных бурильных труб // *Черные металлы*. 2021. № 5. С. 33–38. DOI: [10.17580/chm.2021.05.06](https://doi.org/10.17580/chm.2021.05.06).
  16. Belkahlia Y., Mazouzi A., Lebouachera S.E.I., Hassan A.J., Fides M., Hvizdoš P., Cheniti B., Miroud D. Rotary friction welded C45 to 16NiCr6 steel rods: statistical optimization coupled to mechanical and microstructure approaches // *The International Journal of Advanced Manufacturing Technology*. 2021. Vol. 116. P. 2285–2298. DOI: [10.1007/s00170-021-07597-z](https://doi.org/10.1007/s00170-021-07597-z).
  17. Selvamani S.T., Vigneshwar M., Nikhil M., Hariharan S.J., Palanikumar K. Enhancing the Fatigue Properties of Friction Welded AISI 1020 Grade Steel Joints using Post Weld Heat Treatment Process in Optimized Condition // *Materials Today: Proceedings*. 2019. Vol. 16-2. P. 1251–1258. DOI: [10.1016/j.matpr.2019.05.222](https://doi.org/10.1016/j.matpr.2019.05.222).
  18. Mercan S., Aydin S., Özdemir N. Effect of welding parameters on the fatigue properties of dissimilar AISI 2205–AISI 1020 joined by friction welding // *International Journal of Fatigue*. 2015. Vol. 81. P. 78–90. DOI: [10.1016/j.ijfatigue.2015.07.023](https://doi.org/10.1016/j.ijfatigue.2015.07.023).
  19. Barrionuevo G.O., Mullo J.L., Ramos-Grez J.A. Predicting the ultimate tensile strength of AISI 1045 steel and 2017-T4 aluminum alloy joints in a laser-assisted rotary friction welding process using machine learning: a comparison with response surface methodology // *The International Journal of Advanced Manufacturing Technology*. 2021. Vol. 116. P. 1247–1257. DOI: [10.1007/s00170-021-07469-6](https://doi.org/10.1007/s00170-021-07469-6).
  20. Лукин В.И., Овсепян С.В., Ковальчук В.Г., Саморук М.Л. Особенности ротационной сварки трением высокожаропрочного никелевого сплава ВЖ175 // *Труды ВИАМ*. 2017. № 12. С. 3–12. DOI: [10.18577/2307-6046-2017-0-12-1-1](https://doi.org/10.18577/2307-6046-2017-0-12-1-1).
  21. Fang Y., Jiang X., Mo D., Zhu D., Luo Z. A review on dissimilar metals' welding methods and mechanisms with interlayer // *The International Journal of Advanced Manufacturing Technology*. 2019. Vol. 102. P. 2845–2863. DOI: [10.1007/s00170-019-03353-6](https://doi.org/10.1007/s00170-019-03353-6).
  22. Кузьмина Е.А., Приймак Е.Ю., Кириленко А.С. Оптимизация параметров ротационной сварки трением разнородных сварных соединений среднеуглеродистых легированных сталей 30ХГСА и 40ХМФА // *Металловедение и термическая обработка металлов*. 2022. № 10. С. 52–59. DOI: [10.30906/mitom.2022.10.52-59](https://doi.org/10.30906/mitom.2022.10.52-59).
  23. Вилль В.И. Сварка металлов трением. М.: Машиностроение, 1970. 176 с.
  24. Priymak E.Yu., Lobanov M.L., Belikov S.V., Karabanalov M.S., Yakovleva I.L. Structure Formation Patterns and Crystallographic Texture in Welded Joints of Medium-Carbon Alloy Steels in the Process of Rotary Friction Welding // *Physics of Metals and Metallo-*

- graphy. 2022. Vol. 123. № 6. P. 559–566. DOI: [10.1134/S0031918X22060126](https://doi.org/10.1134/S0031918X22060126).
25. Кузьмина Е.А., Приймак Е.Ю., Кириленко А.С., Сёмка Я.С. Влияние силы нагрева при ротационной сварке трением на механические свойства и механизм разрушения при растяжении разнородных сварных соединений сталей 30ХГСА и 40ХМФА // Черные металлы. 2022. № 12. С. 49–57. DOI: [10.17580/chm.2022.12.07](https://doi.org/10.17580/chm.2022.12.07).
26. Атамашкин А.С., Приймак Е.Ю. Влияние послесварочного отпуска на механическое поведение фрикционных сварных соединений сталей 32Г2 и 40ХН в условиях многоциклового усталости // Вектор науки Тольяттинского государственного университета. 2021. № 3. С. 7–18. DOI: [10.18323/2073-5073-2021-3-7-18](https://doi.org/10.18323/2073-5073-2021-3-7-18).

## Усталостная прочность сварных соединений сталей 30ХГСА–40ХМФА, полученных ротационной сваркой трением

© 2023

**Приймак Елена Юрьевна**<sup>\*1,2,4</sup>, кандидат технических наук, заведующий лабораторией металловедения и термической обработки, доцент кафедры материаловедения и технологии материалов  
**Кузьмина Елена Александровна**<sup>1</sup>, начальник технического отдела  
**Гладковский Сергей Викторович**<sup>3,5</sup>, доктор технических наук, главный научный сотрудник  
**Вичужанин Дмитрий Иванович**<sup>3,6</sup>, кандидат технических наук, старший научный сотрудник  
**Веселова Валерия Евгеньевна**<sup>3,7</sup>, младший научный сотрудник

<sup>1</sup>АО «Завод бурового оборудования», Оренбург (Россия)

<sup>2</sup>Оренбургский государственный университет, Оренбург (Россия)

<sup>3</sup>Институт машиноведения имени Э.С. Горкунова УрО РАН, Екатеринбург (Россия)

\*E-mail: [elena-pijmak@yandex.ru](mailto:elena-pijmak@yandex.ru)

<sup>4</sup>ORCID: <https://orcid.org/0000-0002-4571-2410>

<sup>5</sup>ORCID: <https://orcid.org/0000-0002-3542-6242>

<sup>6</sup>ORCID: <https://orcid.org/0000-0002-6508-6859>

<sup>7</sup>ORCID: <https://orcid.org/0000-0002-4955-6435>

Поступила в редакцию 02.11.2022

Принята к публикации 16.02.2023

**Аннотация:** Ротационная сварка трением (РСТ) используется при производстве бурильных труб для геолого-разведки на твердые полезные ископаемые. Потребность в создании облегченных колонн бурильных труб для высокоскоростного алмазного бурения сверхглубоких скважин диктует необходимость более пристального внимания к изучению зоны сварного шва и назначению технологических параметров РСТ. В работе приведены результаты экспериментальных исследований сварного соединения бурильной трубы типоразмера  $H$  по ISO 10097 из сталей 30ХГСА (тело трубы) и 40ХМФА (замковая часть) в условиях воздействия циклических нагрузок. Оценивалось влияние силы, прикладываемой к заготовкам в процессе трения соприкасающихся поверхностей (силы при нагреве), и послесварочного отпуска при температуре 550 °С на циклическую долговечность сварных соединений в условиях знакопеременного растяжения-сжатия при напряжении амплитуды цикла  $\pm 420$  МПа. Установлено, что с увеличением силы при нагреве в зоне термомеханического влияния происходят изменения микроструктуры, способствующие повышению усталостной прочности сварных соединений. Выявлено негативное влияние послесварочного отпуска на усталостную прочность сварных соединений, выражающееся в снижении количества циклов до разрушения на 15–40 % в зависимости от величины силы при нагреве. Определен оптимальный режим РСТ указанного сочетания сталей, обеспечивающий наибольшее количество циклов до разрушения: сила при нагреве (при трении)  $F_H=120$  кН, сила проковки  $F_{пр}=160$  кН, частота вращения при нагреве  $n=800$  об/мин и осадка при нагреве  $l=8$  мм. Проведена серия усталостных испытаний при различных значениях напряжения амплитуды цикла сварного соединения, полученного на оптимальном режиме, и основного металла стали 30ХГСА; построены кривые ограниченной выносливости. Показано, что различия в кривых ограниченной выносливости материала тела трубы (сталь 30ХГСА) и сварного соединения незначительны. Полученные результаты дополнены данными измерений микротвердости и фрактограммами разрушенных образцов, раскрывающими механизм распространения трещин в условиях воздействия циклических нагрузок.

**Ключевые слова:** ротационная сварка трением; бурильные трубы; сварное соединение; усталостная прочность; кривая ограниченной выносливости; сталь 30ХГСА; сталь 40ХМФА.

**Благодарности:** Исследование выполнено при финансовой поддержке РФФИ в рамках научного проекта № 20-38-90032.

При проведении механических испытаний использовалось оборудование, входящее в состав ЦКП «Пластометрия» Института машиноведения имени Э.С. Горкунова УрО РАН.

**Для цитирования:** Приймак Е.Ю., Кузьмина Е.А., Гладковский С.В., Вичужанин Д.И., Веселова В.Е. Усталостная прочность сварных соединений сталей 30ХГСА–40ХМФА, полученных ротационной сваркой трением // Frontier Materials & Technologies. 2023. № 1. С. 69–81. DOI: [10.18323/2782-4039-2023-1-69-81](https://doi.org/10.18323/2782-4039-2023-1-69-81).